Towards a MagnetoCaloric Cooling System

Using Interactions of Magnetic Fields & Magnetic Fluids

Shubham Dalvi

Towards A MagnetoCaloric Cooling System -

Using Interactions of Magnetic Fields & Magnetic Fluids

Shubham Dalvi

This dissertation has been approved by the Supervisor:

Prof. Dr. Ir. Gerrit Brem

and the Co-supervisors

Prof. Dr. Ir. Theo H van der Meer
Dr. Mina Shahi

The present thesis work is carried out in the Thermal Engineering group of the Faculty of Engineering Technology, University of Twente. The research is part of the NET-MNF project and is (partly) financed by the Netherlands Organization for Scientific Research (NWO).

Cover Design: Bhakti Dalvi
Printed by: IPSKAMP printing, Enschede, The Netherlands
ISBN: 978-90-365-5783-2
DOI: 10.3990/1.9789036557849

Copyright © 2023 by Shubham Dalvi, The Netherlands
All rights reserved. No parts of this thesis may be reproduced, stored in a retrieval system or transmitted in any form or by any means without permission of the author.
Alle rechten voorbehouden. Niets uit deze uitgave mag worden vermenigvuldigd, in enige vorm of op enige wijze, zonder voorafgaande schriftelijke toestemming van de auteur.

Towards A MagnetoCaloric Cooling System -

Using Interactions of Magnetic Fields & Magnetic Fluids

DISSERTATION

to obtain the degree of doctor
at the University of Twente,
on the authority of rector magnificus,
Prof. Dr. Ir. A. Veldkamp,
on account of the decision of the Doctorate Board,
to be publicly defended
on Thursday 28 September 2023 at 14:45 hours

by

Shubham Dalvi

born on 9th of May 1995
in Pune, India

Graduation Committee :

Chair/Secretary:	Prof. Dr. Ir. H.F.J.M. Koopman *University of Twente, ET*
Supervisor:	Prof. Dr. Ir. Gerrit Brem *University of Twente, ET*
Co-supervisors:	Prof. Dr. Ir. Theo H. van der Meer Dr. Mina Shahi *University of Twente, ET*
Committee Members:	Prof. Dr. Bernhard Peters *University of Luxembourg, Faculty of Science, Technology and Medicine*
	Prof. Dr. Ekkes Brück *TU Delft, Faculty of Applied Science*
	Prof. Dr. Ir. Bernard Geurts *University of Twente, EEMCS*
	Prof. Dr. Ir. Wilko Rohlfs *University of Twente, ET*
	Prof. Dr. Ir. Harm Askes *University of Twente, ET*

" Trust those who are

still seeking the truth,

doubt those who claim

to have found it..."

- André Gide

– To Mummy, Pappa, & my sister Bhakti

Summary

Increasing energy consumption has been a major concern on a global scale over the past few decades. A large chunk of resources is required to meet the daily household energy requirements, such as cooling and refrigeration. To overcome this issue, several alternative technologies have been explored by researchers that can achieve the desired objectives at less energy inputs. Magnetic refrigeration is one such technology that functions with low electricity consumption and ecologically superior materials. It operates essentially on the Magneto-Caloric Effect (MCE) which exhibits an increase/decrease in temperature of specific materials under varying magnetic fields.

In the present work, one such implementation of the magnetic refrigeration method is addressed with the help of a numerical framework. To be specific, a computational study is performed for the design and development of a novel MCE based room temperature cooling device. In addition to the existing perks of magnetic refrigeration, the present device is aimed to operate without any external mechanical motion. This is achieved using the mixture of a Magneto-Caloric Material (MCM) and a heat transfer fluid along with an externally applied magnetic field. After a detailed review, Calorivac - H (LaFeMnSiH) is finalized as MCM, whereas Galinstan (GaInSn-68.5%21.5%10%) is used as heat transfer fluid for the current work. The focus of this research is to create an accurate and efficient numerical tool that can predict the complex behaviour of magnetic fluids and magnetic fields under different operating conditions. By doing so, we aim to enhance our understanding of room temperature magnetic cooling and explore its full potential for future applications.

In order to understand the overall functioning, enough emphasis is given in the first place to precisely calculate the magnetic field distribution of distinct sources. Several existing

numerical strategies to represent solenoid and permanent magnet are thoroughly reviewed. Based on this, different solvers are compiled from their inception in the OpenFOAM framework, and their results are compared against published and in-house experimental/analytical data. Contrary to the apparent claims, it is demonstrated that the closely spaced solenoid does not ensure the highest magnetic forces. Further, two unique Halbach arrays are studied to obtain a strong one sided magnetic field distribution for significant MCE. In particular, an enclosed Halbach array is considered for the single stage operation, while a planar Halbach array is finalised for multi-stage arrangements.

A critical review of the existing correlations is provided for each thermo-physical property for its dependency on operating parameters. Additionally, the magnetic properties are addressed along with relaxation mechanisms and the overall response of MCS (Magneto-Caloric Slurry) is classified in two broad categories namely Néel's and Brownian relaxation mechanism. As the present work deals with a solid-liquid suspension, a Critical Deposition Velocity analysis is performed for the non-Newtonian mixture of Calorivac-H and Galinstan. Results obtained at distinct volume fractions and particle sizes are used to avoid the undesired particle settling that leads to high frictional losses and large pressure gradients. Further, a broad perspective is presented on the solid-liquid modelling strategies, and the preference for the Euler-Euler mixture model is justified. A Discrete Element Method study is also performed to understand the dynamic behaviour of an individual Calorivac particle. Moreover, the Diffusion Mixture Model is discussed in great detail to address the physical significance of each volumetric force of the present context.

The possibility of magnetically driven energy transport is first analysed using two independent case studies. Behaviour of distinct magnetic fluids is observed in two different enclosures that are exposed to an externally applied field. It is noticed that in both cases the presence of a magnetic field leads to unique volumetric forces. This ultimately results in the local recirculation zones that further influence the flow characteristics and heat transfer. Based on these observations, a single stage cooling system is studied initially with the help of several local and global variables. Results confirmed that the change in flow-thermal characteristics of MCS is proportional to the amount of MCM used and the strength of applied magnetic field. Moreover, it is concluded that for a 40% mixture of Calorivac-H and Galinstan, a maximum temperature drop of 1.9K is obtained at 1.03 Tesla. This cooling

span is then further expanded with the help of two distinct multi-stage arrangements. These multi-stage configurations operate on the cascading principle and require a heat exchanger cum magnetic shield for its working. A maximum temperature span of 6.08K is achieved from five stage cascade setup at the aforementioned operating conditions. This examination demonstrated the possibility to overcome the limiting ΔT_{ad} that is inherent to different MCM.

To conclude, the present work offers great insights on the performance of MCE based room temperature cooling devices. The results reported in the present work can be used as a foundation to further improve the efficiency and compactness of future prototypes. In addition, the developed numerical tools can be effectively used for understanding the hydro-thermal response of any generic system that involves the interplay of magnetic fluids and external magnetic fields.

Samenvatting

Toenemend energieverbruik is de afgelopen decennia wereldwijd een belangrijke zorg geweest. Een aanzienlijke hoeveelheid middelen is nodig om te voldoen aan de dagelijkse energiebehoeften van huishoudens, bijvoorbeeld voor de klimaatbeheersing en koelkasten. Om dit probleem aan te pakken, hebben onderzoekers verschillende alternatieve technologieën verkend die de gewenste doelstellingen kunnen bereiken met minder energieverbruik. Magnetische koeling is een dergelijke techniek die functioneert met een laag elektriciteitsverbruik en ecologisch superieure materialen. Deze techniek werkt hoofdzakelijk op basis van het zogeheten magnetocalorisch effect (MCE) wat een temperatuurverhoging/-verlaging van specifieke materialen vertoont onder variërende magnetische velden.

In dit werk wordt een implementatie van de magnetische koelmethode behandeld met behulp van een numeriek raamwerk. Om precies te zijn, wordt er een rekenkundige studie uitgevoerd voor het ontwerp en de ontwikkeling van een nieuw apparaat voor koeling bij temperatuur, gebaseerd op het magnetocalorisch effect. Naast de bestaande voordelen van magnetische koeling is het doel van dit apparaat om te werken zonder enige externe mechanische beweging. Dit wordt bereikt door het gebruik van een mengsel van magnetocalorisch materiaal (MCM) en een warmteoverdrachtsvloeistof, samen met een extern aangebracht magnetisch veld. Na een grondige beoordeling is Calorivac-H definitief vastgesteld als MCM, terwijl Galinstan wordt gebruikt als warmteoverdrachtsvloeistof in dit werk. De focus van dit onderzoek is het creëren van een nauwkeurige en efficiënt numeriek hulpmiddel die het complexe gedrag van magnetische vloeistoffen en magnetische velden onder verschillende bedrijfsomstandigheden kan voorspellen. Door dit te doen, streven we ernaar ons begrip van magnetische koeling bij kamertemperatuur te verbeteren en het

volledige potentieel ervan voor toekomstige toepassingen te verkennen.

Om het algehele functioneren te begrijpen, wordt in de eerste plaats nadruk gelegd op het nauwkeurig modelleren van de magnetische veldverdeling van verschillende bronnen. Een aantal bestaande numerieke strategieën, die een spoel en permanente magneet representeren, worden grondig beoordeeld. met betrekking tot permanente magneten en spoelen. Op basis hiervan worden verschillende oplossers samengesteld vanaf hun begin in het OpenFOAM-raamwerk en hun resultaten worden vergeleken met gepubliceerde en interne experimentele/analytische gegevens. In tegenstelling tot de voor de hand liggende beweringen, wordt aangetoond dat de dicht bij elkaar geplaatste spoel niet zorgt voor de hoogste magnetische krachten. Verder worden twee unieke Halbach-rangschikkingen bestudeerd om een sterke eenzijdige verdeling van het magnetisch veld te verkrijgen voor significante magnetocalorische effecten. In het bijzonder wordt een ingesloten Halbach-rangschikking overwogen voor de enkelvoudige bedrijfsmodus, terwijl voor meervoudige opstellingen een plenaire Halbach-rangschikking wordt gekozen.

Een kritische beoordeling van de bestaande correlaties wordt gegeven voor elke thermofysische eigenschap wat betreft de afhankelijkheid van bedrijfsparameters. Daarnaast worden de magnetische eigenschappen behandeld samen met relaxatiemechanismen en wordt de algehele reactie van magnetocalorische slurry (MCS) ingedeeld in twee brede categorieën, namelijk Néel's en Browniaanse relaxatiemechanismen. Aangezien dit werk te maken heeft met een vaste-vloeistof suspensie, wordt een analyse van de kritische neerslagsnelheid uitgevoerd voor het niet-Newtoniaanse mengel van Calorivac - H (LaFeMnSiH) en Galinstan (GaInSn-68.5%21.5%10%). Resultaten verkregen bij verschillende volumefracties en deeltjesgroottes worden gebruikt om ongewenste neerslag van de deeltjes te voorkomen, wat leidt tot hoge wrijvingsverliezen en grote drukgradiënten. Verder wordt een brede kijk gegeven op de modelleringsstrategieën voor vaste-vloeistof systemen, en wordt de voorkeur voor het Euler-Euler mengmodel gerechtvaardigd. Een eindige elementenmethode studie wordt ook uitgevoerd om het dynamische gedrag van een afzonderlijk Calorivac-deeltje te begrijpen. Bovendien wordt het diffusie mengmodel uitvoerig besproken om de fysieke betekenis van elke volumetrische kracht in de huidige context aan te pakken.

De mogelijkheid van magnetisch-aangedreven energietransport wordt eerste geanalyseerd aan de hand van twee onafhankelijke casestudies. Het gedrag van verschillende magnetische

vloeistoffen wordt waargenomen in twee verschillende behuizingen die worden blootgesteld aan een extern aangebracht veld. Het wordt opgemerkt dat in beide gevallen de aanwezigheid van een magnetisch veld leidt tot unieke volumetrische krachten. Dit resulteert uiteindelijk in lokale recirculatiezones die de stromingseigenschappen en warmteoverdracht verder beïnvloeden. Op basis van deze waarnemingen wordt in eerste instantie een koelsysteem met één enkele fase bestudeerd met behulp van verschillende lokale en globale variabelen. De resultaten bevestigen dat de verandering in stromings- en thermische eigenschappen van magnetische koelsystemen evenredig is met de hoeveelheid gebruikte magnetocalorisch materialen en de sterkte van het aangebrachte magnetische veld. Bovendien wordt geconcludeerd dat bij een mengel van 40% Calorivac-H en Galinstan een temperatuurdaling van 1.9 Kelvin wordt verkregen bij 1.03 Tesla. Deze koeling wordt vervolgend verder uitgebreid met behulp van twee verschillende multi-stage opstellingen. Deze multi-stage configuraties werken volgens het cascade-principe en vereisen een warmtewisselaar in combinatie met een magnetisch schild voor hun werking. Een maximale temperatuurspanning van 6.08 Kelvin wordt bereikt met een cascade-opstelling van vijf fasen bij de eerder genoemde bedrijfsomstandigheden. Deze studie toont de mogelijkheid om het beperkende adiabatische temperatuurverschil te overwinnen die inherent is aan verschillende magnetocalorische materialen.

Ter conclusie biedt dit werk waardevolle inzicht in de prestaties van apparaten die werken op het magnetocalorische effect voor koeling bij kamertemperatuur. De resultaten die in dit werk worden gerapporteerd, kunnen dienen als basis om de efficiëntie en compactheid van toekomstige prototypes verder te verbeteren. Bovendien kunnen de ontwikkelde numerieke hulpmiddelen effectief worden gebruikt om het hydrothermische gedrag van elk generiek systeem te begrijpen dat betrokken is bij de wisselwerking tussen magnetische vloeistoffen en externe magnetische velden.

Contents

Summary **i**

Samenvatting **v**

List of Figures **xii**

List of Tables **xviii**

Nomenclature **xix**

1 Introduction **1**

1.1 Background 1

1.2 Room Temperature Cooling & Magneto-Caloric Effect 3

1.3 FerroHydroDynamics & Thermo-Magnetic Convection 6

1.4 Research Objectives & Outline 8

2 Understanding the Magnetic Field Distributions **11**

2.1 Magnetic Field of a Moving Charge 12

2.2 Magnetic Dipole 13

2.2.1 Previous Works 14

2.2.2 Present Numerical Work 15

2.3 Permanent Magnet 17

2.3.1 Earlier Works 18

2.3.2 Present Numerical Work 22
2.4 Solenoid 24
2.4.1 Previous Works 25
2.4.2 Present Work 26

3 Thermo-physical & Magnetic Properties 35
3.1 Magnetic Behaviour of MCS 36
3.2 Density of MCS 40
3.3 Modelling the Thermal Properties of Magnetic Fluids 41
3.3.1 Thermal Conductivity 42
3.3.2 Specific Heat 43
3.4 Rheological Behaviour of MCS 45
3.4.1 Effect of Magnetic Field on Overall Viscosity 46
3.4.2 Comparative Study among Different Non-Newtonian Models 49
3.5 Study of Critical Deposition Velocity 51

4 Modelling Approaches for Solid Liquid Suspensions 57
4.1 Overview of the Existing Methods 57
4.2 DEM Study of an Individual Magnetic Particle 60
4.2.1 Analytical Expression for the Motion of a Particle in a 1D Linear **H** 61
4.2.2 Dynamics of the Calorivac Particle in Different **H** Distributions 63
4.3 Euler-Euler Mixture Model 66
4.3.1 Coupling Strategies and Types of Mixture Models 71
4.4 Formulating the Diffusion Mixture Model 73

5 Realising Magnetically Driven Energy Transport 79
5.1 Overview of Existing Works 80
5.2 Interaction of Ferrofluid with Magnetic Dipole 81
5.2.1 Problem Description and Numerical Methodology 81

5.2.2 Results and Discussions 83
5.3 TMC within a Circular Annulus 87
5.3.1 Problem Description 90
5.3.2 Computational Methodology 92
5.3.3 Results and Discussion 95

6 Prototype Simulations of Cooling Systems 101
6.1 Problem Description 102
6.1.1 Geometrical Details 102
6.1.2 **H** Field Arrangement & Thermo-physical Properties 104
6.2 Computational Methodology 107
6.2.1 Grid Distribution & Grid Convergence Study 107
6.2.2 Model Validation 110
6.2.3 Numerical Method 111
6.3 Results & Discussion 112
6.3.1 Single Stage Arrangement 112
6.3.2 Multi-Stage Arrangement 118
6.3.3 Planar Halbach Array and Magnetic Shielding 120
6.3.4 U Shape Staircase Arrangement 122
6.3.5 Vertically Stacked Circular Arrangement 125

7 Conclusions and Outlook 129
7.1 Concluding Remarks 129
7.2 Recommendations 132

Appendix A Derivation of the MCE 135

Appendix B Magnetic Field Distribution of Finite Solenoid 139

Appendix C Diffusion Mixture Model 143
C.1 Validity of DMM 143

C.2 Limitations of DMM 145

Scientific Output **147**

Acknowledgements **149**

Bibliography **155**

List of Figures

1.1 Schematic of a Persian ice house (a) Sketch by a Dutch traveller Krenelin Bervin (From Mokhlesi [1]) (b) Actual footage of an Yakhchal's vault (From Davis [2]) 2

1.2 Projection of cooling capacity in residential and commercial cooling/air conditioning (From Anderson et al. [6]) 3

1.3 Operational principle of the MCE 5

1.4 Schematic of a magnetically polarized volumetric element in a field gradient $\mathbf{H_0}$ (From Rosensweig [23]) 7

2.1 Magnetic field of an infinitesimal current element 12

2.2 Representation of a magnetic dipole using Ampère model 14

2.3 Geometrical representation for computing the $\mathbf{H}$ of magnetic dipole . . 15

2.4 Grid distribution for computing the $\mathbf{H}$ of a magnetic dipole 15

2.5 H^* distribution for all three locations of magnetic dipole (a) For location A, (b) For location B, (c) For location C 17

2.6 Composition of ferromagnetic material [40] 18

2.7 Magnetic domain of a hard magnetic material 18

2.8 Representation of the symbols used in Equation 2.6 - Equation 2.8 . . . 19

2.9 Comparison of present work (PW) with the analytical work (AW) of McCaig and Clegg [42] and experimental work of Oldenburg et al. [52] (a) On-axis ($x/2a = 0, y/2b = 0$) measurements for H_z, (b) Off-axis ($x/2a \neq 0, y/2b \neq 0$) measurements for H_z, (c) Off-axis ($x/2a \neq 0, y/2b \neq 0$) measurements for H_x, (d) Off-axis ($x/2a \neq 0, y/2b \neq 0$) measurements for H_y 23
2.10 Representation of a thin finite solenoid and its magnetic field distribution 24
2.11 Schematic of the configuration used 26
2.12 Comparison of numerically obtained B_{mag} with our own experimental results at different current magnitudes (a) $I = 10$A, (b) $I = 12$A, (c) $I = 14$A, (d) $I = 16$A, (e) $I = 18$A, (f) $I = 20$A 27
2.13 Comparison of magnetic field distribution from the present work with Labinac et al. [61] in (a) Axial direction for $0 \leq z < L_s$, (b) Axial direction for $z > L_s$, (c) Radial direction 29
2.14 Variation of H_ρ^* for solenoid configuration (a) S1, (b) S2, (c) S3, (d) S4 30
2.15 Variation of H_z^* for solenoid configuration (a) S1, (b) S2, (c) S3, (d) S4 31
2.16 Iso - magnetic field lines at x mid-plane for different L_s/D_s (a) S1, (b) S2, (c) S3, (d) S4. The dashed vertical lines represent the corresponding Ls_{start} and Ls_{end}, and the coloured contour represents the H_z^* 32

3.1 Overview of different types of magnetic responses (From Brandon [69]) . 37
3.2 Classification of major magnetization models used in the literature . . . 38
3.3 Schematic representation of the Néel relaxation mechanism and the Brownian relaxation mechanism 39
3.4 Effect of particle size on relaxation time constant (From Rosensweig [76]) 39
3.5 Variation of specific magnetization with T and applied field for 25.4 wt % of Calorivac in Galinstan 40
3.6 Variation of $\left(\frac{\partial M}{\partial T}\right)_H$ with T and applied field for 25.4 wt % of Calorivac in Galinstan 40

3.7 Comparison of different approaches while computing the ΔT_{ad} (From Mugica et al. [101]) 44

3.8 Variation of C_p with T for Calorivac - H 44

3.9 Effect of different H on the viscosity of MF.(From Bacri et al. [111]) where $\eta_r(H, f) = [\eta(H, f) - \eta(0, 0)]/\eta(0, 0)$, $\bullet \rightarrow$ f = 0 Hz, $\blacksquare \rightarrow$ f = 52 Hz, $\blacktriangle \rightarrow$ f = 150 Hz, $\diamond \rightarrow$ f = 345 Hz, $+ \rightarrow$ f = 645 Hz, $\triangle \rightarrow$ f = 1480 Hz 47

3.10 Schematic of different interactions of magnetic moment and viscous moment (From Singh et al. [112]) 48

3.11 Comparison of different non-Newtonian models to approximate rheology of pure Gn 50

3.12 Classification of different flow stability regimes (From Bbosa et al. [138]) 52

3.13 Effect of volume fraction on the CDV of non-Newtonian Gn for $d_p = 50\mu$m 53

3.14 CDV variation of non-Newtonian Gn with different particle sizes at (a) $\phi_d = 5\%$, (b) $\phi_d = 10\%$, (c) $\phi_d = 20\%$, (d) $\phi_d = 25\%$ 54

3.15 Steps involved to compute Re_p during CDV of Gn 55

4.1 Classification of different types of two phase flows (From Ishii and Hibiki [141]) 58

4.2 Overview of the Lagrangian approach and the Eulerian approach 59

4.3 Modelling approaches for Solid-liquid multiphase systems 60

4.4 Schematic of the domain considered for the DEM study 61

4.5 Comparison of analytical results with the XDEM-based solver for $d_p = 100\mu$m, $\rho = 7200$ kg/m^3, $\chi = 999$ and $\Re = 1000$ (a) Displacement with time, (b) Velocity with time 64

4.6 Comparison of analytical results with the XDEM-based solver for $d_p = 100\mu$m, $\rho = 7200$ kg/m^3, $\chi = 999$ and $\Re_1 = 1000, \Re_2 = 100, \Re_3 = 10, \Re_4 = 1$ (a) Displacement with time, (b) Velocity with time 64

4.7 Comparison of analytical results with the XDEM-based solver for $d_p = 100\mu m$, $\rho = 7200$ kg/m^3, $\chi = 999$ and $\Re_{1x} = 1000, \Re_{2x} = 100, \Re_{3x} = 10, \Re_{4x} = 1, \Re_{1y} = 2000, \Re_{2y} = 200, \Re_{3y} = 20, \Re_{4y} = 2, \Re_{4z} = 4000, \Re_{2z} = 400, \Re_{3z} = 40, \Re_{4z} = 4$ (a) x with time, (b) U_x with time, (c) y with time, (d) U_y with time, (e) z with time, (f) U_z with time 65
4.8 Overview of different coupling approaches 71

5.1 Variation of U_{Mean} at $Ra = 10^6$ for different positions of wire and Mn . 84
5.2 Variation of Nu_{avg} at $Ra = 10^6$ for different positions of wire and Mn . 84
5.3 Comparison of streamline distribution and U_{Mean} contours at $Mn = 1.029 \times 10^{12}$ (With the reference case of $Mn = 0$) 85
5.4 Streamline distribution and U_{Mean} contours for case B 86
5.5 Variation of isotherms for different locations and Mn, where Mn^*, Mn^{**}, Mn^{***} corresponds to $Mn = 6.433 \times 10^{10}, Mn = 2.573 \times 10^{11}$, and $Mn = 1.029 \times 10^{12}$, respectively 88
5.6 Nu_{local} distribution for different locations at $Mn = 6.433 \times 10^{10}$ 89
5.7 Nu_{local} distribution at different Mn for case B 89
5.8 Geometrical representation of present case (Figure not to scale) 89
5.9 Enlarged view of discretized circular annulus 89
5.10 Variation of magneto-caloric properties for different T and B (a) m, (b) $\left(\frac{\partial m}{\partial T}\right)_H$ 91
5.11 Fixed temperature gradients over length of HEX's 95
5.12 Distribution of $H^{'}$ within circular annulus for L/D of 0.125 95
5.13 Power spectrum of U_{avg} for different Br and L/D (For an enlarged version of these figures, all readers are humbly requested to refer Dalvi et al. [176]) 96
5.14 Development of velocity contours over time for different L/D at Br of 1.5 Tesla 98
5.15 Comparison of U_{avg} with L/D for different Br 99
5.16 Comparison of Nu_{avg} with L/D for different Br 99

5.17 Comparison of power spectrum of U_{avg} for L/D of 0.125 at $Br = 1.5$ Tesla (a) With F_B, (b) Without F_B 100

6.1 Schematic of the 3D toroidal prototype 102

6.2 $T-s$ curve of magnetic Brayton cycle for Calorivac - H (From Rajamani [19]) 102

6.3 Description of the 3D U shape domain (not to scale) (a) Iso-metric view with notations for thermodynamic process, (b) Top view 104

6.4 Implementation of the Halbach array for single stage analysis in the OpenFOAM framework (a) Iso-metric contour, (b) **H** variation along the axis of HHEX 105

6.5 Visualization of the Halbach array (From Groot [194]) (a) Direction of the internal field for each distinct magnet, (b) Cross-sectional view of magnetic field distribution 106

6.6 Grid distribution of the considered domain 108

6.7 T variation along the axial centreline for (a) HHEX (flow direction from $Z/D_h = 0$ to $Z/D_h = 30$), (b) CHEX (flow direction from $Z/D_h = 30$ to $Z/D_h = 0$) 109

6.8 Comparison of numerical Δp_m for various U_m with the Darcy–Weisbach equation and Zambrano et al. [147] at different weight fractions (a) For $C_w = 8\%$, (b) For $C_w = 12\%$ 111

6.9 Comparison of T distribution at different volume fractions (a) For $\phi_d = 20\%$, (b) For $\phi_d = 30\%$, (c) For $\phi_d = 40\%$ 114

6.10 Effect of ϕ_d on (a) T stats of HHEX, (b) T stats of Middle buffer, (c) T stats of CHEX, (d) Heat Rejection Rate and Cooling Capacity 115

6.11 $\partial T/\partial n$ distribution in the axial ($z^* = z/D_h$) and angular (θ) direction (a) For $\phi_d = 20\%$ at HHEX, (b) For $\phi_d = 20\%$ at CHEX, (c) For $\phi_d = 30\%$ at HHEX, (d) For $\phi_d = 30\%$ at CHEX, (e) For $\phi_d = 40\%$ at HHEX, (f) For $\phi_d = 40\%$ at CHEX 116

6.12 Comparison of streamlines at different volume fractions (a) For $\phi_d = 20\%$, (b) For $\phi_d = 30\%$, (c) For $\phi_d = 40\%$ 117
6.13 Visualisation of the planar Halbach arrangement. Here, the red and silver colour on the magnet represents the north pole and south pole respectively (From [200]) 120
6.14 Illustration of the magnetic shielding principal 120
6.15 Schematic of the (a) Isometric view for a single stage configuration, (b) Top view for a single stage system, (c) Side view for the entire cascade system, (d) Isometric view for complete multi-stage staircase arrangement. Here, red and dark blue colour in the Halbach array represents the north pole and south pole respectively 122
6.16 Grid distribution for a U shape cascade arrangement; (a) Isometric view, (b) Enlarged view 123
6.17 Temperature distribution along the axial mid-plane of each stage for a U shape based multi-stage cascade arrangement 124
6.18 Schematic of (a) Isometric view for a single stage circular setup, (b) Top view for a single stage configuration, (c) Side view of the entire cascade assembly, (d) Isometric view for a five-stage vertically stacked configuration. Here, red and dark blue colour in the Halbach array represents the north pole and south pole respectively 125
6.19 Angular placement of all HEX for the entire cascade configuration. Here, the innermost circular arc refers to the first stage, and subsequent stages are shown with different radii solely for illustrative purposes 126
6.20 Schematic of the grid distribution for a vertically stacked circular cascade arrangement 126
6.21 Temperature distribution along the axial mid-plane of each stage for a vertically stacked circular cascade arrangement 127

List of Tables

2.1 Information about boundary conditions 16
2.2 Parameters used in the work of Oldenburg et al. [52] 22
2.3 Description of parameters associated with the solenoid configurations . . 28

3.1 Thermo-physical properties of the dispersed phase and the carrier phase used in the present work 41
3.2 Correlations for U_t^* based on varying d_p^* [140] 56

4.1 Overview of recent numerical studies that investigate magnetic fluids using two-phase mixture model 68
4.2 Comparison between the DFM and the DMM 72

5.1 Information about boundary conditions 83
5.2 List of constant value parameters used in the present study 92
5.3 Effect of F_B on U_{avg} and Nu_{avg} for L/D of 0.125 at $Br = 1.5$ Tesla . . 99

6.1 Information about the boundary conditions used in the present work . . 106
6.2 Details of the thermo-physical variables 107
6.3 Details about the grid independence study 108
6.4 Comparison of different materials for IHEX 121

C.1 Magnitude of required parameters 144

Nomenclature

Normal symbols represent scalar quantities and **boldface** symbols represent vector and tensor quantities. Generally, boldface Roman symbols represent vectors, and boldface Greek symbols represent tensor quantities, but this rule is not adhered too strictly. *"Dimensions"* of all the terms are provided in a complete SI base set, i. e. mass (M) in kg, length (L) in meters, time (T) in seconds, temperature (Θ) in Kelvin, and current (I) in Ampere. However, derived SI units are implemented in certain instances to represent the *"units"*, such as Ampere (A), Joule (J), Kelvin (K), Newton (N), Pascal (Pa), Siemens (S), and Weber (Wb).

Acronyms

Symbol	**Description**
AMR	Active Magnetic Regenerator
ASMM	Algebraic Slip Mixture Model
CDV	Critical Deposition Velocity
CHEX	Cold Heat EXchanger
DC	Direct Current
DEM	Discrete Element Method
DFM	Drift Flux Model

DMM	Diffusion Mixture Model
FHD	FerroHydroDynamics
FVM	Finite Volume Method
HHEX	Hot Heat EXchanger
IHEX	Intermediate Heat EXchanger
KFD	Kelvin Force Density
MCE	Magneto-Caloric Effect
MCM	Magneto-Caloric Materials
MCS	Magneto-Caloric Slurry
MF	Magnetic Fluid
MR	Magneto-Rheological Fluid
MRI	Magnetic Resonance Imaging
PDE	Partial Differential Equation
TMC	Thermo-Magnetic Convection
XDEM	eXtended Discrete Element Method

Dimensionless Numbers

Symbol	**Description**	**Definition**
Bi	Biot number	$\frac{hL_c}{\kappa}$
Nu	Nusselt number	$\frac{hL_c}{\kappa}$
Pe	Péclet number	$\frac{D_h U}{\alpha_D}$

Pr	Prandtl number	$\frac{\mu C_p}{\kappa}$
Ra	Rayleigh number	$\frac{g\beta\Delta T L_c^3}{\nu\alpha_D}$
Re_p	Particle Reynolds number	$\frac{\rho_c U_t d_p}{\mu}$

Greek Symbols

Symbol	**Description**	**Dimensions**	**Units**
α_D	Thermal diffusivity	L^2T^{-1}	m^2/s
β	Coefficient of volumetric expansion	Θ^{-1}	1/K
$\mathbf{\Omega}$	Flow vorticity	T^{-1}	rad/s
χ	Magnetic susceptibility	-	-
γ	Density ratio	-	-
Γ_k	Mass source for phase k	MT^{-1}	kg/s
κ	Thermal conductivity	$MLT^{-3}\Theta^{-1}$	W/mK
μ	Dynamic viscosity	$ML^{-1}T^{-1}$	Ns/m
μ_o	Vacuum permeability	$MLT^{-2}I^{-2}$	N/A^2
μ_r	Relative magnetic permeability	-	-
ν	Kinematic viscosity	L^2T^{-1}	m^2/s
ϕ	Volume fraction	-	-
Φ_H	Magnetic scalar potential	I	A
σ	Electrical conductivity	$M^{-1}L^{-3}T^3I^2$	S/m
Υ	Particulate loading	-	-

$\boldsymbol{\tau}$	Stress tensor	$ML^{-1}T^{-2}$	Pa
τ_B	Brownian relaxation time	T	s
τ_{eff}	Effective relaxation time	T	s
τ_G	Gillies shear stress criteria	$ML^{-1}T^{-2}$	Pa
τ_N	Néel's relaxation time	T	s
τ_p	Average particle shear stress	$ML^{-1}T^{-2}$	Pa
τ_w	Wall shear stress	$ML^{-1}T^{-2}$	Pa

Roman Symbols

Symbol	**Description**	**Dimensions**	**Units**
$\mathbf{J}$	Volumetric flux	LT^{-1}	m/s
$\mathbf{U}_{Fk} = \mathbf{U}_{Ik} - \mathbf{U}_k$	Fluctuating velocity of phase k	LT^{-1}	m/s
$\mathbf{U}_{Ik}$	Local velocity of phase k	LT^{-1}	m/s
$\mathbf{U}_{jk} = \mathbf{U}_k - \mathbf{U}_j$	Drift velocity of phase k	LT^{-1}	m/s
$\mathbf{U}_j$	Drift velocity/ velocity of centre of volume	LT^{-1}	m/s
$\mathbf{U}_{mk} = \mathbf{U}_k - \mathbf{U}_m$	Diffusion velocity of phase k	LT^{-1}	m/s
$\mathbf{U}_m$	Mixture velocity/ velocity of mass centre of mixture	LT^{-1}	m/s
Eu	Euler's number	-	-
h	Convective heat transfer coefficient	$MT^{-3}\Theta^{-1}$	W/m^2K
L_c	Characteristic length	L	m
L_d	Distance between 2 particles	L	m

B, $\mathbf{B}$	Magnetic flux density	$MT^{-2}I^{-1}$	Wb/m^2
B_r, $\mathbf{B}_\mathrm{r}$	Remanent flux density	$MT^{-2}I^{-1}$	Wb/m^2
C_p	Specific heat	$L^2T^{-2}\Theta^{-1}$	J/kgK
d_p	Diameter of particle	L	m
e	Specific internal energy	L^2T^{-2}	J/kg
g	Acceleration due to gravity	LT^{-2}	m/s^2
H, $\mathbf{H}$	Magnetic field strength	$L^{-1}I$	A/m
K_B	Boltzmann constant	$ML^2T^{-2}\Theta^{-1}$	J/K
M, $\mathbf{M}$	Magnetization	$L^{-1}I$	A/m
n	Number density	L^{-3}	$1/m^3$
p	Pressure	$ML^{-1}T^{-2}$	Pa
q	Specific heat	L^2T^{-2}	J/kg
T	Temperature	Θ	K
t_p	Particle relaxation time	T	s
U_t	Terminal velocity	LT^{-1}	m/s
w	Specific work	L^2T^{-2}	J/kg

Subscripts

Symbol	**Description**
A_{ad}	Adiabatic A
A_{amb}	Ambient A

A_{atm}	Atmospheric A
A_{avg}	Average of A
A_c	A of continuous phase
A_d	A of dispersed phase
A_{eff}	Effective A
A_{ini}	Initial A
A_k	Relate to phase k
A_l	A of liquid
A_m	Mixture A
A_p	A of particle
A_{sl}	Slip A
A_s	A of solid

Other symbols

Symbol	**Description**
$\dot{A}$	Rate of change of A
$\widetilde{A}$	Surface average of A

CHAPTER 1

Introduction

1.1 Background

Since their birth, modern civilizations have always taken conscious efforts to make human life easier in the harsh climatic conditions of our planet. Specifically, in the hot and arid regions where a relatively colder ambience is an essential need for human survival. This is required not only to regulate the human body temperature but also to preserve valuable food resources. To achieve this, different indigenous cooling/refrigeration techniques have been implemented for food storage and human comfort. The first such practice dates back to 1780 BC, when archaeological proofs confirm the use of an ice house in the Mesopotamia region [3]. Similar evidence has been discovered in China, indicating that analogous setups were in use as early as the 7th century BC. Even today, prototypes of such designs can be found in Iran,

(a) (b)

Figure 1.1: Schematic of a Persian ice house (a) Sketch by a Dutch traveller Krenelin Bervin (From Mokhlesi [1]) (b) Actual footage of an Yakhchal's vault (From Davis [2])

where engineers have effectively used ice pits since 400 BC to store/preserve ice as shown in Figure 1.1. These structures were termed as Yakhchal (Yakh - ice, chal - pit) and were greatly enjoyed by citizens to have ice in hot summers [4].

Over the last 3800 years, we have not only advanced ourselves technologically in this field but have also witnessed a substantial rise in its usage. Currently, almost 17% of the world's total electricity consumption corresponds solely to the cooling and refrigeration sector [5]. As it can be confirmed from Figure 1.2, the overall cooling capacity has more than doubled in the last three decades and is expected to follow the same trend in the upcoming period. Furthermore, the rising demand is non-uniformly distributed across countries and is not restricted to specific regions of the globe. Such large cooling requirements essentially lead to a huge burden on the supply chain ecosystem due to the ongoing energy crisis.

A major part of the aforementioned energy demand comes from the conventional Vapour Compression Refrigeration Cycle (VCRC), which is the most widely used method in today's commercial and domestic cooling/refrigeration/air-conditioning sector. This technology works based on the principle of gas expansion and compression, yielding a versatile temperature range. However, the inefficiencies stemming from

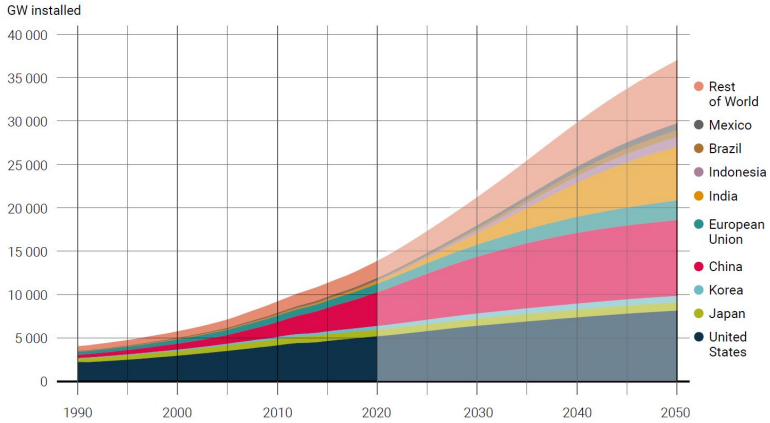

Figure 1.2: Projection of cooling capacity in residential and commercial cooling/air conditioning (From Anderson et al. [6])

compressor-related losses and the use of hazardous substances like chlorofluorocarbons, liquefied ammonia, and hydro-chlorofluorocarbons have cast a shadow over these systems. This technology requires considerable energy input for its operation and is approaching its technical boundaries. Additionally, VCRC has always been criticized for its obligatory use of refrigerants that emit harmful greenhouse gases, resulting in ozone layer depletion. To overcome this, researchers are exploring several alternate techniques [7] that offer a smooth transition in achieving clean energy goals. Such cooling methods can potentially reduce overall greenhouse emissions by 460 billion tonnes in the coming decades [6]. In the present work, one such climate-friendly technique is implemented to obtain a room temperature cooling effect, as discussed in the following sections.

1.2 Room Temperature Cooling & Magneto-Caloric Effect

A significant portion of aforediscussed energy requirement corresponds to the room temperature cooling that need to be addressed. Room temperature cooling is an

important aspect of today's life and will be an inevitable part of our future, due to the temperature rise of our planet by 0.18°C per decade [8]. In an effort to reduce energy consumption and environmental impacts associated with cooling and refrigeration, researchers have been diligently exploring magnetic field-based cooling methods for years [9]. In particular, Magneto-Caloric Effect (MCE) can be used to obtain a room temperature cooling effect as demonstrated by Brown in 1976 [10]. The MCE was first discovered by Auguste Piccard and Pierre Weiss[I] in 1917 [12] and was initially used to obtain near zero temperatures. However, since the seminal work of Brown, MCE has also been actively implemented in the context of room temperature cooling. Over the last few decades, several MCE based working prototypes have been successfully examined for their design and performance [13–15].

MCE is a peculiar phenomenon observed only in specific magnetic materials (MCM) under certain operating conditions. It is often expressed in two different forms i.e. either in terms of an adiabatic temperature change or an isothermal entropy change (as discussed in Appendix A). The total entropy of any solid material can be distinguished under three specific parts as shown below [16]

$$\Delta S = S_{electron}(\mathbf{H}, T) + S_{lattice}(\mathbf{H}, T) + S_{magnetic}(\mathbf{H}, T) \tag{1.1}$$

Here, $S_{electron}(\mathbf{H}, T)$ refers to the entropy change associated with electron spin arrangements, whereas $S_{lattice}(\mathbf{H}, T)$ represents the entropy change caused by the lattice arrangement of atoms. The $S_{magnetic}(\mathbf{H}, T)$ is the magnetic contribution of total entropy change attributed to the random orientation of magnetic dipoles. In an adiabatic condition, if a MCM is exposed to an external magnetic field, its internal magnetic dipoles rearrange themselves (based on its inherent nature as shown in Figure 3.1). This leads to more organized dipoles as shown in Figure 1.3 and hence the decrease of magnetic entropy. However, to compensate for this reduction of $S_{magnetic}(\mathbf{H}, T)$, the $S_{lattice}(\mathbf{H}, T)$ increases (as the $\Delta S = 0$ for an adiabatic

[I] Curious readers are encouraged to visit Pecharsky & Gschneidner [9] and Smith [11] for further details about the interesting history of MCE.

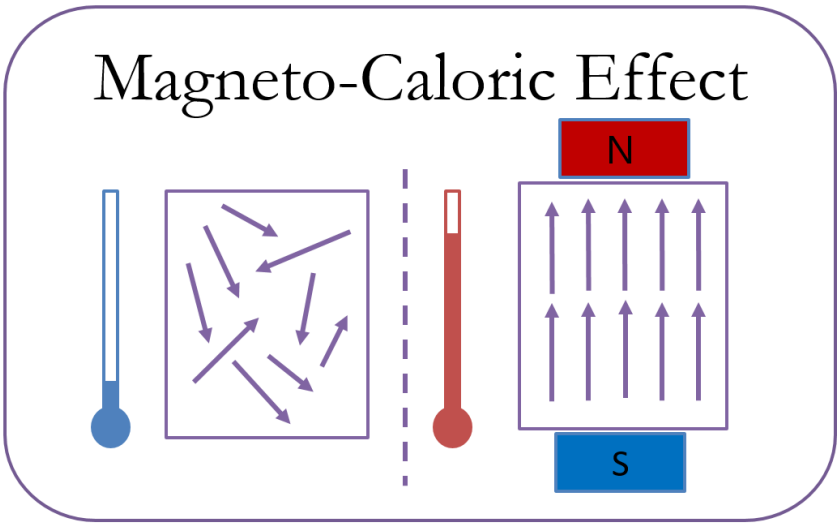

Figure 1.3: Operational principle of the MCE

process), resulting in the elevated temperature of the material. This magnitude of adiabatic temperature rise/drop varies with operating T, type of material, and is proportional to the strength of $\mathbf{H}$. Such implementation of an externally applied field that decreases (increases) the magnetic entropy and leads to an adiabatic increase (decrease) of temperature (referred to as T_{ad}) is essentially known as the Magneto-Caloric Effect (MCE).

Most of the modern magnetic cooling systems that employ MCE work on the principle of Active Magnetic Regenerator (AMR) [17,18]. In such an AMR system, a heat transfer fluid is passed through a porous matrix of MCM materials where MCE is observed. Further, a continuous flow of heat carrier fluid needs to be maintained which requires either reciprocating or rotary arrangements. Due to this mechanical motion, components are subjected to periodic vibrations which can result in frequent maintenance costs and a less reliable system [13]. Also, because of the high initial cost involved for such an assembly, constant efforts are being made by researchers to look for better substitutes. The present work is one such attempt for developing

an MCE based room temperature cooling system without any mechanical motion. To achieve it, the mixture of MCM particles and the heat carrier fluid (termed as Magneto-Caloric Slurry (MCS) in subsequent sections) is passed through the regions of varying magnetic field. The movement of MCS is aimed to be achieved with the help of magnetic pumping as described in Rajamani [19]. The detailed insights on the complete operation of the present system are discussed in Section 6.1.

1.3 FerroHydroDynamics & Thermo-Magnetic Convection

The continuum description of FerroHydroDynamics (FHD) as first defined by Neuringer and Rosensweig [20], deals with the interaction of fluid dynamics and thermodynamics of magnetically polarized fluids. These incompressible fluids often consist of colloidal suspensions of magnetic particles with surfactant coatings to avoid any coalescence even in the presence of considerably strong magnetic fields [21,22]. In the absence of $\mathbf{H}$, despite having individual magnetic moments, the net magnetization of suspended particles is always zero, as they are in continuous Brownian motion. However, when subjected to a magnetic field, the particles try to align their dipoles with the applied magnetic field according to either of the two different relaxation mechanisms (displayed in Figure 3.3). Considering an infinitesimal volumetric element δV of such fluid (having cross-sectional area a_d and width d) within a gradient of magnetic field $\mathbf{H_0}$ as shown in Figure 1.4. The net force acting on one such element can be reported as

$$-\mathbf{H_0}\rho_s a_d + (\mathbf{H_0} + \delta\mathbf{H_0})\,\rho_s a_d = \delta\mathbf{H_0}\rho_s a_d \tag{1.2}$$

Here, $\delta\mathbf{H_0}$ represents the change of applied field along the width and can be rewritten as $(d \cdot \nabla)\,\mathbf{H_0}$ or $(d/\mathbf{M})\,(\mathbf{M} \cdot \nabla)\,\mathbf{H_0}$. Additionally, the magnitude of pole density at both ends is expressed as $\rho_s = \mu_0\mathbf{M}$ [23], where ρ_s refers to the magnetic pole density

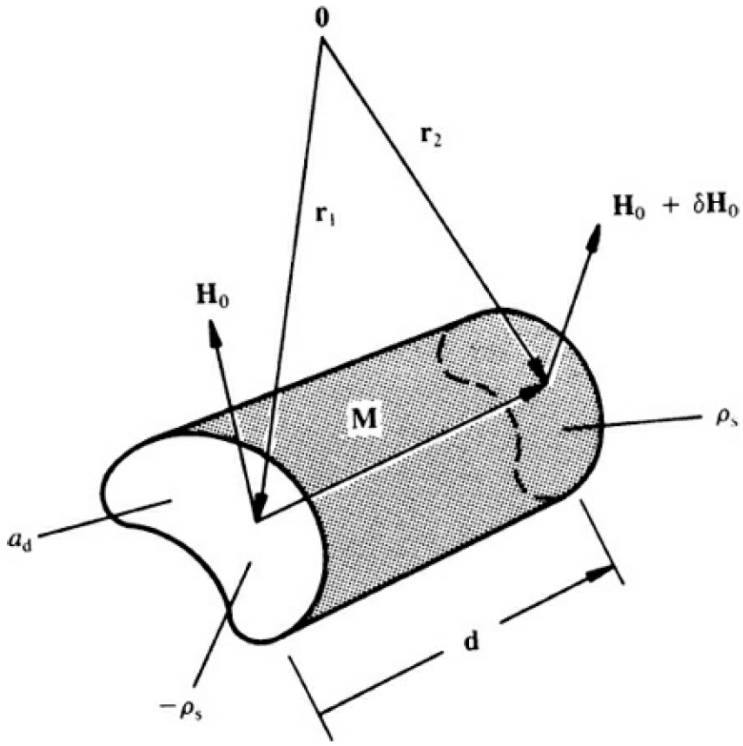

Figure 1.4: Schematic of a magnetically polarized volumetric element in a field gradient $\mathbf{H_0}$ (From Rosensweig [23])

and μ_0 is the magnetic constant. Hence, the acting force can be redefined as:

$$\delta \mathbf{H_0} \rho_s a_d = \mu_0 d \left(\mathbf{M} \cdot \nabla\right) \mathbf{H} a_d \tag{1.3}$$

The aforementioned force if expressed per unit volume simplifies to $\mu_0 \left(\mathbf{M} \cdot \nabla\right) \mathbf{H}$ and is termed as the Kelvin Force Density (KFD). KFD is experienced by every magnetic material in a non-uniform $\mathbf{H}$ distribution which drives them toward the region of a higher magnetic field. Finally, such translational motion of magnetic particles is then transferred to the corresponding Magnetic Fluid (MF) by shear mechanism and rotational friction.

In addition of the $\mathbf{H}$ gradient, if the MF is further exposed to a non-uniform temperature distribution, it exhibits a unique type of heat transfer mechanism

called as Thermo-Magnetic Convection (TMC). TMC is observed significantly for the materials that either have a strong variation of magnetic susceptibility[II] with temperature or have a narrow operational range near T_{Curie}[III]. In conventional fluids, a strong thermal gradient in the gravitational direction results in the considerable density difference leading to buoyancy driven convection. However, due to their magnetic properties, when a MF is exposed to a temperature gradient in the presence of **H**, its magnetic susceptibility varies significantly. This further influence the overall body force acting on the fluid element. Consequently, the distribution of the KFD inside the fluid domain changes which results in TMC. Such peculiar behaviour of MF has been employed by many researchers for several heat and flow transport applications [24–26]

1.4 Research Objectives & Outline

The existing numerical frameworks that can replicate the MCE are developed primarily in the context of AMR. These models frequently rely on simplifications for heat transfer mechanisms and thermophysical properties, thereby constraining their overall validity and adaptability across varying temperature ranges. Thus, the primary objective of the present thesis is to develop a numerical framework that can help in realising a MCE based room temperature cooling device. For achieving this, a computational tool is necessary that accurately interprets the underlying physical processes and their influence on the overall system. In this alignment, an attempt is made to address the following major questions:

- How to precisely obtain the three-dimensional distribution of various magnetic field sources and their dependency on different geometrical parameters?

[II] The extent of magnetization that any material experiences in an external magnetic field is known as magnetic susceptibility.

[III] The temperature at which certain magnetic materials undergo a sharp change in their magnetic properties from a ferromagnetic/ferrimagnetic state to a paramagnetic state, resulting in the loss of their spontaneous magnetization

- What distinct changes are observed in hydro-thermal characteristics due to the complex interaction of magnetic field and magnetic fluid?
- How to simulate a MCE based cooling setup and what are the different possible configurations to enlarge its temperature span?

To resolve the aforementioned queries, the current work is organised in different parts. In the present chapter, a brief introduction to various theoretical aspects is provided along with a historical outlook on the research motivation. The details on different approaches to calculate the magnetic field distribution from different sources are discussed in Chapter 2. Further, the thermophysical and magnetic properties of the present MCS are approximated in accordance with the details from Chapter 3. Additionally, effect of particle size and volume fraction on critical deposition velocity analysis is also discussed to avoid the undesired settling. Chapter 4 provides a generic outlook of the existing solid-liquid modelling strategies and the Euler-Euler approach considered in the present work is explained in great detail. The results of Thermo-Magnetic interactions of magnetic fluid in different enclosed domains are specified in Chapter 5. The performance of a single stage cooling system is reported in Chapter 6 using different local and global flow variables. Two distinct multi-stage configurations are also discussed in continuation with the behaviour of single stage cooling setup. Finally, a concluding remark is provided in Chapter 7 along with a few recommendations for further research.

CHAPTER 2

Understanding the Magnetic Field Distributions

The various physical effects mentioned in the Chapter 1 are observed as a response to the stimuli of an externally applied magnetic field. So, to develop a better understanding of the overall objective, it is first essential to have detailed insights about its original cause. Hence, in the present chapter, the magnetic field distribution obtained from different sources is discussed. Although several possible arrangements are available in the literature to generate a magnetic field, spanning from a thin straight wire to a toroid [27]. However, to keep the present work concise, only specific configurations are discussed which are relevant to the current objective. Beginning with the simplest source of magnetic field, the magnetic field distribution of a moving electric charge is discussed in Section 2.1. Following on the similar line, the field

distribution obtained from a magnetic dipole is explained in Section 2.2. Finally, more complex and widely used magnetic field sources such as permanent magnet, and a finite length solenoid are discussed extensively in Section 2.3 and Section 2.4, respectively. Furthermore, all the numerical results are authenticated with appropriate experimental/analytical/numerical data from the literature.

2.1 Magnetic Field of a Moving Charge

Since the famous discovery of Hans Christian Oersted in 1819, it has been a widely known fact that the flow of electric current produces a simultaneous magnetic field. This coexistence of magnetic field is attributed to the spinning and the orbital motion of electrons as mentioned by André-Marie Ampère. However, it was the

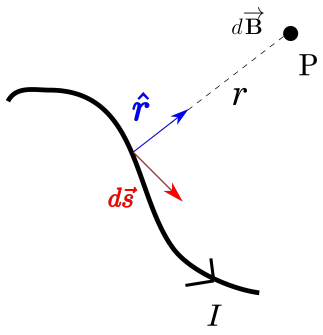

Figure 2.1: Magnetic field of an infinitesimal current element

combined efforts of Jean-Baptiste Biot and Félix Savart that lead to the formulation for magnetic field distribution of an electric charge [28].

Considering an infinitesimally small element $d\vec{s}$ in the same direction of the electric current I as shown in Figure 2.1. The corresponding change of the magnetic flux density $d\overrightarrow{\mathbf{B}}$ at any point P, which is located at a distance r from the element is given by the Biot - Savart law as:

$$d\overrightarrow{\mathbf{B}} = \frac{\mu_o}{4\pi}\frac{Id\vec{s}\times\hat{r}}{r^2} \tag{2.1}$$

The motion of such charged particles via a conducting wire lead to the occurrence of an electric current, which eventually results in the existence of a magnetic field. The exact magnitude of this magnetic flux density in the immediate vicinity of the wire is obtained by integrating small contributions as shown in Equation 2.2

$$\boxed{\overrightarrow{\mathbf{B}} = \int_C d\overrightarrow{\mathbf{B}} = \frac{\mu_o}{4\pi}\int_C \frac{Id\vec{s}\times\hat{r}}{r^2}} \tag{2.2}$$

2.2 Magnetic Dipole

Magnetic dipole can be defined as a pair of magnetic poles that have constant field strength and are kept at a negligible distance from each other. In other words, the flow of the aforementioned electric charge in a miniscule closed loop essentially constitutes a magnetic dipole. The theoretical analogy to classify magnetic dipoles equivalent to electric dipoles (Gilbert model [29]) is not yet completely acceptable, as the magnetic monopoles do not evidently exist in nature. Thus, in classical mechanics, for better understanding, magnetic dipoles are often expressed with tiny current loops (Ampère model) as shown in Figure 2.2. The two different symbols (red and blue) refer to the equivalent poles of a magnet. The strength of these dipoles is expressed via the magnetic dipole moment m, which represents the maximum magnitude of torque experienced by dipoles per unit external magnetic field. This obligates m to the dimensions of $\mathrm{J\,T^{-1}}$, however $\mathrm{A\,m^2}$ is the more widely SI unit

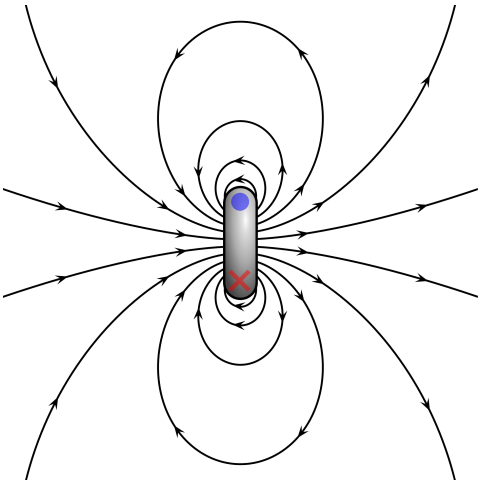

Figure 2.2: Representation of a magnetic dipole using Ampère model

throughout the literature. For an Ampère's model, the dipole moment is simply termed as the product of current magnitude with the area of the loop. On the other hand, for a bar magnet, m is calculated by multiplying the pole strength with the length of the magnet.

2.2.1 Previous Works

Owing to its simple yet significant arrangement, several researchers in the past have employed magnetic dipole to obtain the non-uniform magnetic field. Such uneven field distributions are necessary to stimulate different volumetric forces and hence are essential to study distinct phenomena such as KFD and TMC. Ganguly et al. [30] studied the influence of a dipole on a differentially heated square enclosure filled with magnetic fluid and demonstrated that TMC can be implemented effectively for micro-scale energy transfer. The same configuration is further analysed by Mukhopadhyay et al. [31] and the authors proposed a correlation to predict the Nu in terms of the magnetic Rayleigh number. Ganguly et al. [32] also investigated the influence of magnetic dipoles on forced ferrofluid convection in a 2D channel at a fixed

$Re = 11.8$. Further, an identical domain is simulated by Strek and Jopek [33] but with a parabolic inlet velocity profile, and the authors concluded that there exists a threshold value of H that is required to overcome the viscous forces. Numerical work on the same problem statement is further extended by Goharkhah and Ashjee [34] to understand the effect of different Re and frequency used to control the magnetic dipoles. Moreover, Selimefendigil and Öztop [35] numerically studied the mixed convection in a backward-facing step with a rotating cylinder and demonstrated that magnetic dipoles can alter the length and area of recirculation zones. In addition to the aforementioned studies, other numerical investigations [36, 37] have also been conducted to explore the effect of varying the location and the number of magnetic dipoles on two-dimensional ferrofluid channel flow.

2.2.2 Present Numerical Work

In alignment with the previous works, the non-uniform magnetic field distribution of a magnetic dipole is computed in the OpenFOAM framework [38] using the magnetic

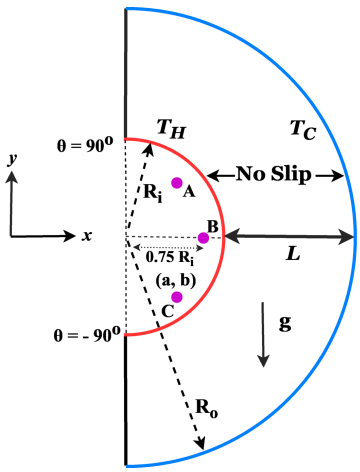

Figure 2.3: Geometrical representation for computing the **H** of magnetic dipole

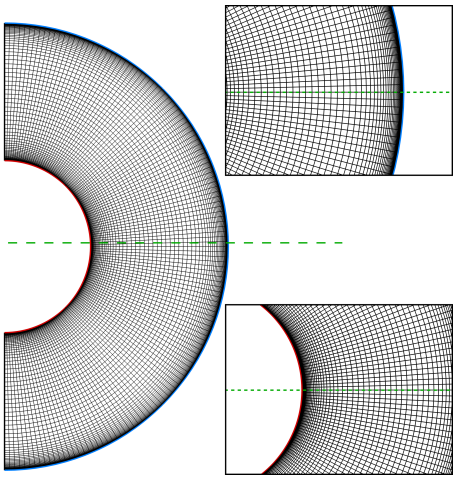

Figure 2.4: Grid distribution for computing the **H** of a magnetic dipole

scalar potential (Φ_H) [39] as shown in Equation 2.3 - Equation 2.5. These equations are used to initialise the **H** field which is then solved with the help of Maxwell's Equation and the boundary conditions shown in Table 2.1.

$$\Phi_H\left(x,y\right) = \frac{\gamma^{\#}}{2\pi}\left[\frac{(x-a)}{(x-a)^2+(y-b)^2}\right] \tag{2.3}$$

$$H_x = -\frac{\partial \Phi_H}{\partial x} = \frac{\gamma^{\#}}{2\pi}\left\{\frac{(x-a)^2-(y-b)^2}{\left[(x-a)^2+(y-b)^2\right]^2}\right\} \tag{2.4}$$

$$H_y = -\frac{\partial \Phi_H}{\partial y} = \frac{\gamma^{\#}}{2\pi}\left\{\frac{2(x-a)(y-b)}{\left[(x-a)^2+(y-b)^2\right]^2}\right\} \tag{2.5}$$

For this, a 2-D semi-circular annulus of a fixed L/D ratio ($L/D = 0.8$) is considered as shown in Figure 2.3, where L is the width of annulus ($L = R_o - R_i$) and D represents the internal diameter ($D = 2R_i$). The semi-circular domain is discretized into a structured non-uniform grid that entirely consists of quadrilateral elements as shown in Figure 2.4.

To capture the large field gradients, fine spacing is also provided near both the walls with a gradual expansion ratio. The non-uniform magnetic field is obtained with the help of a magnetic dipole that is placed at a radial distance of $0.75R_i$ from the centre in three different orientations ($\theta = 60°$ for location A, $\theta = 0°$ for location B, and $\theta = -60°$ for location C). The individual components (H_x and H_y) are defined as a function of their Cartesian coordinates for any specific $\gamma^{\#}$ that is derived from

Table 2.1: Information about boundary conditions

	Inner Wall	Outer Wall	Left walls
M	$Mx, My = 0$	$\partial M/\partial n = 0$	$\partial M/\partial n = 0$
H	$\partial H/\partial n = 0$	$Hx, Hy = 0$	$Hx, Hy = 0$

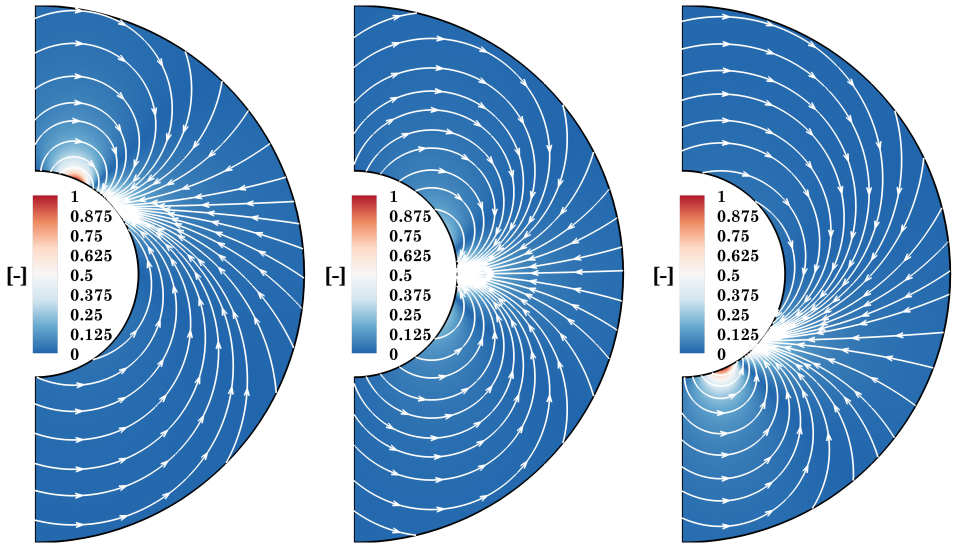

(a) (b) (c)

Figure 2.5: H^* distribution for all three locations of magnetic dipole (a) For location A, (b) For location B, (c) For location C

the corresponding $H^\dagger$. Further, to have a better comparative evaluation, the non-dimensionalised distribution of the strength of magnetic field ($H^* = H/H^\dagger$ where $H = \sqrt{{H_x}^2 + {H_y}^2}$ and $H^\dagger = \gamma^\#/2\pi b$) is shown in Figure 2.5 for all three locations.

2.3 Permanent Magnet

A permanent magnet is essentially the collection of several atomic dipole moments at a microscopic level, which cumulatively results in the formation of a single magnetic domain. Several such magnetic domains are present in a unit volume of a permanent magnet as shown in Figure 2.6. Permanent magnets are usually manufactured from hard magnetic materials[I] that exhibit characteristic behaviour for aforementioned magnetic domains. In the absence of any external magnetic field, numerous dipole

[I] Hard magnetic materials are characterized by their higher B_r and large coercivity (usually greater than $10\,\mathrm{kA\,m^{-1}}$).

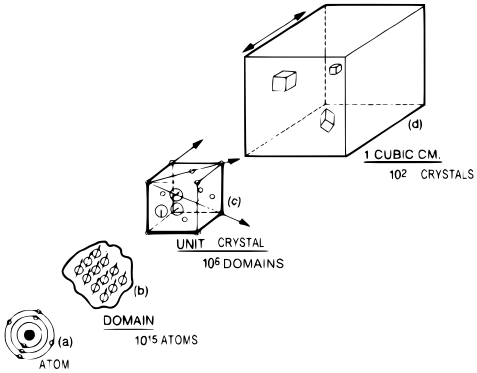

Figure 2.6: Composition of ferromagnetic material [40]

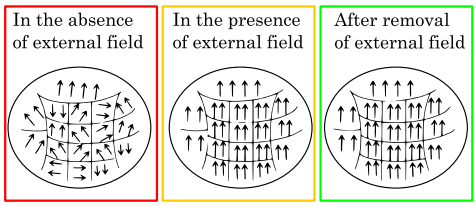

Figure 2.7: Magnetic domain of a hard magnetic material

moments of a hard magnetic material are randomly arranged resulting in zero net magnetization as shown in Figure 2.7. However, once an external magnetic field is applied, all domains align themselves in a same direction, resulting in considerable non-zero magnetization. This intrinsic magnetization exists even after the removal of external field. Such retained magnetic domains are responsible for the variation of the field lines in its vicinity, and hence justifies the prefix "permanent". The ability of permanent magnets to offer magnetic field variation without continuous energy consumption unlike electromagnets is one of the major reasons for its extensive use. Moreover, due to the absence of electric current, Joule heating losses are also avoided and consequently permanent magnets have higher efficiency as compared to other magnetic field sources [15]. This further offers permanent magnets an inherent advantage over other magnetic field sources. An overview of the wide range of applications that employs permanent magnet can be found in the works of Gould [41], McCaig [42], Furlani [43], and Coey [44].

2.3.1 Earlier Works

Several attempts are made to comprehend the magnetic field distribution of a permanent magnet using experimental, numerical as well as analytical methods. Generally,

the field distributions of a permanent magnet are obtained via two approaches namely a magnetic scalar potential (magnetic charge perspective) and a magnetic vector potential (molecular current perspective). In addition to the conventional cuboidal design, several other shapes of permanent magnets such as conical [45,46], arc [47,48], and cylindrical [49–51] are equally studied by the researchers. However, because of its ease of manufacturing, cuboidal-shaped permanent magnets are widely used and are largely investigated in the literature. One of the foremost works to formulate the 3D **H** distribution of a cuboidal permanent magnet is done by McCaig and Clegg [42]. These authors used a magnetic scalar potential approach to obtain the complete non - uniform distribution. Both on-axis and off-axis magnitudes are expressed in all three directions as described in Equation 2.6 - Equation 2.8. The relative positioning of the axes with respect to the magnet and the schematic of the used parameters is shown in Figure 2.8.

Later, Oldenburg et al. [52] carried out experimental work to investigate the field distribution of a cuboidal magnet. Authors measured the on -axis magnitudes of **H** for a specific configuration of the permanent magnet. On the other hand, Xiao et

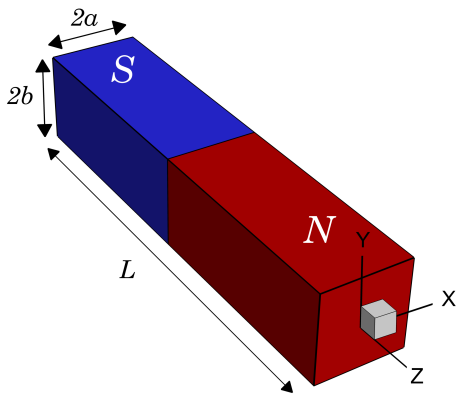

Figure 2.8: Representation of the symbols used in Equation 2.6 - Equation 2.8

al. [53] used a molecular current model to formulate complete analytical distribution based on the Biot - Savart law. Influence of thickness to length ratio of the magnet on the uniformity of field magnitude is discussed in detail. A large magnetic field range of a strong Nd-Fe-B magnet is experimentally studied by Arrott and Templeton [54]. Authors measured the variation of field strength from -2.3 T to 2.3 T across the distance of 0.23 m accurately. Recently, Vervaeke [55] proposed a state-of-the-art high resolution measurement technique to quantify the **H** distribution. All three field components are measured with a high-speed magnetic camera which offers the spatial resolution of 0.01 mm × 0.01 mm at a speed of 120 m s^{-2}.

$$
\begin{aligned}
H_x = \frac{B_r}{4\pi\mu_0}\log_e\Bigg[&\left\{\frac{(y+b)+\left[(y+b)^2+(x-a)^2+z^2\right]^{1/2}}{(y-b)+\left[(y-b)^2+(x-a)^2+z^2\right]^{1/2}}\right\}\times \\
&\left\{\frac{(y-b)+\left[(y-b)^2+(x+a)^2+z^2\right]^{1/2}}{(y+b)+\left[(y+b)^2+(x+a)^2+z^2\right]^{1/2}}\right\}\Bigg] \\
-\frac{B_r}{4\pi\mu_0}\log_e\Bigg[&\left\{\frac{(y+b)+\left[(y+b)^2+(x-a)^2+(z+L)^2\right]^{1/2}}{(y-b)+\left[(y-b)^2+(x-a)^2+(z+L)^2\right]^{1/2}}\right\}\times \\
&\left\{\frac{(y-b)+\left[(y-b)^2+(x+a)^2+(z+L)^2\right]^{1/2}}{(y+b)+\left[(y+b)^2+(x+a)^2+(z+L)^2\right]^{1/2}}\right\}\Bigg]
\end{aligned}
\tag{2.6}
$$

$$
\begin{aligned}
H_y = \frac{B_r}{4\pi\mu_0}\log_e\Bigg[&\left\{\frac{(x+a)+\left[(y-b)^2+(x+a)^2+z^2\right]^{1/2}}{(x-a)+\left[(y-b)^2+(x-a)^2+z^2\right]^{1/2}}\right\}\times \\
&\left\{\frac{(x-a)+\left[(y+b)^2+(x-a)^2+z^2\right]^{1/2}}{(x+a)+\left[(y+b)^2+(x+a)^2+z^2\right]^{1/2}}\right\}\Bigg] \\
-\frac{B_r}{4\pi\mu_0}\log_e\Bigg[&\left\{\frac{(x+a)+\left[(y-b)^2+(x+a)^2+(z+L)^2\right]^{1/2}}{(x-a)+\left[(y-b)^2+(x-a)^2+(z+L)^2\right]^{1/2}}\right\}\times \\
&\left\{\frac{(x-a)+\left[(y+b)^2+(x-a)^2+(z+L)^2\right]^{1/2}}{(x+a)+\left[(y+b)^2+(x+a)^2+(z+L)^2\right]^{1/2}}\right\}\Bigg]
\end{aligned}
\tag{2.7}
$$

$$
\begin{aligned}
H_z = \frac{B_r}{4\pi\mu_0}\log_e\Bigg[&\tan^{-1}\left\{\frac{(x+a)(y+b)}{z\left[(x+a)^2+(y+b)^2+z^2\right]^{1/2}}\right\} \\
&+\tan^{-1}\left\{\frac{(x-a)(y-b)}{z\left[(x-a)^2+(y-b)^2+z^2\right]^{1/2}}\right\} \\
&-\tan^{-1}\left\{\frac{(x+a)(y-b)}{z\left[(x+a)^2+(y-b)^2+z^2\right]^{1/2}}\right\} \\
&-\tan^{-1}\left\{\frac{(x-a)(y-b)}{z\left[(x-a)^2+(y+b)^2+z^2\right]^{1/2}}\right\}\Bigg] \\
-\frac{B_r}{4\pi\mu_0}\log_e\Bigg[&\tan^{-1}\left\{\frac{(x+a)(y+b)}{(z+L)\left[(x+a)^2+(y+b)^2+(z+L)^2\right]^{1/2}}\right\} \\
&+\tan^{-1}\left\{\frac{(x-a)(y-b)}{(z+L)\left[(x-a)^2+(y-b)^2+(z+L)^2\right]^{1/2}}\right\} \\
&-\tan^{-1}\left\{\frac{(x+a)(y-b)}{(z+L)\left[(x+a)^2+(y-b)^2+(z+L)^2\right]^{1/2}}\right\} \\
&-\tan^{-1}\left\{\frac{(x-a)(y-b)}{(z+L)\left[(x-a)^2+(y+b)^2+(z+L)^2\right]^{1/2}}\right\}\Bigg]
\end{aligned}
\tag{2.8}
$$

In addition to its distribution, influence of the obtained magnetic field on the different phenomena is also studied by several researchers. In the context of present work, TMC is one such phenomenon where the permanent magnet has been widely implemented in the literature. Jue [56] performed a numerical study for both magnetic and thermal convection in a 2D square cavity for various values of Ra and Pr. It is concluded that various locations of the magnet along with its intensity can be used for flow regulation in ferrofluids. Zablotsky et al. [57] made a comparison between experimental and numerical results obtained for a ferrofluid cell having permanent magnets attached to its walls. The $K-\omega$ SST model is used to obtain the flow field for a 3D rectangular domain. Authors put forward that maximum thermo-magnetic effect is obtained when the magnets are placed close to the hot end. Ashouri et al. [58] investigated a differentially heated 2-D square cavity in the presence of bar magnet. Authors proposed a correlation of the Nu_{avg} for a broad range of various geometrical

Table 2.2: Parameters used in the work of Oldenburg et al. [52]

Description	Symbol	Magnitude
Remanent flux density	B_{r}	1.19 T
Width of the magnet	$2a$	0.0508 m (2 inch)
Height of the magnet	$2b$	0.0508 m (2 inch)
Length of the magnet	L	0.127 m (5 inch)

and thermophysical parameters. A similar study for high Pr ferrofluid in a 2D cavity with a centrally inserted permanent magnet is conducted by Ashouri and Shafii [59]. Two dominant circulations are observed by the authors which depend on the size of the permanent magnet. Lately, Joubert et al. [60] experimentally investigated the TMC in a differentially heated cavity in the presence of three different permanent magnet configurations.

2.3.2 Present Numerical Work

To compute the 3D distribution of a cuboidal magnet, the existing solver `magneticFoam` is modified in the OpenFOAM framework. For doing so, a magnetic scalar potential (Φ_H) based approach is used such that its gradient is equivalent to the strength of magnetic field $\mathbf{H} = \nabla\Phi_H$. The scalar potential-based approach offers an inherent advantage as it automatically satisfies Ampère's law ($\nabla \times \mathbf{H} = 0$)[II]

$$\nabla \times \mathbf{H} \rightarrow \nabla \times \nabla\Phi_H = 0 \tag{2.9}$$

To authenticate the accuracy of the obtained numerical results, a two-fold comparison is also performed with the experimental work as well as the analytical work present in the literature. The geometrical details and the material properties of the magnet considered for validation study are mentioned in Table 2.2. Primarily, the on-axis measurements are compared with the experimentally available dataset from Oldenburg et al. [52] as shown in Figure 2.9a. Secondly, to further authenticate

[II]The curl of a gradient of a scalar field is always zero.

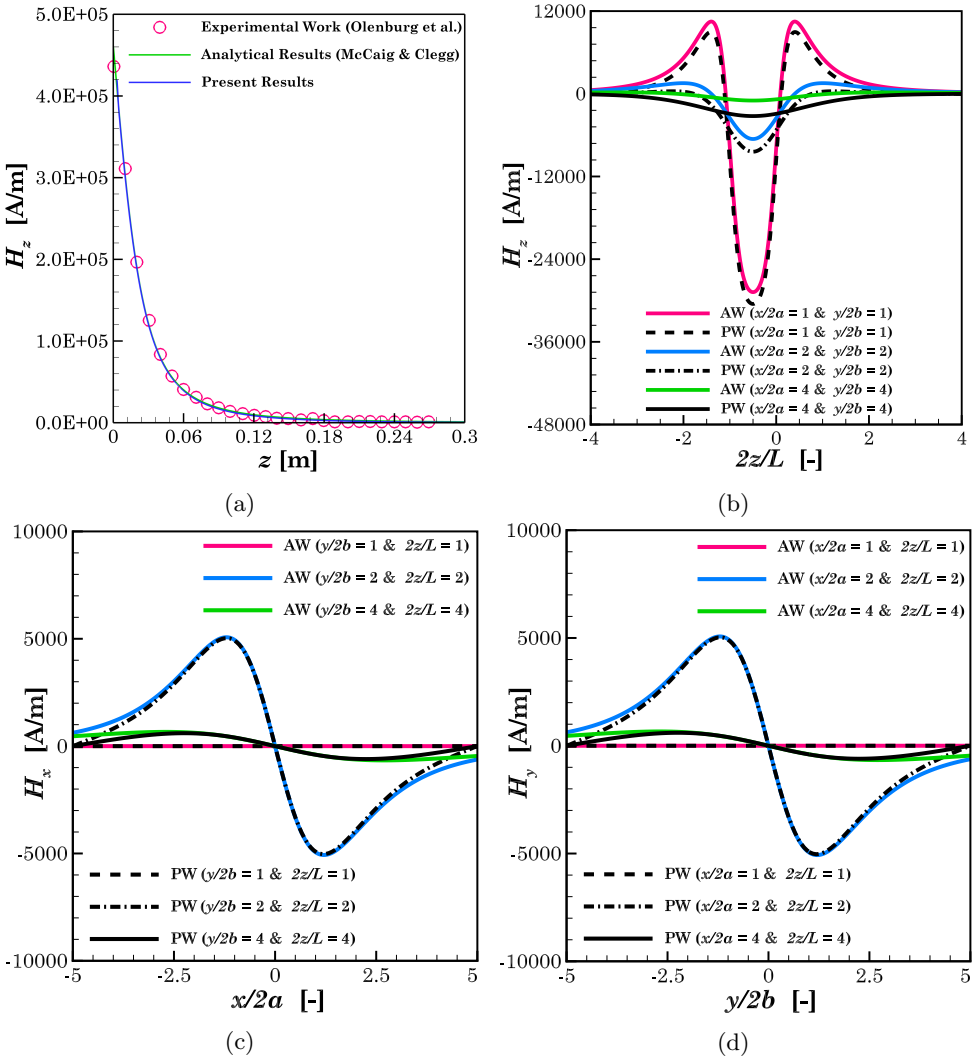

Figure 2.9: Comparison of present work (PW) with the analytical work (AW) of McCaig and Clegg [42] and experimental work of Oldenburg et al. [52] (a) On-axis ($x/2a = 0, y/2b = 0$) measurements for H_z, (b) Off-axis ($x/2a \neq 0, y/2b \neq 0$) measurements for H_z, (c) Off-axis ($x/2a \neq 0, y/2b \neq 0$) measurements for H_x, (d) Off-axis ($x/2a \neq 0, y/2b \neq 0$) measurements for H_y

improved accuracy, the numerically obtained off-axis measurements (of the same permanent magnet configuration mentioned in Table 2.2) are also compared for all

three components. The analytical results used for comparison are obtained using the Equation 2.6 - Equation 2.8 from the work of McCaig and Clegg [42]. As it can be clearly confirmed from Sub-figure 2.9b - Sub-figure 2.9d, the present numerical work provides good agreement with the analytical formulations even at large considerable off-axis distances.

2.4 Solenoid

Solenoid is a specific type of electromagnet where the current carrying wire is wound in a helical shape such that its length is larger than its diameter as shown in Figure 2.10. It is mainly characterised by the total number of turns in the helical coil along with the magnitude of current flowing through it. Although in majority of the research works, the field distribution within the enclosed helical section is always considered uniform (thus neglecting the radial component of magnetic field). However, as demonstrated experimentally [61] and analytically [62], based on its length to

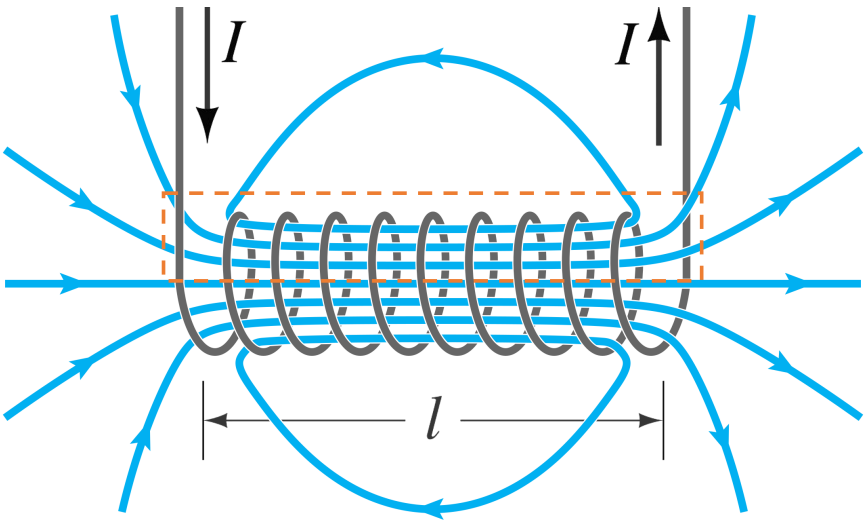

Figure 2.10: Representation of a thin finite solenoid and its magnetic field distribution

diameter ratio, a solenoid exhibits a considerably varying radial (H_ρ) as well as axial (H_z) field distribution. In the context of the present work, we are aiming to employ a finite solenoid to achieve the motion of the working fluid. Hence, it is very essential to investigate its complete distribution.

2.4.1 Previous Works[III]

One of the foremost works on the magnetic field distribution of thin, finite, and a circular cross-sectional solenoid is carried out by Callaghan et al. [62] using magnetic vector potential. Authors derived radial and axial field variations for different lengths and diameters of a solenoid using complete elliptic integrals. Several other studies [50, 61, 64–66] explain these field distributions in a distinct manner using different methods and analytical equations. One of many such works is done by Labinac et al. [61], in which authors discuss about theoretical expressions for the field distribution of a single layer solenoid using various mathematical functions such as the Bessel function, hypergeometric function, and the Legendre polynomials. The aforementioned theoretical expressions are written in the cylindrical coordinates for an azimuthally symmetric solenoid which axially starts from the origin. These field distributions are then generalised by Papadopoulos et al. [67] for a thin solenoid of finite length which can be located arbitrarily anywhere in the axial direction. The generalised distribution is defined using the Bessel functions of the first kind for a solenoid diameter D_s and solenoid length L_s (which extends from z_1 to z_2 such that $z_2 - z_1 = L_s$) with N number of wire turns that carries electric current of magnitude I as shown in Equation 2.10 - Equation 2.12

$$H_\rho = -\frac{D_s N I}{4L_s} \int_0^\infty dk \frac{1}{k} \frac{df(k;z)}{dz} J_1(k\rho) J_1(ka) \tag{2.10}$$

$$H_z = \frac{D_s N I}{4L_s} \int_0^\infty dk f(k;z) J_0(k\rho) J_1(ka) \tag{2.11}$$

[III]This subsection is an excerpt from the published article by Dalvi et al. [63].

where $f(k;z)$ is defined as a piece-wise function based on the value of z as shown below:

$$f(k;z) = \begin{cases} -e^{k(z-z_2)} + e^{k(z-z_1)}, & z \leq z_1 \\ 2 - e^{k(z-z_2)} - e^{-k(z-z_1)}, & z_1 < z \leq z_2 \\ e^{-k(z-z_2)} - e^{-k(z-z_1)}, & z_2 < z \end{cases} \tag{2.12}$$

In addition to the theoretical work, Labinac et al. [61] also performed experimental measurements to understand the non-uniform distribution of a finite solenoid. The measurements are carried out for a specific configuration of single layer solenoid of length 279 mm and radius 150 mm, having 150 turns of copper wire which carries a steady current of 9 A.

2.4.2 Present Work

To obtain the 3D non-uniform distribution of finite solenoid, a custom utility is written in the OpenFOAM that implements the Bessel function based formulations (mentioned in Equation 2.10 - Equation 2.12). Based on the specific inputs provided ($L_s, D_s, N,$ and I), a complete field variation is computed.

To verify the accuracy of the obtained magnetic field distributions, the obtained results are validated with our own experimental results. The measurements are performed for a thin DC finite length solenoid wrapped around a cylindrical pipe that contains no magnetic media (as shown in Figure 2.11). The data is collected with

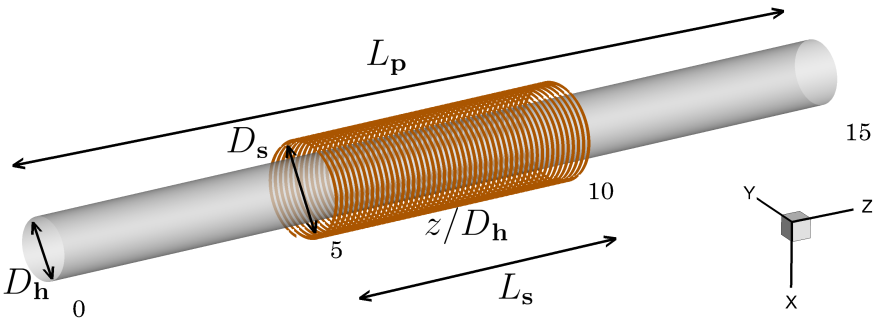

Figure 2.11: Schematic of the configuration used

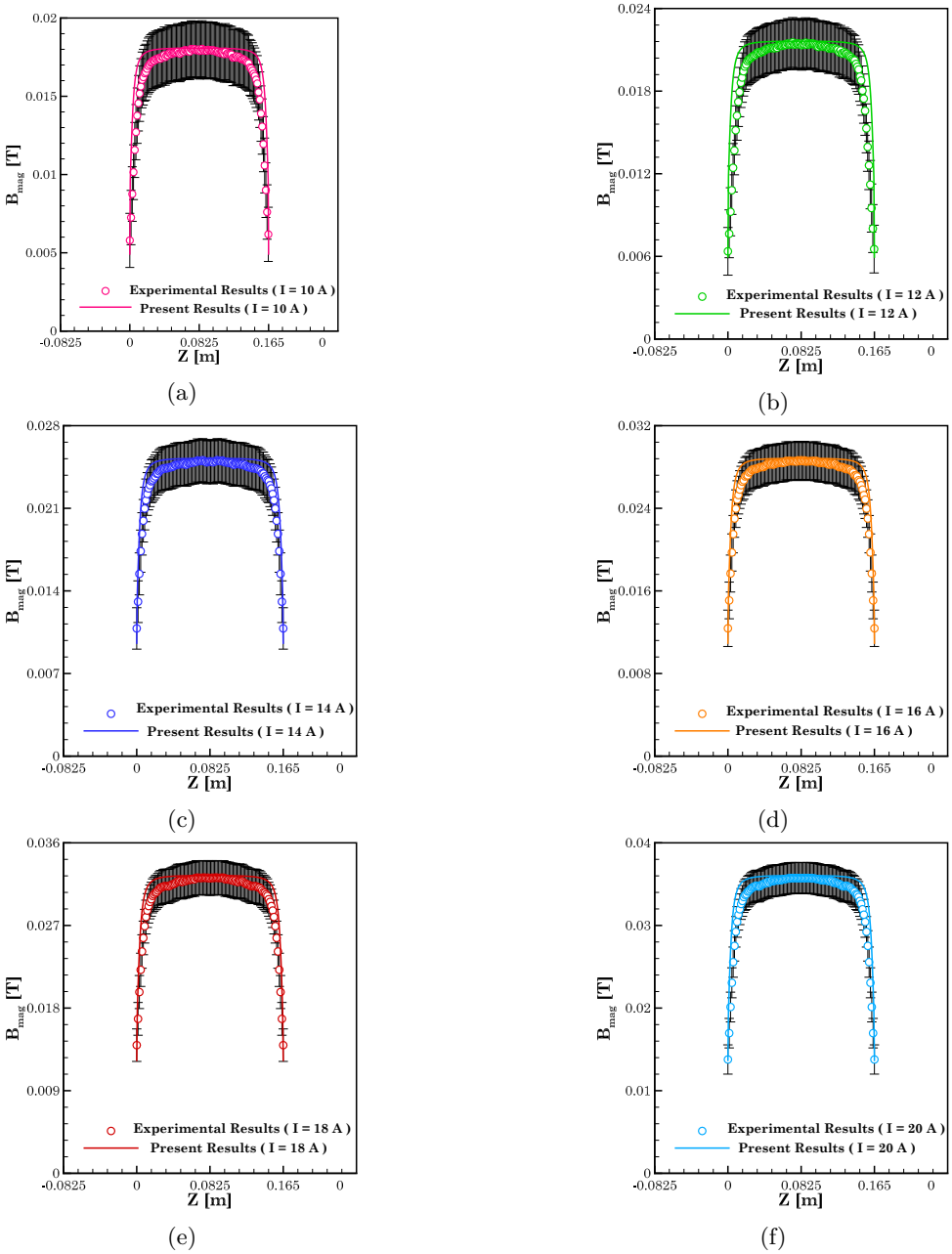

Figure 2.12: Comparison of numerically obtained B_{mag} with our own experimental results at different current magnitudes (a) $I = 10$A, (b) $I = 12$A, (c) $I = 14$A, (d) $I = 16$A, (e) $I = 18$A, (f) $I = 20$A

Table 2.3: Description of parameters associated with the solenoid configurations

Case (L_s/D_s)	Length of Solenoid (L_s)	Diameter of solenoid D_s	Ls_{start}	Ls_{end}
S1	$1D_h$	$4D_h$	$L_p/2 - L_s/2$	$L_p/2 + L_s/2$
S2	$1D_h$	$1.5D_h$	$L_p/2 - L_s/2$	$L_p/2 + L_s/2$
S3	$5D_h$	$4D_h$	$L_p/2 - L_s/2$	$L_p/2 + L_s/2$
S4	$5D_h$	$1.5D_h$	$L_p/2 - L_s/2$	$L_p/2 + L_s/2$

the help of a FM 302 tesla meter along with an AS-NAP axial probe that have an associated measurement error of $0.5\% \pm 0.2$mT [68]. The field magnitude is measured along the axial centreline of specific solenoid with $L_s = 165$mm and $D_s = 6$mm. As it can be clearly observed from the Figure 2.12, even for a wide span of I magnitudes, the current magnitude is well within the bounds of error limit. Additionally, the results are also compared[IV] with (both) the experimental measurements and the theoretical work of Labinac et al. [61]. The radial and axial magnitudes of magnetic field are compared at a specific axial locations, as mentioned in the respective sub - figures of Figure 2.13. It can be confirmed from Figure 2.13 that, the results obtained using the Bessel functions (refer Appendix B) accurately follows the work of Labinac et al. [61] as well as of Callaghan et al. [62].

For better comprehension, four different solenoid configurations (L_s/D_s) (as described in Table 2.3) are also investigated for their radial and axial field distribution. The field obtained for the considered configurations are shown in Figure 2.14 and Figure 2.15, respectively. These distinct distributions are scaled with the length of the pipe ($Z^* = z/L_p$) and the corresponding $H_{max}(H^*_\rho = H_\rho/H_{max},\ H^*_z = H_z/H_{max})$. For all four configurations, both H_ρ and H_z have maximum magnitudes in the vicinity of the solenoid (at $2\rho/D_s = 1$). Additionally, it can be clearly seen from Figure 2.14, at the solenoid surface and near both the edges of the solenoid, the magnitude of H_ρ tends to infinite which reflects from the sharp peaks at Ls_{start} and Ls_{end}. Moreover,

[IV] In the present work, solenoid is wrapped around a pipe and we are mainly concerned about the field distribution inside the solenoid. Thus, comparisons are done only for the radial locations within the circumference of solenoid (up to $2\rho/D_s = 1$).

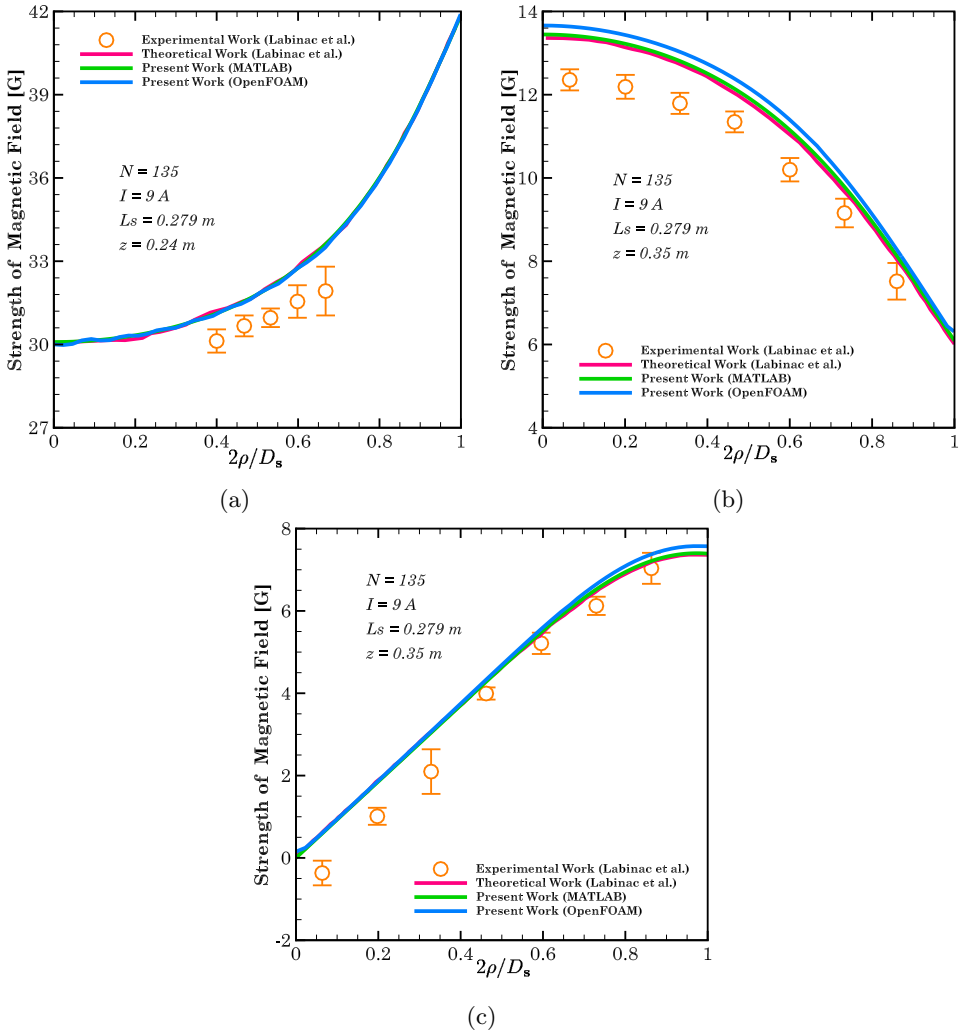

Figure 2.13: Comparison of magnetic field distribution from the present work with Labinac et al. [61] in (a) Axial direction for $0 \leq z < L_s$, (b) Axial direction for $z > L_s$, (c) Radial direction

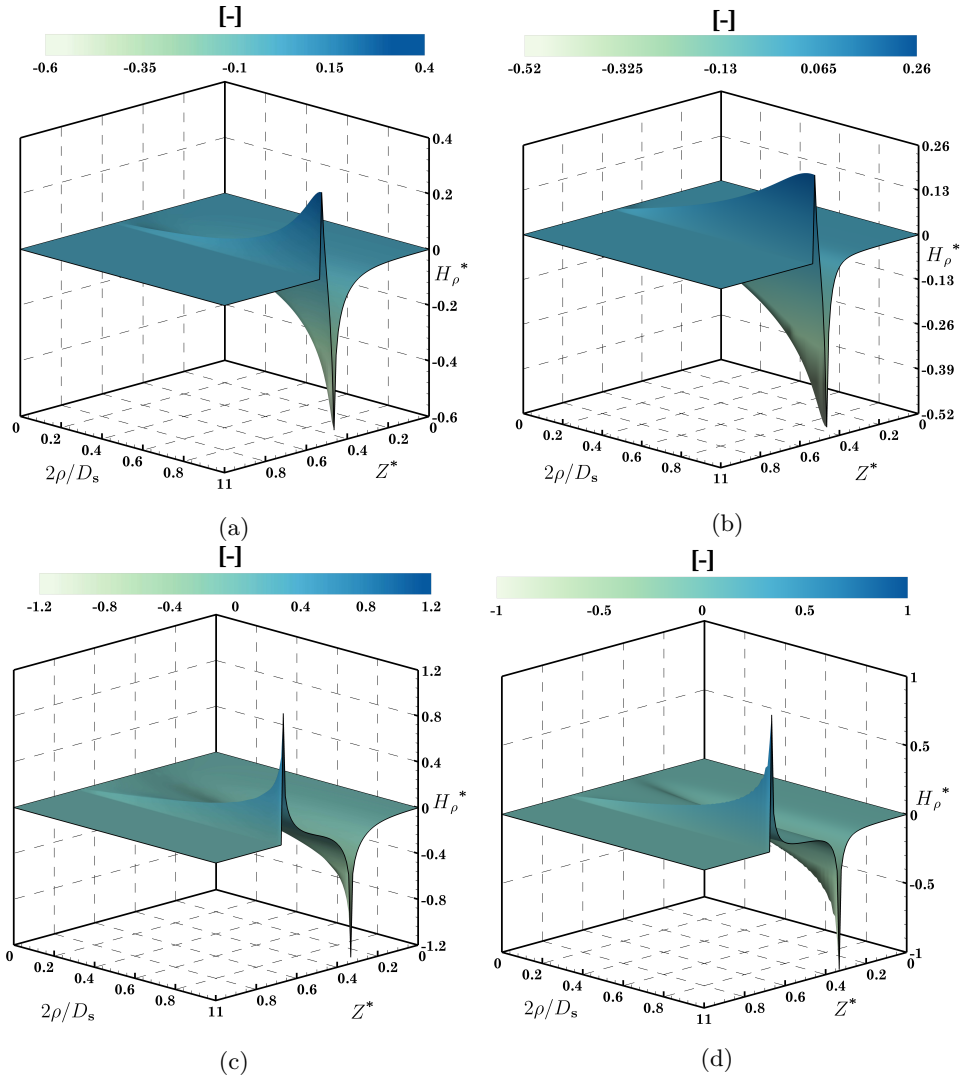

Figure 2.14: Variation of H_ρ^* for solenoid configuration (a) S1, (b) S2, (c) S3, (d) S4

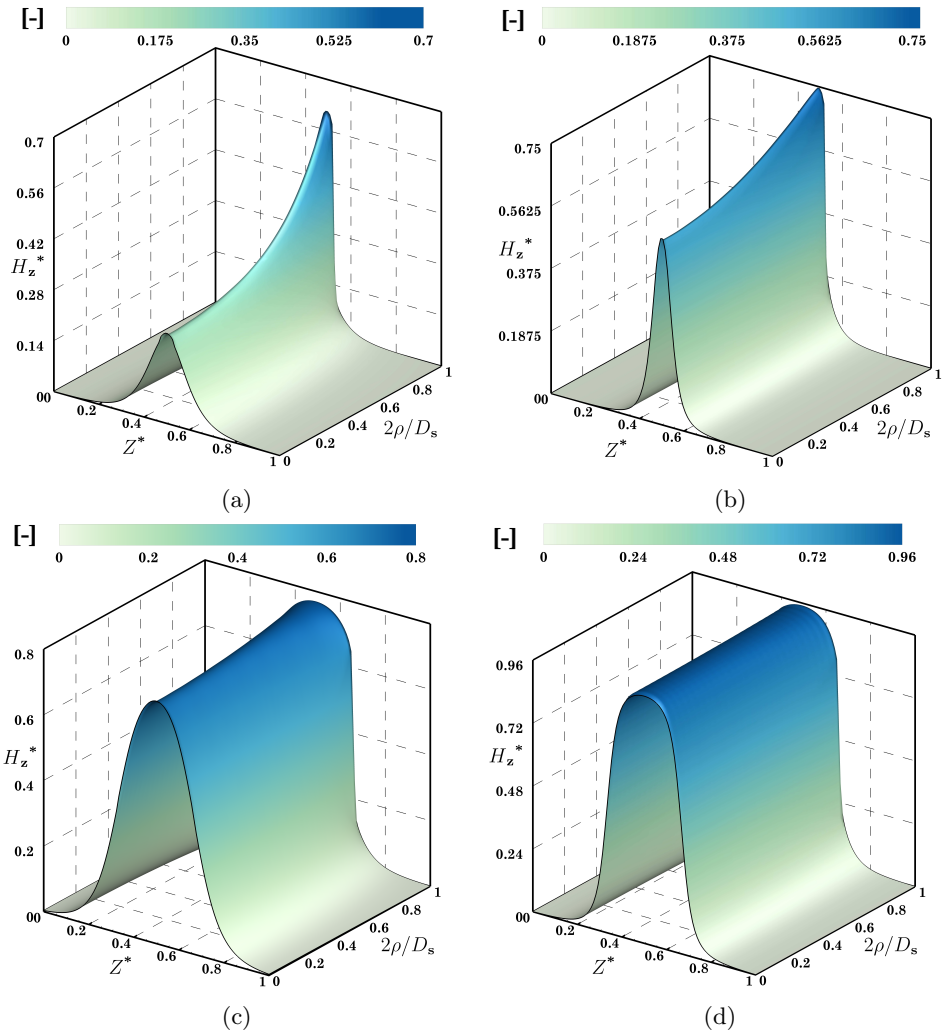

Figure 2.15: Variation of H_z^* for solenoid configuration (a) S1, (b) S2, (c) S3, (d) S4

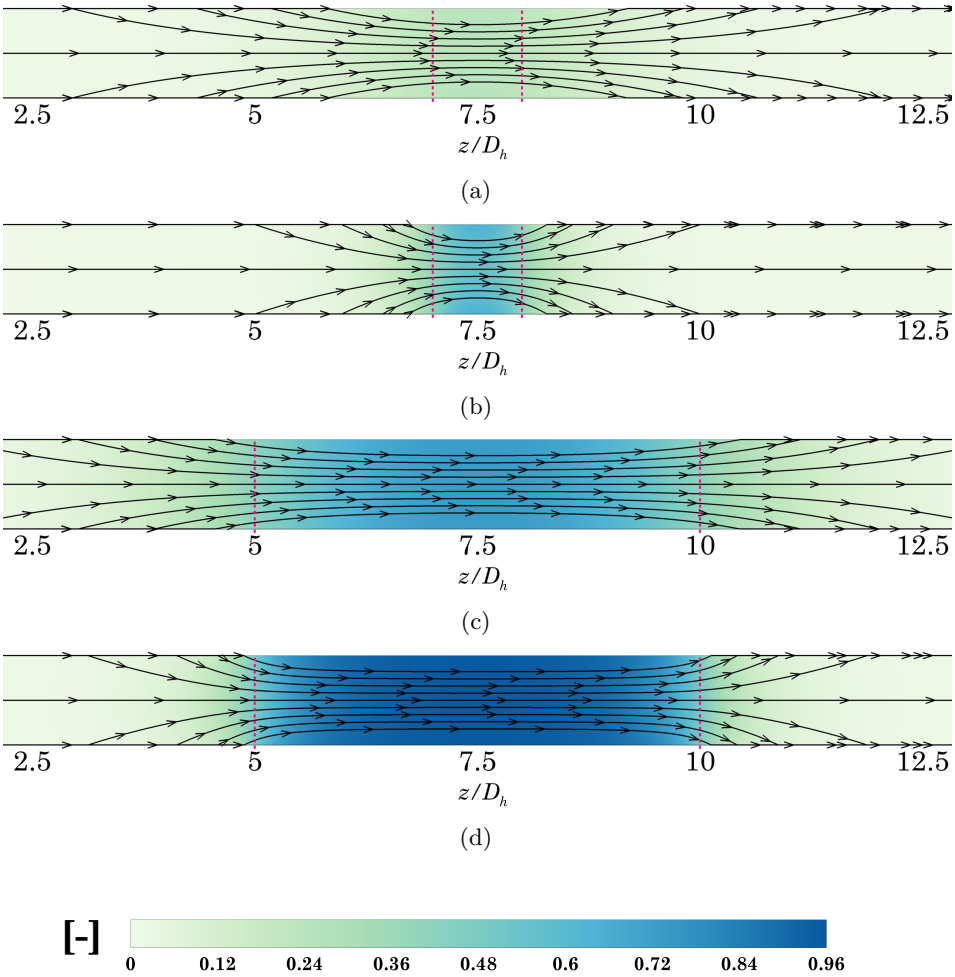

Figure 2.16: Iso - magnetic field lines at x mid-plane for different L_s/D_s (a) S1, (b) S2, (c) S3, (d) S4. The dashed vertical lines represent the corresponding Ls_{start} and Ls_{end}, and the coloured contour represents the H_z^*

at smaller L_s/D_s, there exists a discrepancy between the magnitude of H_ρ at both the ends (Sub-figure 2.14a and Sub-figure 2.14b where $|H_{\rho Ls_{start}}| > |H_{\rho Ls_{end}}|$), and such peculiar behaviour can also be confirmed from the results of Callaghan et al. [62]. Further, it is depicted in Figure 2.15 that, for a specific solenoid length, an increase in D_s leads to the reduced magnitudes of H_z, whereas at a particular solenoid diameter, increase in L_s leads to ascending H_z. It can also be noticed that the radial variation of H_z (from $2\rho/D_s = 0$ to $2\rho/D_s = 1$) decreases with increase in L_s/D_s.

To further support our understanding about the field distribution, the alignment of **H** is also visualised at x mid-plane for all solenoid arrangements. As seen from Figure 2.16, the iso - magnetic field lines completely follow the divergence free behaviour. Additionally, for closely spaced L_s/D_s (S2 and S4), comparatively sharper curvatures are observed around Ls_{start} and Ls_{end} indicating the presence of higher field gradients. In addition to this, the proportional increase of H_z^* magnitude with L_s/D_s is also in agreement with the axial field distribution shown in 2.15.

CHAPTER 3

Thermo-physical & Magnetic Properties

To achieve the present objective of an MCE-based room temperature cooling system, a colloidal suspension of MCM is used as the working fluid. For improved operation/optimization of such a system, it is equally essential to understand its thermo-physical as well as magnetic behaviour at different operating conditions. Thus, in the present chapter, several works are critically analysed to comprehend the influence of various factors on the overall properties of the MCS. Beginning with the magnetic properties (Section 3.1), thermal (Section 3.3) as well as rheological (Section 3.4) behaviour is studied for their dependency on varying particle size, volume fraction, strength, and direction of magnetic field. Finally, a brief analysis on the Critical Deposition Velocity (CDV) is also discussed in Section 3.5 to avoid the

undesired settling of MCM particles.

3.1 Magnetic Behaviour of MCS

The overall magnetic behaviour of MCS can be best approximated by understanding the magnetization. In simplified terms, magnetization can be described as the bulk response of any material to an externally applied magnetic field. The exact nature of this response mainly depends on the electron spin arrangement of atoms, and such peculiar spin arrangements further results in an inherent angular momentum for any material. To be specific, electrons mainly have two different angular momenta i.e. spin angular momentum[I] and the orbital angular momentum[II] where each of them corresponds to the existence of a tiny magnetic moment. A cumulative sum of all such tiny magnetic moments per unit volume represents the overall magnetization $\mathbf{M}$ of the material. An outlook of the five major types of magnetic behaviours is shown in Figure 3.1. The first two (paramagnetism and diamagnetism) do not demonstrate magnetic interaction whereas the last three exhibit long range magnetic order. Generally, all the available materials in nature are inherently diamagnetic, however, its influence is outweighed in case of remaining four configurations.

As shown in Figure 3.1, the particles respond by changing its embedded magnetic moment in either parallel or against the direction of $\mathbf{H}$. This phenomenon of change in alignment of particle magnetic moment can be approximated in two broad categories namely the Quasi-stationary models and the relaxation models. The Quasi-stationary theory assumes that the particles respond to the externally applied $\mathbf{H}$ instantaneously, and hence there does not exist any temporal variation of magnetization i.e. $\partial\mathbf{M}/\partial t = 0$. Such class of magnetization models can be classified as equilibrium magnetization models that only take into account the effect of T, H, ϕ_d, and m. However, the particle magnetic moment always experiences lag while aligning with external $\mathbf{H}$ i.e.

[I] Motion of electrons around its own centre of mass.
[II] Motion of electrons about an external centre such as rotation around the nucleus of an atom.

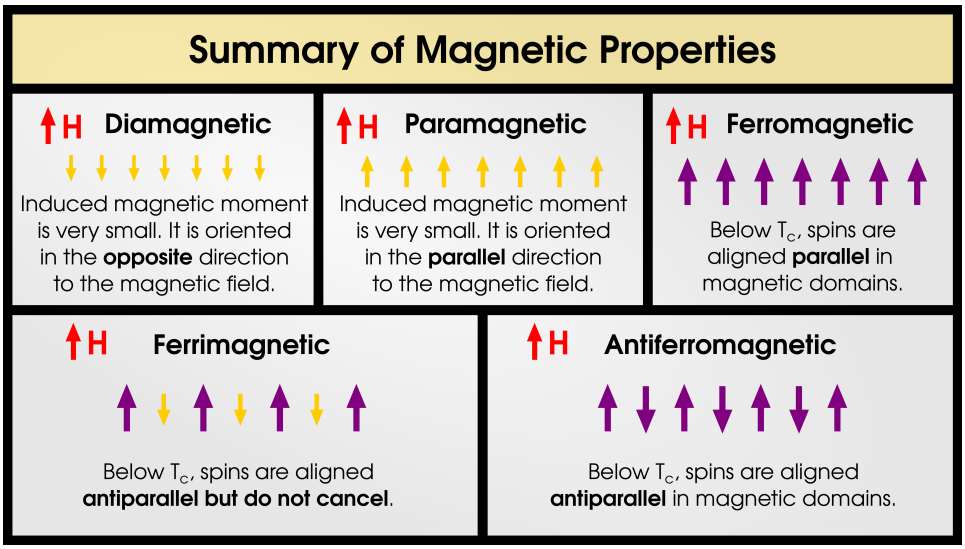

Figure 3.1: Overview of different types of magnetic responses (From Brandon [69])

$\partial \mathbf{M}/\partial t \neq 0$. These classes of magnetization models that considers the influence of the dynamic behaviour of $\mathbf{M}$ can be referred as relaxation magnetization models. In addition to the aforementioned factors, relaxation models also take into account the effect of d_p, flow viscosity η, and flow vorticity $\mathbf{\Omega}$. An overview of the widely used magnetization models in the context of MF is shown in Figure 3.2. For additional insights about the $\mathbf{M}$ equations, readers are encouraged to go through the significant works of Shliomis [70–72]. Further, for both groups of $\mathbf{M}$ models, motion towards the final equilibrium position is achieved via two different mechanisms namely the Brownian relaxation mechanism and the Néel's relaxation mechanism. In Néel's relaxation mechanism, particle rotate its internal magnetic domain to align itself with an externally applied magnetic moment. On the other hand, an actual physical rotation of the particle occurs in case of the Brownian relaxation mechanism. For improved understanding, a schematic of both relaxation mechanisms is shown in Figure 3.3. The formulations for both mechanism are shown in Equation 3.1 and the one with smaller magnitude governs the relaxation process. Moreover, it is

3

Equilibrium Magnetization Models

1. Linear Magnetization Model

$$\mathbf{M} = \chi \mathbf{H}$$

2. T dependent Non - Linear Magnetization Model

$$\mathbf{M} = \chi_m \mathbf{H} \quad \chi_m = \chi_0/[1+\beta(T-T_0)]$$

3. Langevin's Magnetization Model (SuperParaMagentic Model)

$$M_L(H,T,\phi) = \phi M_d \mathcal{L}(\xi)$$

$$\mathcal{L}(\xi) = \coth(\xi) - \xi^{-1}$$

$$\xi = \frac{\mu_0 m \mathrm{H}}{K_B \mathrm{T}}$$

4. Modiefied SuperParaMagentic Model

$$M = \phi M_d \mathcal{L}(\xi_p)$$

$$\mathcal{L}(\xi_p) = \coth(\xi_p) - \xi_p^{-1}$$

$$\xi_p = \frac{\mu_0 m (H + M_\mathrm{L}/3)}{K_B \mathrm{T}}$$

Relaxation Magnetization Models

1. Debye Magnetization Model

$$\frac{\partial \mathbf{M}}{\partial t} + (\mathbf{U}_m \cdot \nabla)\mathbf{M} = \frac{1}{\mathrm{I}}(\mathbf{S} \times \mathbf{M}) - \frac{1}{\tau_{\mathrm{eff}}}\left(\mathbf{M} - \mathrm{M}_0 \frac{\mathbf{H}}{\mathrm{H}}\right)$$

$$\mathrm{M}_0 = nm\mathcal{L}(\xi) \qquad n = \frac{6\phi}{\pi d_p^3}$$

2. Fokker -Planck Equation

$$\frac{d\mathbf{M}^*}{dt} = (\mathbf{\Omega} \times \mathbf{M}^*) - \frac{[\zeta^2 - (\boldsymbol{\xi}\cdot\boldsymbol{\zeta})]}{\tau\zeta^2}\mathbf{M}^* - \frac{[\zeta - \mathcal{L}(\zeta)]}{6\eta\phi\zeta\mathcal{L}^2(\zeta)}[\mathbf{M}^* \times (\mathbf{M}^* \times \mathbf{H})]$$

$$\mathbf{M}^* = \frac{nm\mathcal{L}\ \zeta)\boldsymbol{\zeta}}{\zeta} \qquad \boldsymbol{\zeta} = \frac{m\mathbf{H}_\mathrm{e}}{K_B \mathrm{T}}$$

3. Shliomis' Phenomenological Equation

$$\frac{d\mathbf{H}_\mathrm{e}}{dt} = \mathbf{\Omega} \times \mathbf{H}_\mathrm{e} - \frac{1}{\tau}(\mathbf{H}_\mathrm{e} - \mathbf{H}) - \frac{1}{6\eta\phi}[\mathbf{H}_\mathrm{e} \times (\mathbf{M}^\mathbf{z} \times \mathbf{H})]$$

$$\mathbf{M}^\mathbf{z} = \chi^* \mathbf{H}_\mathrm{e} \quad \text{where} \quad \chi^* = \frac{nm}{K_B \mathrm{T}}$$

Figure 3.2: Classification of major magnetization models used in the literature

also noticed that the particle size significantly influences the relaxation process (as shown in Figure 3.4) and there exists a critical diameter d_p^C for each MF at which $\tau_N = \tau_B$. For $d_p < d_p^C$, particles respond via Néel's relaxation whereas internal moment freezes at $d_p > d_p^C$. Generally, all MF exhibit a non- uniform particle size distribution [23, 73], and it is possible that relaxation can occur simultaneously by both (Néel's and Brownian) mechanisms [74]. Thus, it is advisable to use an effective

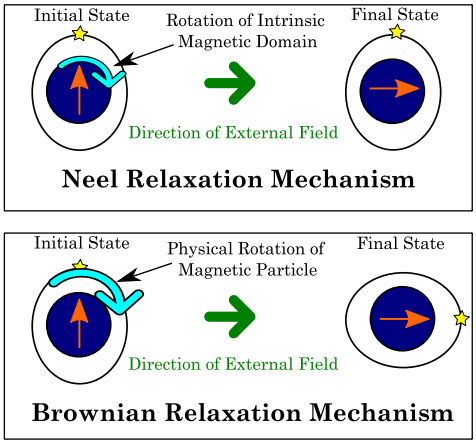

Figure 3.3: Schematic representation of the Néel relaxation mechanism and the Brownian relaxation mechanism

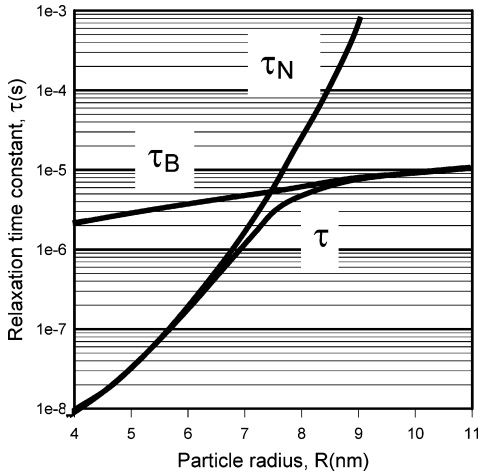

Figure 3.4: Effect of particle size on relaxation time constant (From Rosensweig [76])

magnetic relaxation time constant [75] as mentioned below

$$\boxed{\tau_{\text{eff}} = \frac{\tau_N \tau_B}{\tau_N + \tau_B} \quad \text{where} \quad \tau_N = \frac{1}{f_0} e^{KV/K_B \mathrm{T}} \quad \text{and} \quad \tau_B = \frac{3\mu_{\text{eff}} V_h}{K_B \mathrm{T}}} \tag{3.1}$$

In addition to the parameter **M**, another important magnetic parameter for the present context is the change of magnetization with temperature i.e. $\frac{\partial \mathbf{M}}{\partial T}$. This is mainly because as mentioned earlier, to obtain the desired temperature rise/drop, we are completely relying on the MCE in the present work. As an outcome of MCE, the adiabatic temperature change ΔT_{ad} is computed using the $\frac{\partial \mathbf{M}}{\partial T}$ as shown in Equation A.8. Thus, to compute the ΔT_{ad}, it is essential to accurately follow the variations of $\frac{\partial \mathbf{M}}{\partial T}$. For all MCM, the maximum temperature change occurs near the T_{curie}, where the MCM undergoes a phase transition from ferromagnetic to paramagnetic nature. Due to such sudden transformations, qualitative or often quantitative changes are observed in the magnetic properties of the MCM. To approximate such magnetic properties of MCM near T_{curie}, there exist several Mean Field Theory (MFT) formulations [16, 77]. Additionally, for widely used MCM such as Gadolinium,

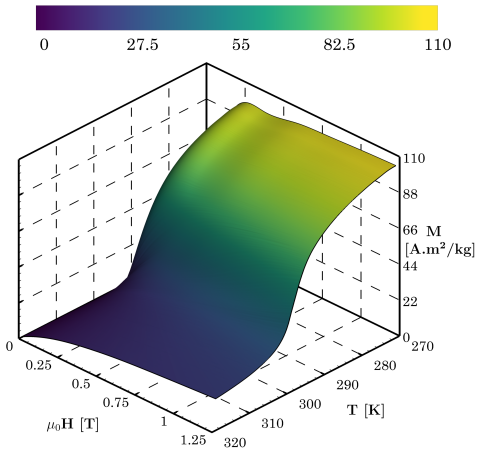

Figure 3.5: Variation of specific magnetization with T and applied field for 25.4 wt % of Calorivac in Galinstan

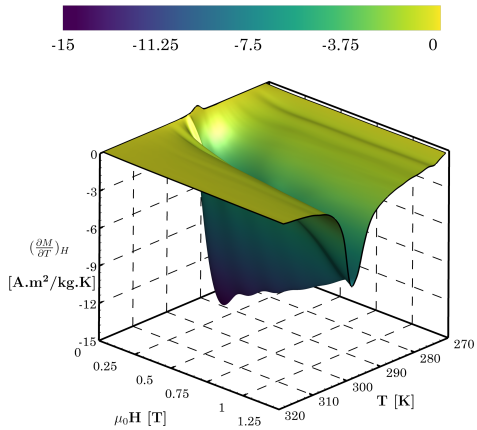

Figure 3.6: Variation of $\left(\frac{\partial M}{\partial T}\right)_H$ with T and applied field for 25.4 wt % of Calorivac in Galinstan

several databases are also available that explain the variation of such properties. However, as described in the later part of this chapter (Figure 3.7), both the MFT's and the available database exhibit considerable difference with the experimentally measured magnitudes. Thus, to avoid aforesaid discrepancy, our own experimental data is used in the present work to model the variations of $\mathbf{M}$ and $\frac{\partial \mathbf{M}}{\partial T}$ for MCS. As shown in Figure 3.5 and Figure 3.6, the measurements are done to consider the influence of both $\mathbf{H}$ and T for a known mixture of Calorivac-H in Gn.

3.2 Density of MCS

Density of any material refers to the bulk amount of matter present per unit volume. Throughout the literature there does not exist sufficient number of numerical/experimental/analytical work that discuss the influence of external magnetic field on the ρ_m. Hence, it is widely accepted knowledge within the community that the applied field does not influence the overall density of the magnetic fluid. However,

Table 3.1: Thermo-physical properties of the dispersed phase and the carrier phase used in the present work

	ρ [kg/m^3]	κ [W/mK]	C_p [J/kgK]
Calorivac - H	7200	7.0	Figure 3.8
Galinstan	6440	16.5	296

recently Ajith et al. [78] reported the decrease in ρ_m of ferrofluid with the exposure to external magnetic field of 350 Gauss for disk shaped $MgFe_2O_4$ nanoparticles. On similar lines, a decrease of ρ_m is outlined experimentally by Zhao and Hu [79] using the Archimedes's principle. Based on the same principle, Hao et al. [80] proposed a potential application in the field of mineral separation that exploits the density reduction of MF in an external field. Nevertheless, these research works are very recent[III] that needs more elaborative discussion on all fronts for wider acceptance. Thus, in alignment with the literature, the density of the MCS is considered to have no influence of magnetic field and is computed with the help of Equation 3.2. As established above, the considered MCS consist of the dispersed (subscript d) solid particles of fixed particle size in a carrier fluid (subscript c). Hence, based on the corresponding ϕ, the overall density of the mixture is formulated using properties of Table 3.1 as shown below:

$$\boxed{\rho_m = \sum_{\alpha=1}^{n} \phi_\alpha \rho_\alpha = \phi_d \rho_d + \phi_c \rho_c = \phi_d \rho_d + (1 - \phi_d)\rho_c} \tag{3.2}$$

3.3 Modelling the Thermal Properties of Magnetic Fluids

[III]Since the inaugural work of FHD in 1964 [20], only three research works are available out of which two are conference papers.

3.3.1 Thermal Conductivity

Due to its significance, there exists an enormous amount of research works [81] that investigate the influence of d_p, ϕ_d, T, particle shape, strength, and direction of $\mathbf{H}$ on the overall κ of magnetic fluids. All the reported results specifically point out the proportional increase of κ with increment in ϕ_d. Additionally, it is also noticed that parallel implementation of external field ($\mathbf{H} \parallel \Delta T$) exhibits a larger increment in κ as compared to the perpendicular arrangement. This is attributed to the formation of particle chains in the direction of H, thus resulting in the anisotropic behaviour of the overall κ. Several formulations have been proposed to approximate this dependency of thermal conductivity on the external magnetic field [82–85]. However, aforesaid research works are done for the smaller d_p (< 100 nm) and at lower ϕ_d ($< 10\%$) [86–88]. Thus, in the context of the present work, as we are dealing with the large ϕ_d of micron size particles, aforementioned results are no longer applicable.

Contrary to the Magnetic Nano-Fluids (MNF)[IV], relatively less literature is available for the magnetic fluids of larger suspended d_p (Magneto-Rheological fluids). However, similar to the MNF, a proportional increase of κ is also observed with larger ϕ_d and the parallel $\mathbf{H}$ configuration [89–91]. One of the foremost works on the thermal conductivity of MR fluids is performed by Shulman et al. [92]. Authors reported the enhanced heat conduction in the direction of the applied field and reduced values for the perpendicular direction. Such anisotropic behaviour of thermal conductivity is also reported in several experimental/numerical works [93,94]. Forero et al. [95] discussed about the association of κ with the μ of MR fluids in the context of carbonyl iron particles in silicon oil. Another interesting work is performed by Reinecke et al. [94] where authors proposed a two-step model to predict the $\mathbf{H}$ dependent rise of κ for a Fe-based MR fluid. However, the proposed model holds a drawback as it requires a parameter that must be supplied from the experimental measurements.

[IV] Often quoted as Ferrofluids, MNF are the colloidal suspension of mono-dispersed magnetic particles of nm size.

From the literature mentioned above, it is established that the observed increment of κ with $\mathbf{H}$ is subjective to the composition of dispersed phase along with the specific ϕ_d and d_p. Hence, it is inaccurate to use such aforementioned correlations for the present MCS as they are derived using the data of other materials. In addition to this, currently, there does not exist a universal model that can approximate κ of the micron-sized magnetic fluids at higher ϕ_d. Hence, for the present case, the effect of $\mathbf{H}$ is not considered while solving the energy equation. However, the effect of dispersed volume fraction ϕ_d is taken into account based on the individual contribution from the dispersed and the carrier phase. To do so, several models are available in the literature such as Maxwell's model [96], Jeffrey's model [97]. However, for the present work, Rayleigh's model [98] (Equation 3.3) is used over its counterparts as it offers accurate results even at higher ϕ_d [15].

$$\boxed{\begin{aligned} &k_m = k_c \left(\frac{\lambda_2 - 2\phi_d - 0.525\lambda_3\phi_d^{10/3}}{\lambda_2 + \phi_d - 0.525\lambda_3\phi_d^{10/3}} \right) \quad \text{where} \\ &\lambda_2 = \frac{2+\lambda_1}{1-\lambda_1}, \quad \lambda_3 = \frac{3-3\lambda_1}{4+3\lambda_1}, \quad \text{and} \quad \lambda_1 = \frac{k_d}{k_c} \end{aligned}} \tag{3.3}$$

3.3.2 Specific Heat

The specific heat corresponds to the amount of energy required to raise the temperature of the considered material by 1K. Hence, each material has its distinct behaviour of C_p with respect to T, and this dependence has been highlighted throughout literature via several correlations/experimental databases. However, analogous to ρ, smaller volume of work is available in the literature on the influence of $\mathbf{H}$ on the C_p of magnetic fluids. Chiu et al. [99] carried out experimental work for a water-based MF at four discrete magnetic fields. Authors reported that C_p decreases with increased $\mathbf{H}$ as the particles shrink at higher fields. On similar lines, micro-calorimeter measurements for a ferrimagnetic system are conducted by Korolev et al. [100]. It is put forward that, there exists an optimum magnetic field range for the considered

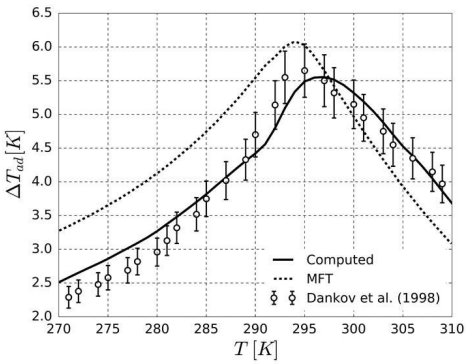

Figure 3.7: Comparison of different approaches while computing the ΔT_{ad} (From Mugica et al. [101])

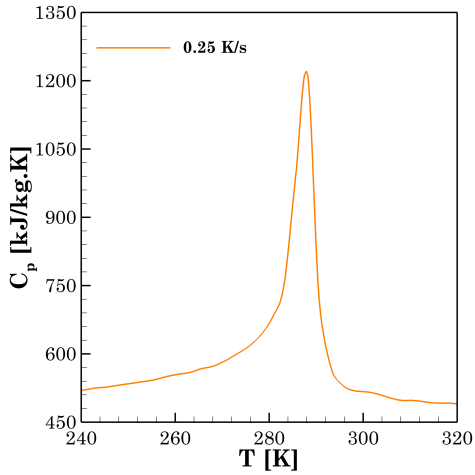

Figure 3.8: Variation of C_p with T for Calorivac - H

MF within which the C_p holds the maximum value. As mentioned in Section 3.1, the maximum MCE occurs near the T_{Curie} where the MCM experiences a phase transition from ferromagnetic to paramagnetic behaviour. Although, different mean field theory approximations are available that can be used to compute the sudden variation of C_p near T_{Curie}. There exists a significant discrepancy between the available databases, MFT's, and the experimental measurements as shown in Figure 3.7. Moreover, as it can be referred from the Equation A.8, C_p contributes significantly for the ΔT_{ad} computation. Thus, in the present work, experimentally measured variation of MCM's specific heat with T is used in the computations (Figure 3.8). Later, the overall specific heat of MCS $(C_p)_m$ is calculated using the formulation shown in Equation 3.4.

$$\boxed{(\rho C_p)_m = \left[(1-\phi_d)\,(\rho C_p)_c\right] + \left[\phi_d\,(\rho C_p)_d\right]} \tag{3.4}$$

3.4 Rheological Behaviour of MCS

Being a colloidal suspension of solid-liquid mixture, rheology of the considered MCS holds a paramount importance. Several parameters such as T, p, ϕ_d, d_p, strength and direction of $\mathbf{H}$ can significantly influence the overall rheology of the MCS. Throughout the literature, it is a well-established observation that the liquid viscosity increases proportionally with p and inversely with T. Additionally, various approximations are available that governs the dependency of μ with T [81]. On similar lines, there also exist several correlations that estimate the increment of μ with ϕ_d. One of the foremost correlations that model the effect of ϕ_d on the viscosity of a solid-liquid suspension is proposed by Einstein [102]. As shown in Equation 3.5, the correlation is only valid for a narrow range of dilute suspensions i.e. $\phi_d < 5\%$. Later, Rosensweig [21] modified it and proposed another expression that offers good predictions for concentrated suspension of up till $\phi_d = 30\%$. Here, the ϕ_{dc} is a critical volume fraction beyond which the results of Equation 3.6 deviates from the experimental measurements.

$$\mu_m = \mu_c \left(1 + \frac{5}{2}\phi_d\right) \tag{3.5}$$

$$\mu_m = \mu_c \left(1 - \frac{5}{2}\phi_d + b\,\phi_d^2\right)^{-1} \text{ where } \quad b = \frac{5/2\,\phi_{dc} - 1}{\phi_{dc}^2} \tag{3.6}$$

For general nanofluids, there exists a mixed observation about the dependency of viscosity on the particle size [103]. On the other hand, based on the limited works available in the context of MF, it can be said that μ of MF increases proportionally with the d_p. Odenbach and Raj [104] studied five ferrofluid samples with different content of large particles. Authors attributed the major contribution of viscosity increment to the larger d_p. An experimental analysis for three different particle sizes of Fe_3O_4 in transformer oil is performed by Shah et al. [105]. It is demonstrated that the increased d_p is responsible for an enhanced yield stress. On identical lines Nowak et al. [106] confirmed that the larger mean particle size exhibits higher increment

in viscosity. Similar investigations are also carried out in the context of Magneto-Rheological (MR) fluids where the d_p of the suspended particles is usually in the microns range [107]. Lemaire et al. [108] noticed that up to a specific high value of $R_{mt} \approx 10^9$ (R_{mt} = Magneto-static energy/Thermal energy), the apparent yield stress of MR fluids increases proportionally with d_p. Also, a same conclusion in put forward by Gans et al. [109] where a d_p bigger than a certain threshold size is observed to have limited influence on viscosity.

3.4.1 Effect of Magnetic Field on Overall Viscosity

Despite all the aforesaid factors, the most critical parameter that can significantly alter μ of MF is an external magnetic field. Magnetic fluids exhibit distinct rheological behaviour based on the nature and strength of the applied magnetic field. MF show an increase in the viscosity under a steady magnetic field, and at low frequency (f) oscillating fields, whereas they experience a reduction in viscosity at higher frequencies ($f > 1/\tau_B$) [110]. For a better understanding, an overview about the influence of different $\mathbf{H}$ on the overall μ of MF is shown in Figure 3.9.

Based on the seminal experimental works of McTague [113], Rosensweig [114], and Hall and Busenberg [115], the increment of μ in the presence of steady $\mathbf{H}$ (magneto-viscous effect) is explained. The rise of flow resistance is mainly attributed to the rotational hindrance of particles in a shear flow. For a magnetically hard particle[V], (as mentioned in Section 3.1) the relaxation will occur via Brownian mechanism. This process of physical particle rotation (ω_p) will get suppressed/encouraged by the flow vorticity ($\mathbf{\Omega}$) based on the respective direction and magnitude of non-zero $\mathbf{H}$. To understand this process in an effective manner, all possible configurations are depicted in Figure 3.10. Later, Shliomis [116] formulated a theoretical model to compute this exact enhancement in viscosity (rotational viscosity or magnetic field-dependent viscosity) for a stationary $\mathbf{H}$. However, the formulation does not

[V] For $d_p > d_p^C$, the internal magnetic moment is frozen.

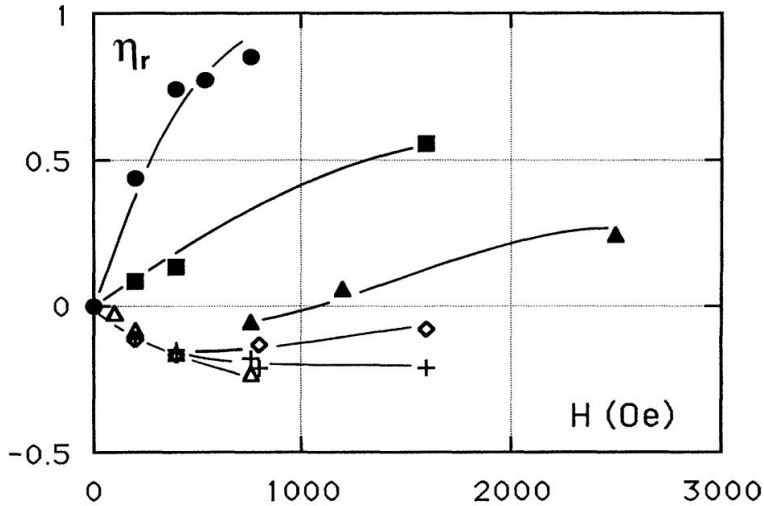

Figure 3.9: Effect of different H on the viscosity of MF.(From Bacri et al. [111]) where $\eta_r(H, f) = [\eta(H, f) - \eta(0, 0)]/\eta(0, 0)$, ● → f = 0 Hz, ■ → f = 52 Hz, ▲ → f = 150 Hz, ◇ → f = 345 Hz, + → f = 645 Hz, △ → f = 1480 Hz

take into account the possibility of Néel relaxation mechanism and inter-particle interaction. A comprehensive review of the numerical/experimental studies that explores the magneto-viscous effect can be accessed through the work of Affiah and Sidik [117].

On the other hand, for an high f oscillating **H**, the reduction in the viscosity is observed after the foremost work of Moskowitz and Rosensweig [118]. A plausible justification for this phenomenon came much later by Bacri et al. [111] via their experimental work. Authors solely held the spin-up mechanism[VI] responsible for the conversion of magnetic energy to the kinetic energy of the fluid. This further results in the enhanced flow rates that are represented in terms of viscosity reductions and hence termed as negative viscosity effect. In addition to the single particle spin-up, the possibility of rotating dimers (fixed-length chain of particles) is also explored by several researchers [74, 119]. This negative viscosity effect is further

[VI] At a sufficiently high oscillating field, the particles will rotate at higher speed than flow vorticity, resulting in the participle spinning

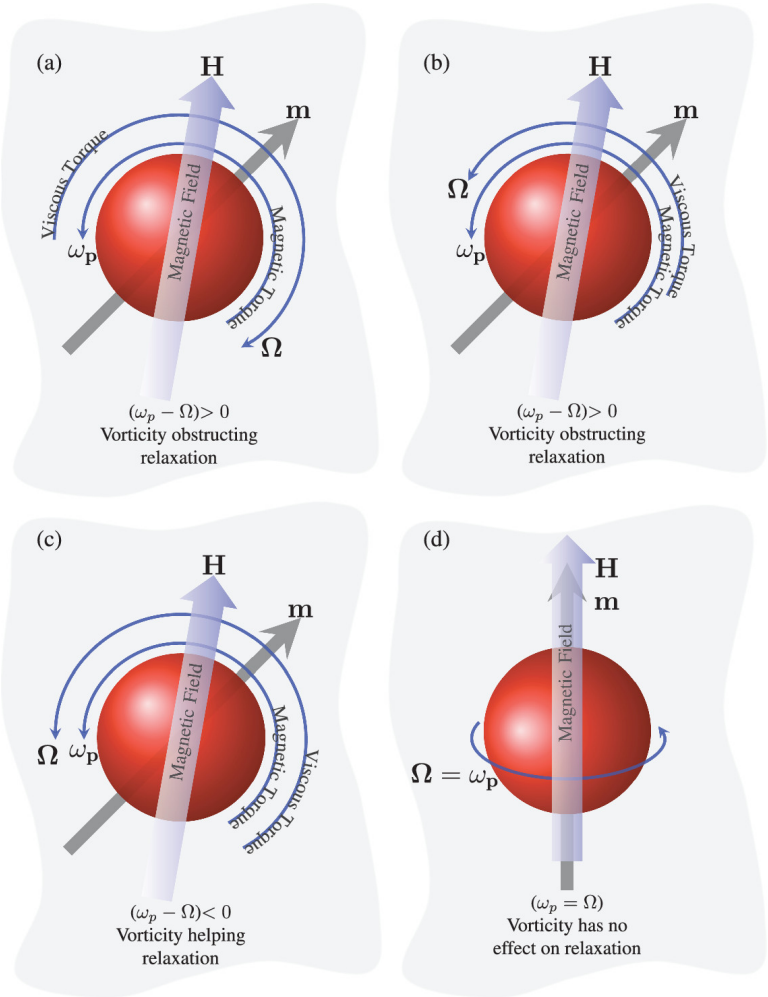

Figure 3.10: Schematic of different interactions of magnetic moment and viscous moment (From Singh et al. [112])

explored by many researchers through experimental [120–123], theoretical [124, 125], and numerical [126–128] works to observe and control the MF behaviour.

For the present MCS, liquid metal Galinstan (Gn) is used as a base liquid with micron-sized suspended particles of Calorivac-H. Hence, the viscosity behaviour of the carrier phase Gn (μ_c) at different shear rates is taken from the experimental work

of Lu et al. [129]. Further, the influence of dispersed phase on the overall viscosity of the mixture (μ_c) is obtained with the help of Thomas's correlation [130] as shown below:

$$\boxed{\mu_m = \mu_c \left(1 + 2.5\phi_d + 10.05\ \phi_d^2 + 0.00273e^{16.6\ \phi_d}\right)} \tag{3.7}$$

Moreover, as the MCS is considered to operate under the influence of an external steady **H** of around 1 T. The final viscosity of MCS (μ_{MCS}) is modelled with the help of Shliomis' correlation (Equation 3.8 - Equation 3.9) that considers the magneto-viscous effect as shown below:

$$\mu_{\text{MCS}} = \mu_m + \Delta\mu_m \tag{3.8}$$

$$\boxed{\begin{gathered}\Delta\mu_m = \frac{3}{2}\phi_d^{'}\mu_m \left(\frac{\xi - \tanh(\xi)}{\xi + \tanh(\xi)}\right) \sin^2 \beta_{\mathbf{\Omega H}} \quad \text{where} \\ \xi = \frac{\mu_0 m \mathrm{H}}{K_B \mathrm{T}} \quad \text{and} \quad \phi_d^{'} = \phi_d \left(\frac{d + 2s}{d}\right)^3\end{gathered}} \tag{3.9}$$

3.4.2 Comparative Study among Different Non-Newtonian Models

As mentioned in the previous section, the rheological behaviour of the Gn in the present work is modelled using the experimental data of Lu et al. [129]. Based on the measurements, authors demonstrated that pure Gn follows a shear rate-dependent viscosity value. This implies that the fluid can no longer be governed by a constant magnitude of viscosity. To approximate such non-linear behaviour, several models are available in the literature. However, we need to perform a careful comparison to finalise the appropriate model that accurately follows the non-Newtonian behaviour of Gn. To do so, three generalised equations (Herschel-Bulkley law (Equation 3.10), Casson law (Equation 3.11), combination of both) are compared against the experimental measurements of shear stress against shear rate.

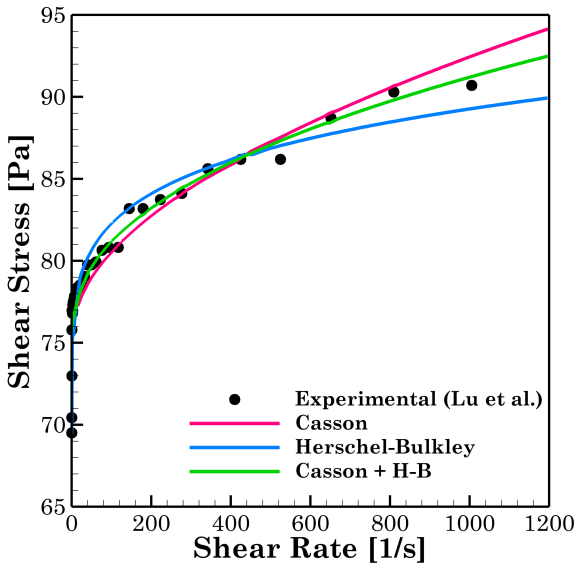

Figure 3.11: Comparison of different non-Newtonian models to approximate rheology of pure Gn

Herschel-Bulkley Equation

$$\tau = \tau_{\mathrm{o}} + k\dot{\gamma}^{n} \tag{3.10}$$

Casson Equation

$$\sqrt{\tau} = \sqrt{\tau_{\mathrm{C}}} + k_{C}\sqrt{\dot{\gamma}} \tag{3.11}$$

In the above equations, τ_{o} and τ_{C} refers to the yield shear stress that needs to be imposed on the fluid to start its deformation (flow). Further, k and k_{C} are proportionality constants, whereas n is the flow index that measures the extent of shear thickening/thinning behaviour. As it can be confirmed from the Figure 3.11, among all three models the Herschel-Bulkley equation correctly follows the non-Newtonian behaviour at smaller shear rates[VII]. Hence, the HB equation is used in the present work, where the effective viscosity is computed as shown below:

[VII] In the present context, we are mainly operating at the bottom end of shear rate spectrum as we are aiming for the absence of any external mechanical motion.

$$\mu_{eff} = \begin{cases} \mu_o & |\dot{\gamma}| \leq \dot{\gamma}_o, \\ \tau_o|\dot{\gamma}|^{-1} + k|\dot{\gamma}|^{n-1} & |\dot{\gamma}| > \dot{\gamma}_o \end{cases} \tag{3.12}$$

Here, μ_o is the limiting viscosity which is obtained as $\mu_o = \tau_o\dot{\gamma}_o^{-1} + k\dot{\gamma}_o^{n-1}$. Finally, this effective viscosity is used as an input (μ_c) to compute the overall viscosity of MCS through Equation 3.7 - Equation 3.9

3.5 Study of Critical Deposition Velocity

Although ferrofluids are synthesized in such a way that they can sustain their colloidal stability for decades[VIII]. However, researchers can not ensure the same for micron-sized particle systems. While dealing with such huge particles, the inertial forces are too large to be overcome by thermal agitations. This ultimately results in the settling/sedimentation of the particles even in a stationary fluid. In the present context of micron-sized suspended MCM, such deposition means a localised heating/cooling which is completely undesirable. Such particle deposition is also troublesome in the general context of solid-liquid transport systems, as it eventually leads to significant pressure gradients and high frictional losses. Thus, a considerable amount of research has been done to avoid the settling of solid-liquid systems by identifying different flow regimes [131–133]. Doron et al. [134] investigated the hydraulic transport of solid-liquid slurry in horizontal pipes using a two-layer model. However, this formulation was unable to correctly predict the occurrence of stationary bed at low mixture velocities. Hence, Dorno and Barnea [135] extended the existing model to take into account the individual bed heights (stationary and moving). This enables the model to correctly predict the existence of stationary bed. Eventually, authors used the same three-layer model formulations to distinguish

[VIII] A high thermal energy ($K_B\ T$) ensures the colloidal stability of MNF. For d_p in orders of nm, even a surfactant of 2 nm increases thermal energy to 20 $K_B\ T$ by increasing steric repulsion energy [107]

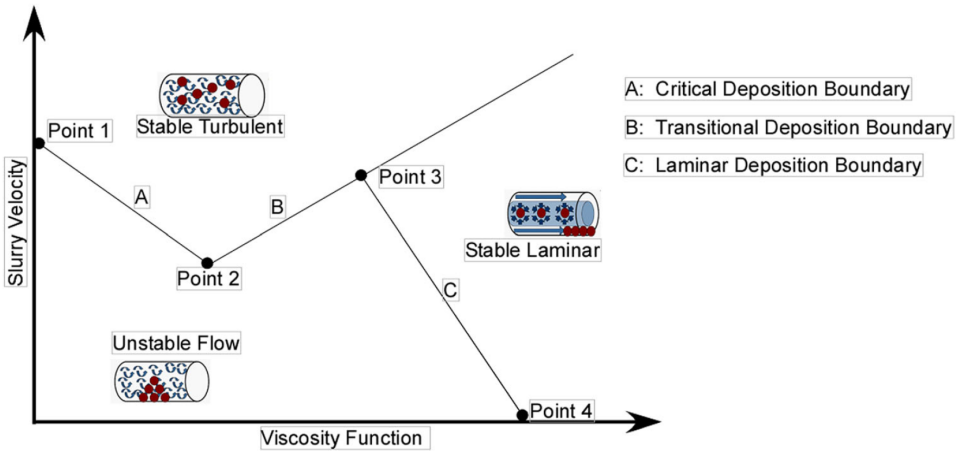

Figure 3.12: Classification of different flow stability regimes (From Bbosa et al. [138])

the four different functioning zones for the case of solid-liquid slurry [136]. Later, Poloski [137] gave a detailed insight into the deposition mechanism of Newtonian and non-Newtonian slurry transport systems. Interested readers are also encouraged to explore a review work on the same subject by Bbosa et al. [138]. As shown in Figure 3.12, a generalised stability map is explained for both Newtonian and non-Newtonian solid-liquid suspensions. Authors suggested the existence of homogenous slurries at higher mixture velocity and smaller rheology, whereas heterogeneous suspensions are predicted at higher yield stress. For the present MCS system, we do not operate in the turbulent regime as the required high flow velocities can not be achieved. Due to the presence of high-yield stresses, the present flow operates within the stable laminar regime, and there exists a concentration gradient in the direction perpendicular to the flow. Because of such a non-uniform distribution of particles, it can also be identified as a heterogeneous flow regime.

The general approach of all the aforementioned works deals with categorization of the operational regimes based on velocity and viscosity magnitudes. Such classification of different flow regimes helps in ensuring the safe operation of solid-liquid transport

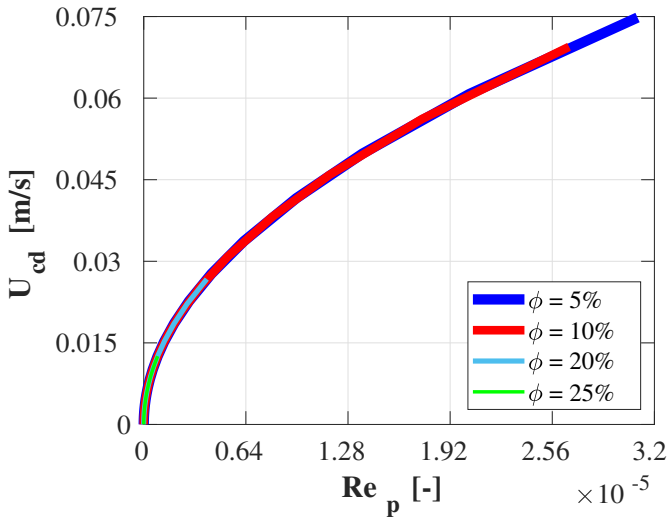

Figure 3.13: Effect of volume fraction on the CDV of non-Newtonian Gn for $d_p = 50\mu m$

systems without sedimentation. The same objective can also be obtained by operating the system above a certain threshold velocity magnitude such as Critical Deposition Velocity (CDV). CDV refers to the minimum velocity that is required by the particles to overcome inertia and avoid the deposition/settling in a stationary fluid. Based on the experimental datasets, there exist several criteria that define different correlations [137] for the CDV of a solid-liquid transport system. One such widely used correlation is proposed by Gillies et al. [139] which uses a threshold ratio (τ_G) of wall shear stress (τ_w) and average particle shear stress (τ_p). Authors put forward that the laminar settling in slurries is significantly reduced when $\tau_G \geq 60$ and completely eliminated for $\tau_G \geq 100$. Thus, using the same criteria and replacing the μ_{eff} in τ_w, we can get a correlation for the critical deposition velocity (U_{cd}) in laminar slurries for non-Newtonian fluids as shown below:

$$\tau_G = \frac{\tau_w}{\tau_p} \quad \text{where} \quad \tau_w = \frac{8\mu U}{D_h} \quad \text{and} \quad \tau_p = \frac{(\rho_s - \rho_f) g d_p}{6} \tag{3.13}$$

$$U_{cd} = \frac{100(\rho_s - \rho_f) g d_p D_h}{48 \mu_{eff}} \tag{3.14}$$

To avoid the aforementioned deposition drawbacks, a CDV analysis is carried out that investigates the influence of ϕ_d and d_p on the particle settling. Initially, the effect of volume fraction is observed at a specific d_p of 50µm. As it can be confirmed from Figure 3.13, U_{cd} shows proportional reduction with increased ϕ. This distinct trend can be easily explained as for a non-Newtonian fluid, yield stress exhibits larger magnitudes at higher ϕ. Such elevated yield stress offers additional resistance for the

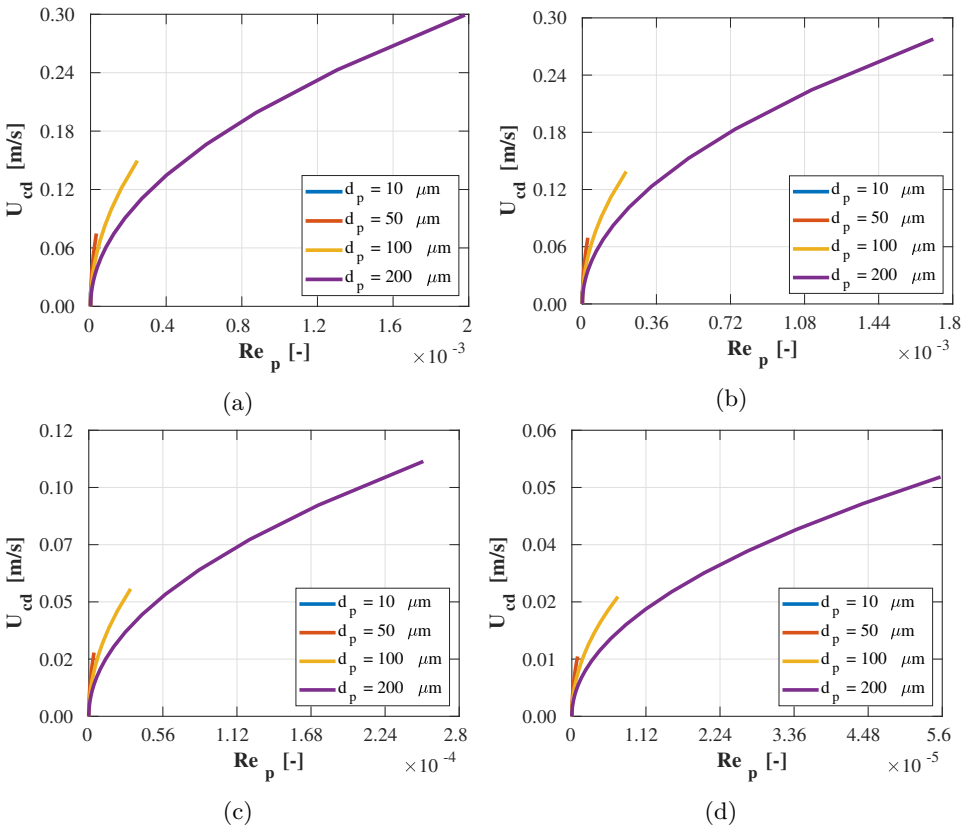

Figure 3.14: CDV variation of non-Newtonian Gn with different particle sizes at (a) $\phi_d = 5\%$, (b) $\phi_d = 10\%$, (c) $\phi_d = 20\%$, (d) $\phi_d = 25\%$

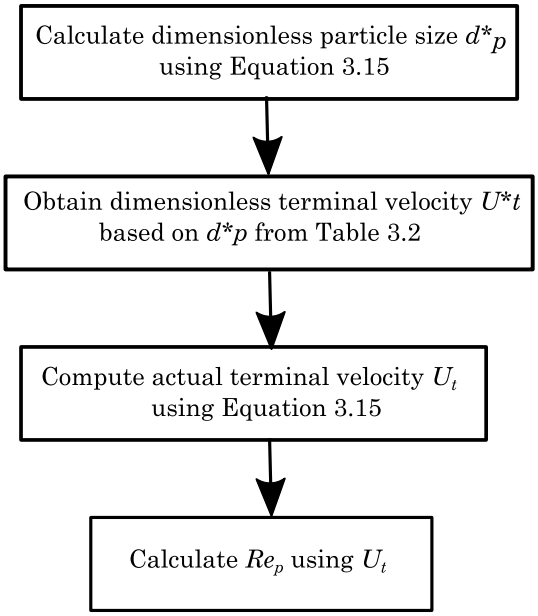

Figure 3.15: Steps involved to compute Re_p during CDV of Gn

settling of particles in a stationary fluid, thus resulting in reduced requirements of U_{cd}. On similar lines, effect of d_p is also studied at all four volume fractions as shown in Figure 3.14. It is noticed that the magnitude of U_{cd} increases with increment in d_p at all four volume fractions. This proportional rise is simply attributed to the higher inertia of larger particles that require increased energy input to avoid settling. For better comprehension, the obtained U_{cd} magnitudes are compared against the particle Reynolds number (Re_p) which is calculated using the Grace method [140] shown in Figure 3.15.

$$\boxed{\begin{aligned} Re_p &= \frac{\rho_c U_t d_p}{\mu_{eff}}, \quad d_p^* = d_p \left[\frac{\rho_f(\rho_s-\rho_f)g}{\mu_{eff}^2}\right]^{1/3} \quad \text{and} \\ U_t^* &= U_t \left[\frac{\rho_f^2}{\mu_{eff}(\rho_s-\rho_f)g}\right]^{1/3} \quad U_t = \frac{(\rho_d-\rho_c)\, d_p^2 g}{18\mu_c} \end{aligned}} \tag{3.15}$$

Table 3.2: Correlations for U_t^* based on varying d_p^* [140]

Range	Correlation
$d_p^* \leq 3.8$	$U_t^* = 1.6415 \times 10^{-6} d_p^{*8} - 3.1234 \times 10^{-5} d_p^{*5} + \frac{d_p^{*2}}{18}$
$3.8 < d_p^* \leq 7.58$	$\log U_t^* = -1.4032(\log d_p^*)^2 + 2.9162 \log d_p^* - 1.5466$
$7.58 < d_p^* \leq 227$	$\log U_t^* = 0.1712(\log d_p^*)^3 - 1.0907(\log d_p^*)^2 + 2.9478 \log d_p^* - 1.6475$
$227 < d_p^* \leq 3500$	$\log U_t^* = -0.1891(\log d_p^*)^3 + 1.687(\log d_p^*)^2 - 4.5103 \log d_p^* + 5.1837$

To conclude, for safe operation of the considered MCS system, there exists an upper limit on the d_p, whereas a higher ϕ is favourable to prevent settling effects.

CHAPTER 4

Modelling Approaches for Solid Liquid Suspensions

4.1 Overview of the Existing Methods

Multiphase flows are often referred to the mixture of two or more distinct thermodynamics phases (solid, liquid, and gas) present inside a physical domain. Such flows are broadly categorized in three major sections based on their structure of interface [141] as shown in Figure 4.1. When the inter-facial length scale (particle size, droplet size, or bubble size) is much smaller than the length scale of the resolved flow, the mixture is referred to be dispersed flow such as solid-liquid slurry, bubble column. On the other hand, if the inter-facial length scale is of equal order to the length scale of considered domain, the flow is examined as separated flows, for ex - sloshing

Class	Typical regimes	Geometry	Configuration	Examples
Separated flows	Film flow	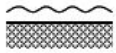	Liquid film in gas Gas film in liquid	Film condensation Film boiling
	Annular flow	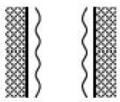	Liquid core and gas film Gas core and liquid film	Film boiling Boilers
	Jet flow		Liquid jet in gas Gas jet in liquid	Atomization Jet condenser
Mixed or Transitional flows	Cap, Slug or Churn-turbulent flow	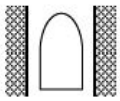	Gas pocket in liquid	Sodium boiling in forced convection
	Bubbly annular flow	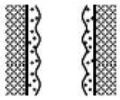	Gas bubbles in liquid film with gas core	Evaporators with wall nucleation
	Droplet annular flow	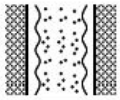	Gas core with droplets and liquid film	Steam generator
	Bubbly droplet annular flow	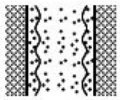	Gas core with droplets and liquid film with gas bubbles	Boiling nuclear reactor channel
Dispersed flows	Bubbly flow	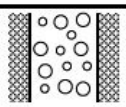	Gas bubbles in liquid	Chemical reactors
	Droplet flow	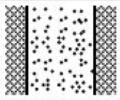	Liquid droplets in gas	Spray cooling
	Particulate flow	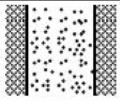	Solid particles in gas or liquid	Transportation of powder

Figure 4.1: Classification of different types of two phase flows (From Ishii and Hibiki [141])

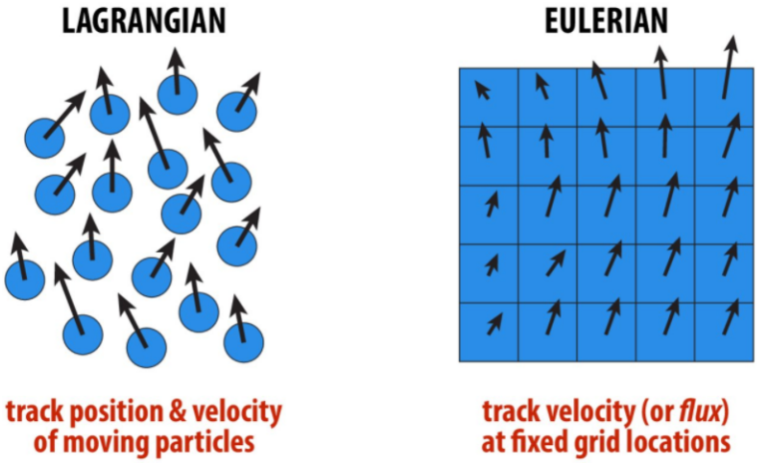

Figure 4.2: Overview of the Lagrangian approach and the Eulerian approach

tanks, jet sprays, etc. The simultaneous occurrence of both the aforementioned flow patterns is identified as a transitional flow regime.

For the present considered case, the suspension of Calorivac-H particles within a base fluid Galinstan lies under the category of dispersed flows. Now, there exists mainly two broad approaches to approximate this intricate behaviour of dispersed flows i.e the Lagrangian approach and the Eulerian approach. As shown in Figure 4.2, in the former method the fluid phase is treated as a continuous media whereas every individual dispersed particle is analysed by integrating the equation of motion along its path. On the other hand, in the Eulerian approach all the phases are treated as a continuous media whose behaviour are investigated using the conservation laws of continuum mechanics. Based on these two aforementioned approaches, a wide range of modelling strategies can be implemented to analyse any solid-liquid system as described in Figure 4.3. However, as the discrete phase volume fraction of the present work is more than 10%, the Lagrangian approach (tracking discrete motion of each particle) is not computationally advisable. Hence, to replicate the response of our complete system, an Eulerian formulation is used in the present work. Nevertheless,

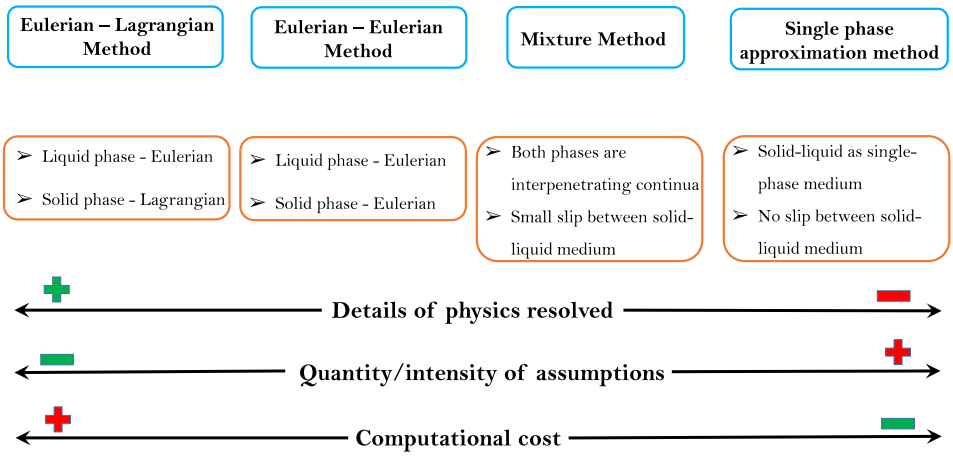

Figure 4.3: Modelling approaches for Solid-liquid multiphase systems

to complement our understanding at the particle scale, a preliminary study is carried out using the Discrete Element Method that follows the Lagrangian approach.

4.2 DEM Study of an Individual Magnetic Particle

For better insights on our MCM suspended room temperature cooling system, it is essential to observe the behaviour of each magnetic particle. However, due to an enormous associated computational cost, only a single magnetic particle is discussed in the present introductory work. To do so, the dynamics of an individual particle is assessed in the presence of distinct **H** distributions. Specifically, the motion of a stationary 100µm Calorivac particle is observed (as shown in Figure 4.4) with the help of an eXtended Discrete Element Method (XDEM)[I] code [142]. Owing to the non-uniform **H** distribution, the KFD experienced by the Calorivac particle is resolved

[I]The Extended Discrete Element Method (XDEM) refers to a numerical approach that extends the classical discrete element analysis by considering additional variables such as the thermodynamic state, stress/strain, or electromagnetic field of each particle.

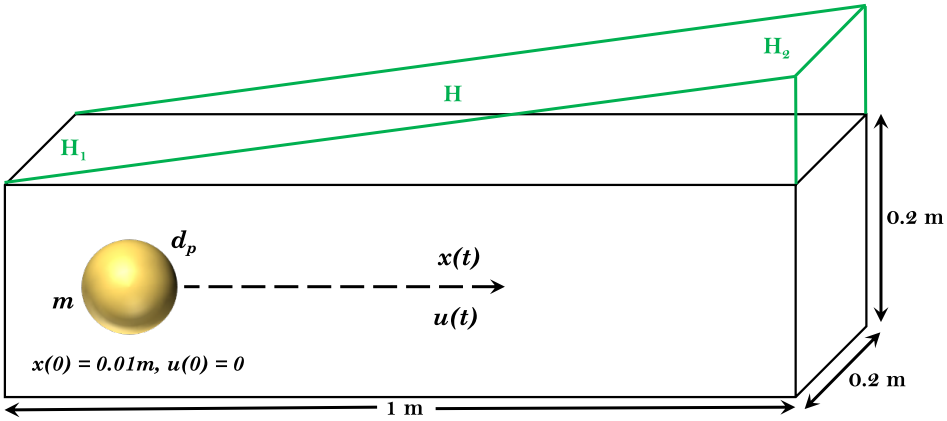

Figure 4.4: Schematic of the domain considered for the DEM study

by adding the corresponding forces in the XDEM solver. As a result of the unique KFD, the particle translates from its initial position with a specific velocity. These time-dependent results from the modified solver are further authenticated against the exact analytical solutions. For the sake of brevity, the analytical formulation for the displacement and velocity of Calorivac is derived only for the 1D linear **H** (as shown in Subsection 4.2.1). However, the same procedure can be implemented to obtain the exact expressions for the remaining **H** arrangements.

4.2.1 Analytical Expression for the Motion of a Particle in a 1D Linear H

The uni-dimensional motion of an individual magnetic particle under the influence of an external **H** is governed by the equation shown below

$$m\frac{d^2x}{dt^2} = \{\mu_0 \left(\mathbf{M}\cdot\nabla\right)\mathbf{H}\}\, V_p \tag{4.1}$$

Here, for simplification, the magnetization is assumed to be a linear function of an external magnetic field such that $\mathbf{M} = \chi\,\mathbf{H}$. To further generalize our analysis, only

1D linearly increasing distribution is considered in x direction i.e. $H = (\Re \times x)\hat{\imath}$ where $\Re$ refers to the constant of proportionality. After implementing the aforementioned substitutions, the Equation 4.1 can be rewritten as

$$\mu_0 \left(\mathbf{M} \cdot \nabla\right) \mathbf{H} = \mu_0 M_x H_{xx} \hat{\imath} = \mu_0 (\chi H_x) \Re \ \rightarrow \mu_0 \chi \Re^2 x \tag{4.2}$$

Moreover, Equation 4.2 can be reformulated as

$$\frac{d^2x}{dt^2} = \frac{\mu_0 \chi \Re^2 x}{m} \rightarrow \frac{d^2x}{dt^2} - \left(\frac{\mu_0 \chi \Re^2 V_p}{m}\right) x = 0 \tag{4.3}$$

The aforementioned equation is a second-order linear homogeneous ordinary differential equation whose solution can be used to obtain the time-dependent displacement $x(t)$ and velocity $u(t)$ of Calorivac particle as shown below:

$$\begin{aligned} x(t) &= \mathrm{C1}\ e^{\lambda_1 t} \ + \ \mathrm{C2}\ e^{\lambda_2 t} \\ u(t) = x'(t) &= \mathrm{C1}\ \lambda_1\ e^{\lambda_1 t} \ + \ \mathrm{C2}\ \lambda_2\ e^{\lambda_2 t} \end{aligned} \tag{4.4}$$

In Equation 4.4, λ_1 and λ_2 are two distinct roots of the differential equation obtained after solving the determinant of the characteristic equation (CE). Additionally, C1 and C2 are the constants that can be obtained after implementing either the initial or the boundary conditions depending on the nature of the problem statement. For a standard 2nd-order linear ODE, its distinct roots can be written as

$$a\ \frac{d^2x}{dt^2} + b\ \frac{dx}{dt} + cx = 0 \quad \text{where} \quad \lambda_{1,2} = \frac{-b \pm \sqrt{b^2 - 4ac}}{2a} \tag{4.5}$$

After comparing, the constants of CE and eventually the roots of the Equation 4.4 can be finalised as

$$a = 1, b = 0, c = -\left(\frac{\mu_0 \chi \Re^2 V_p}{m}\right),\ \lambda_{1,2} = \frac{\pm\sqrt{4c}}{2} \text{ hence } \lambda_{1,2} = \pm\sqrt{\frac{\mu_0 \chi \Re^2 V_p}{m}} \tag{4.6}$$

Further, C1 and C2 (in the Equation 4.4) can be obtained after implementing the following initial conditions for displacement ($x(0) = X_0$) and velocity ($x'(0) = u(0) = U_0$) as shown below:

$$\mathrm{C1} + \mathrm{C2} = X_0 \quad \text{and} \quad \mathrm{C1}\ \lambda_1 + \mathrm{C2}\ \lambda_2 = U_0 \tag{4.7}$$

As initially, the particle is at rest, hence $U_0 = 0$. Also, from Equation 4.6, it is clear that $\lambda_1 = -\lambda_2$. Using these reductions the magnitude of constants can be simplified as

$$\mathrm{C1} = \mathrm{C2} = 0.5X_0 \tag{4.8}$$

Finally, after implementing the corresponding substitutions for C1 and C2 (from Equation 4.8) and $\lambda_{1,2}$ (from Equation 4.6), the displacement and velocity of Calorivac particle over time can be obtained as

$$\boxed{\begin{aligned} x(t) &= 0.5X_0 \left(e^{\sqrt{\frac{\mu_0 \chi \Re^2 V_p}{m}}t} + e^{-\sqrt{\frac{\mu_0 \chi \Re^2 V_p}{m}}t} \right) \\ u(t) = x'(t) &= 0.5X_0 \sqrt{\frac{\mu_0 \chi \Re^2 V_p}{m}} \left(e^{\sqrt{\frac{\mu_0 \chi \Re^2 V_p}{m}}t} - e^{-\sqrt{\frac{\mu_0 \chi \Re^2 V_p}{m}}t} \right) \end{aligned}} \tag{4.9}$$

4.2.2 Dynamics of the Calorivac Particle in Different H Distributions

To replicate and validate the unique motion of Calorivac particle, three generic **H** distributions are considered in the present work as shown in Sub-subsection 4.2.2.1 - 4.2.2.3.

4.2.2.1 For 1D Linear Magnetic Field ($\boldsymbol{H} = \Re x\, \hat{i}$)

Additionally, both time-varying velocity and displacement are compared against the exact analytical expressions for each arrangement as shown in Figure 4.5 - Figure 4.7.

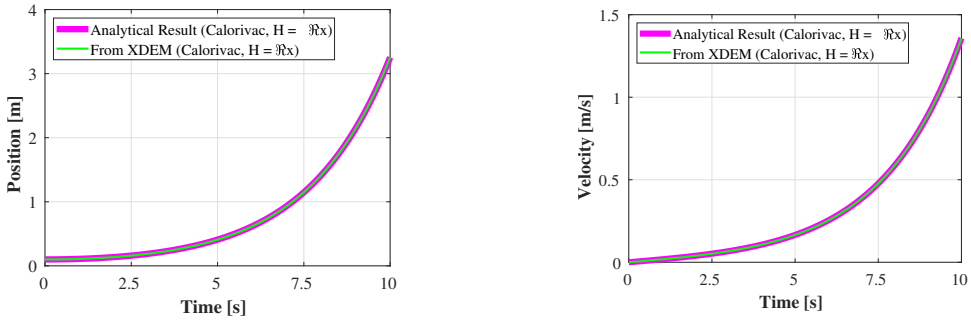

(a) (b)

Figure 4.5: Comparison of analytical results with the XDEM-based solver for $d_p = 100\mu\text{m}$, $\rho = 7200$ kg/m^3, $\chi = 999$ and $\Re = 1000$ (a) Displacement with time, (b) Velocity with time

4

4.2.2.2 For a Generalised 1D Cubic Polynomial Magnetic Field ($\boldsymbol{H} = \left[\Re_1 x^3 + \Re_2 x^2 + \Re_3 x + \Re_4\right]\ \hat{i}$)

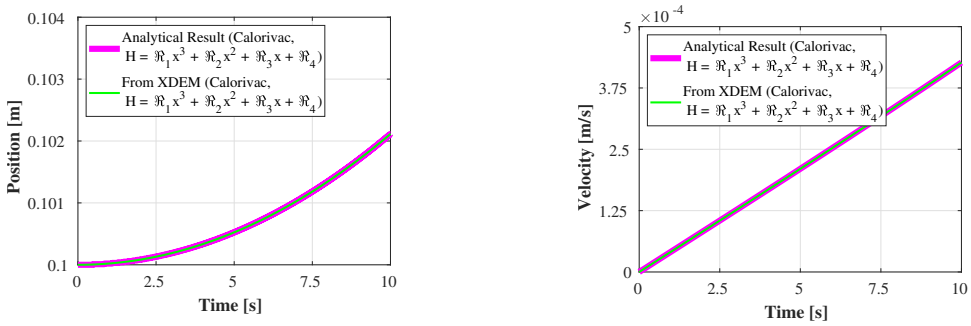

(a) (b)

Figure 4.6: Comparison of analytical results with the XDEM-based solver for $d_p = 100\mu\text{m}$, $\rho = 7200$ kg/m^3, $\chi = 999$ and $\Re_1 = 1000, \Re_2 = 100, \Re_3 = 10, \Re_4 = 1$ (a) Displacement with time, (b) Velocity with time

4.2.2.3 For a Generalised 3D Cubic Polynomial Magnetic Field

$$\boldsymbol{H} = \left[\Re_{1x} x^3 + \Re_{2x} x^2 + \Re_{3x} x + \Re_{4x}\right]\ \hat{i}\ +$$
$$\left[\Re_{1y} y^3 + \Re_{2y} y^2 + \Re_{3y} y + \Re_{4y}\right]\ \hat{j}\ +$$
$$\left[\Re_{1z} z^3 + \Re_{2z} z^2 + \Re_{3z} z + \Re_{4z}\right]\ \hat{k})$$

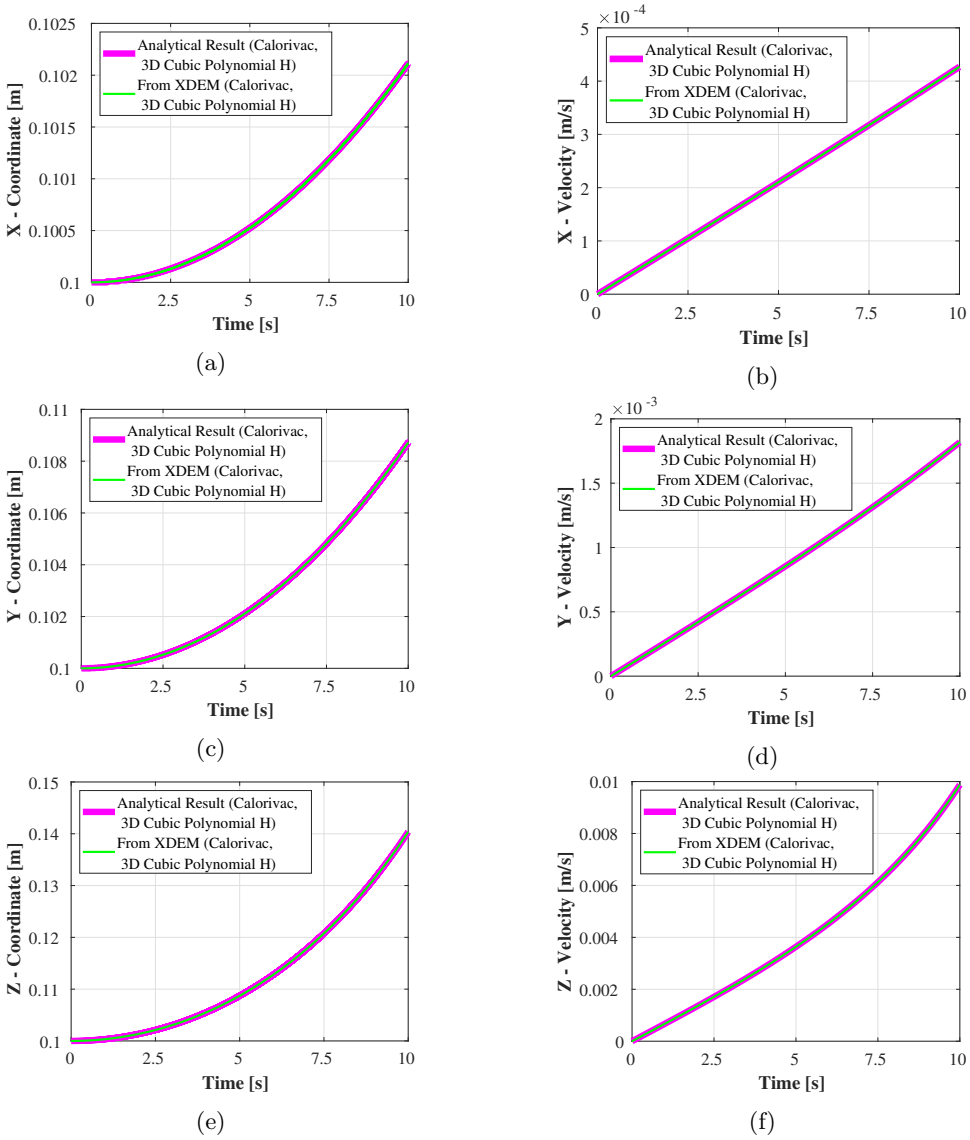

Figure 4.7: Comparison of analytical results with the XDEM-based solver for $d_p = 100\mu\text{m}$, $\rho = 7200\ \text{kg/m}^3$, $\chi = 999$ and $\Re_{1x} = 1000, \Re_{2x} = 100, \Re_{3x} = 10, \Re_{4x} = 1, \Re_{1y} = 2000, \Re_{2y} = 200, \Re_{3y} = 20, \Re_{4y} = 2, \Re_{4z} = 4000, \Re_{2z} = 400, \Re_{3z} = 40, \Re_{4z} = 4$ (a) x with time, (b) U_x with time, (c) y with time, (d) U_y with time, (e) z with time, (f) U_z with time

This DEM study helped us to understand the exact response of an individual Calorivac particle in a surrounding magnetic field. As it is evidently observed from the aforementioned figures, the distinct distribution of **H** results in a dynamic particle motion in each individual direction. Such unique time-dependent displacement and velocity of the same particle is attributed to the corresponding magnitudes of KFD experienced by the Calorivac particle.

4.3 Euler-Euler Mixture Model

At smaller ϕ_d, the entire behaviour of the solid-liquid mixtures can be approximated by a Single Phase numerical Model (SPM) with suitable thermophysical properties [143]. However, as we approach the higher ϕ and larger d_p systems, the aforementioned SPMs provide inaccurate results, and the approximation of considering solid-liquid mixture as a single medium does not hold true. This is mainly because single-phase approximations only take into account the effect of the continuous phase (liquid for the present case) on the dispersed phase (solid for the present case). Nevertheless, it is a well established observation that at higher ϕ_d, the dispersed phase equivalently influences the continuous phase by reducing the mean momentum of the flow. For resolving this concern, there exist different multiphase modelling approaches based on the length scale of interest, computational cost, and range of validity. To address this issue in a higher ϕ_d dispersed flow systems (particle diameter $<<$ length scale of flow), an Euler - Euler (EE) based multiphase model must be used for accurate analysis of the complex solid-liquid interactions [141]. More specifically, at intermediate particle loading ($\alpha_d\rho_d/\alpha_c\rho_c$) and for smaller Stokes number St, only two EE modelling strategies are viable [144] i.e. a complete two-fluid model and a mixture model. In a complete two-fluid model, the conservative governing equations are solved for each phase, and the coupling is obtained via interphase exchange coefficients. On the other hand, only a single set of equations is considered for the mixture model along with additional constitutive relations for closure. Hence, for the same validation

range and length scale of interest, a mixture model approach is used for the present work which is computationally more efficient than its counterpart EE version [145].

The aforementioned mixture model approach has been implemented across broad fields of solid-liquid systems such as sand water mixture [146], heavy oil flow [147], heterogeneous ice slurry [148], fly ash water [149, 150], and wax transport [151]. On similar lines, numerous research works have implemented a mixture model to study the flow and thermal characteristics of the MF. An outline of such major studies along with their model specifications and the principle conclusion is shown in Table 4.1. Overall, it is clearly noticed that the magnitude and distribution of the external magnetic field can be used as an effective means to monitor and manipulate the heat transfer rate. This is mainly attributed to the presence of **H** which creates several local recirculation zones that eventually modify its thermal behaviour.

Additionally, other significant works have also been carried out to understand the solid-liquid behaviour of MF. One of the foremost works that discusses the two-phase aspects of magnetic fluids is conducted by Rosensweig et al. [152]. Authors used the interpenetrating continuum approximation to examine the void fraction distribution and stability of magnetized fluidised beds. On similar lines, Sergeev and Muromsky [153] studied the propagation of linear disturbances in a liquid-solid fluidised bed and derived magnetic stabilization criteria. An experimental study is carried out by Rozenblit et al. [154] to investigate the local and average heat transfer in a turbulent solid liquid slurry flow using infrared imaging and an electro resistance sensor. It is reported that the cross-sectional variation of particle concentrations has a significant influence on the h_{local}, and higher particle concentration result in proportional increment of the h_{avg}. For understanding the capillary flow of a two-phase ferromagnetic suspension, Kuzhir et al. [155] implemented an in-vitro model and discussed the flow onset/flow blockage behaviour using pressure velocity dependence. Recebli and Kurt [156] performed an analytical study for a two-phase circular Poiseuille flow and attributed decreased local U of both phases to the perpendicular **H**. A solid-liquid mixed convection under the influence of different

Table 4.1: Overview of recent numerical studies that investigate magnetic fluids using two-phase mixture model

Ref	Physical Domain	Type of $\mathbf{H}$	$\mathbf{M}$	μ	k	Key findings
Tynjälä et al. [162]	Cylindrical thin layer	Not mentioned (NM)	NM	NM	NM	Towards the beginning of convection, ferrofluid exhibits spatio - temporal chaos whose wave number is different from turbulent flows.
Jafari et al. [163]	3D cylinder	$\mathbf{H}^{\mathrm{I}}$	$\mathbf{M}^{\mathrm{II}}$	μ^{III}	k^{IV}	Perpendicular orientation of magnetic field and temperature gradient results in improved heat transfer.
Aminfar et al. [164]	3D cylinder	$\mathbf{H}^{\mathrm{V}}$	$\mathbf{M}^{\mathrm{VI}}$	μ^{III}	k^{IV}	Negative field gradient have similar effects to that of buoyancy and improve Nu at the cost of higher pumping power.

Continued on next page

Table 4.1 – *Continued from previous page*

Ref	Physical Domain	Type of **H**	**M**	μ	k	Key findings
Aminfar et al. [165]	3D duct	$\mathbf{H}^{\mathrm{V}}$	$\mathbf{M}^{\mathrm{VI}}$	μ^{III}	k^{VII}	Transverse magnetic field distorts the axial velocity profile and result in the formation of a counter rotating vortices pair.
Ghasemian et al. [166]	2D Channel	$\mathbf{H}^{\mathrm{VIII}}$	$\mathbf{M}^{\mathrm{IX}}$	μ^{II}	k^{IV}	Improved flow mixing and heat transfer is observed at an optimum frequency of alternating magnetic field which increases with an increase in *Re*.
Hangi et al. [167]	3D cylinder	$\mathbf{H}^{\mathrm{V}}$	$\mathbf{M}^{\mathrm{X}}$	μ^{II}	k^{II}	Increasing *Re* at a specific **H** results in reduced flow mixing whereas enhanced recirculation is observed at higher **H** for any particular *Re*.

Continued on next page

Table 4.1 – *Continued from previous page*

Ref	Physical Domain	Type of **H**	**M**	μ	k	Key findings
Hekmat et al. [168]	3D annulus	$\mathbf{H}^{\text{V}}$	$\mathbf{M}^{\text{VI}}$	μ^{XI}	k^{VII}	The Kelvin force density increases proportionally with the gradient of applied field and ϕ of suspended magnetic nanoparticles.
Yousefi et al. [169]	3D flattened tube	$\mathbf{H}^{\text{V}}$	$\mathbf{M}^{\text{VI}}$	μ^{XI}	k^{VII}	The location as well as the number of the secondary flow rotations varies with respect to the applied field and lead to improved wall shear stress.

[I] Steady and Uniform [II] Constant magnitude [III] Rosensweig's correlation [23] [IV] Volume fraction weighted correlation [V] Steady and Non - Uniform [VI] Langevin function [159] [VII] Hamilton - Crosser model [160] [VIII] Steady/Transient and non - Uniform [IX] Temperature dependent linear magnetization model [57] [X] Combination of VI and IX [XI] Batchelor model [161]

magnetic field gradients is evaluated by Aminfar et al. [157]. Authors proposed that the desired behaviour of Nu, friction factor, and the U profiles can be obtained by manipulating the magnetic field gradients in both axial and transverse direction. In the same context, effect of 2D non - uniform magnetic field on the flow behaviour of blood ferrofluid mixture is studied numerically by Aminfar et al. [158]. It is concluded that the application of positive and negative field gradients along the

streamwise direction leads to the constriction and expansion of the considered elastic tube respectively.

4.3.1 Coupling Strategies and Types of Mixture Models

For any solid - liquid suspension, there exits three different ways to resolve the interplay between the dispersed phase and its surrounding carrier phase as shown in Figure 4.8. As discussed earlier, at very small concentrations (smaller than 0.01% by volume [143]), particles almost have no influence on the continuous phase. Thus, the flow behaviour can be directly modelled without considering the influence of dispersed phase. This type of arrangement is referred to as one way coupling. However, as we move towards the higher ϕ_d, the dispersed particles might alter the motion of fluid elements which can lead to the reduction of the overall momentum. In such case, the two way coupling should be employed which takes into account the influence of suspended particles on the mean momentum of the flow. Moreover, at a comparatively higher ϕ_d the distance between the suspended particles reduces

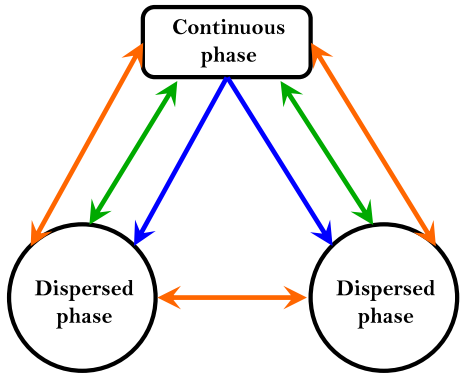

One way coupling–Effect of continuous phase on dispersed phase

Two way coupling–Mutual influence of continuous phase & dispersed phase

Four way coupling–two way coupling with interactions among dispersed phase

Figure 4.8: Overview of different coupling approaches

Table 4.2: Comparison between the DFM and the DMM

Drift Flux Model	Diffusion Mixture Model
❑ Velocity of each phase is measured relative to the mixture centre of volume ($\mathbf{U}_{jk} = \mathbf{U}_k - \mathbf{U}_j$)	❑ Velocity of each phase is computed relative to the mass centre of mixture ($\mathbf{U}_{mk} = \mathbf{U}_k - \mathbf{U}_m$)
❑ Constitutive relation $\sum \phi_k \mathbf{U}_{jk} = 0$	❑ Constitutive relation $\sum \phi_k \rho_k \mathbf{U}_{mk} = 0$
❑ Important in kinematic analysis i.e. systems with constant density, energy, and enthalpy	❑ Preferred for dynamic analysis i.e. systems with varying density, energy, and enthalpy

which leads to enhanced particle - particle interactions. Such interplays can affect the pressure and the viscous stresses of the suspensions and can be termed as four way coupling. For the present considered system, as the inter-particle spacing is considerable large (as shown in Equation C.3), the influence of particle on its surrounding particles is not considered.

Based on the approximations involved, the mixture model approach discussed above can be implemented in mainly three different numerical frameworks. The simplest ASMM (Algebraic Slip Mixture Model) completely neglects the interaction between the phases. This results in reduced accuracy limiting its range of application up to lower ϕ_d. A relatively better formulation implements the volumetric flux (velocity of mixture centre of volume) based method often termed as Drift Flux Model (DFM). However, DFM essentially requires the strict coupling between the dispersed and the continuous phase and hence neglects their associated density difference. Thus, a Diffusion Mixture Model (DMM) is used in the present work that essentially has no limiting approximations analogous to their counterparts [170]. For better insights, an analogy between DFM and DMM is also shown in Table 4.2.

4.4 Formulating the Diffusion Mixture Model

An ideal multiphase flow formulation should capture instantaneous variations of each phase with an identical boundary condition at all the interfaces. However, the presence of moving interface makes it very difficult to formulate the problem in a physical as well as in a mathematical manner. Thus, to convert such microscopic variations to observable macroscopic fields, different averaging procedures are implemented. Nonetheless, all such averaging techniques result in additional terms in the corresponding field equations. This essentially leads to the necessity of different constitutive relations that should be used along with the governing equation for its closure. The Favré averaged (mass weighted average) equations[II] for the conservation of mass for any solid-liquid system can be written as [141, 172]

$$\frac{\partial}{\partial t}\left(\phi_k \rho_k\right) + \nabla \cdot \left(\phi_k \rho_k \mathbf{U}_k\right) = \Gamma_k \tag{4.10}$$

After summation of above equation for all the phases

$$\frac{\partial}{\partial t}\sum_{k=1}^{n}\left(\phi_k \rho_k\right) + \nabla \cdot \sum_{k=1}^{n}\left(\phi_k \rho_k \mathbf{U}_k\right) = \underbrace{\cancelto{0}{\sum_{k=1}^{n}\Gamma_k}}_{\text{as total mass is conserved}} \tag{4.11}$$

Finally, it becomes the continuity equation for the considered mixture and can be written as

$$\boxed{\frac{\partial \rho_m}{\partial t} + \nabla \cdot \left(\rho_m \mathbf{U}_m\right) = 0} \tag{4.12}$$

where the mixture density and mixture velocity are represented as shown below:

$$\boxed{\rho_m = \sum_{k=1}^{n}\phi_k \rho_k \quad \text{and} \quad \mathbf{U}_m = \frac{1}{\rho_m}\sum_{k=1}^{n}\phi_k \rho_k \mathbf{U}_k} \tag{4.13}$$

[II] For the sake of brevity, the present work is only limited to the derivation of DMM using Favré - averaged technique. Interested readers can go through Chapter 3 of Ishii & Hibiki [141], and Section 1.2 of Hiltunen et al. [171] for further description.

On similar lines, the Favré averaged equation for the conservation of linear momentum can be written as [171]

$$\frac{\partial}{\partial t}\left(\phi_k \rho_k \mathbf{U}_k\right) + \nabla \cdot \left(\phi_k \rho_k \mathbf{U}_k \mathbf{U}_k\right) = -\phi_k \nabla p_{\mathrm{k}} + \nabla \cdot \left[\phi_k \left(\boldsymbol{\tau}_k + \boldsymbol{\tau}_{Tk}\right)\right] + \phi_k \rho_k \mathbf{g} + \mathbf{F}_k + \mathbf{M}_k \tag{4.14}$$

Here, $\boldsymbol{\tau}_k$ and $\boldsymbol{\tau}_{Tk}$ refer to the viscous stress and turbulent stress respectively. Additionally, $\mathbf{F}_k$ is the external force density experienced by the mixture and $\mathbf{M}_k$ indicates the surface tension effects. In the present work, the effect of turbulent stress and the interface surface tension is neglected. Hence, Equation 4.14 can be summed up for both phases as

$$\frac{\partial}{\partial t}\sum_{k=1}^{n}\left(\phi_k \rho_k \mathbf{U}_k\right) + \nabla \cdot \sum_{k=1}^{n}\left(\phi_k \rho_k \mathbf{U}_k \mathbf{U}_k\right) = -\sum_{k=1}^{n}\phi_k \nabla p_{\mathrm{k}} + \nabla \cdot \sum_{k=1}^{n}\left(\phi_k \boldsymbol{\tau}_k\right) + \sum_{k=1}^{n}\phi_k \rho_k \mathbf{g} + \sum_{k=1}^{n}\mathbf{F}_k \tag{4.15}$$

To simplify the convective term of the above equation, a diffusion mixture velocity is used that measures the velocity of phase "k" relative to its mass centre of mixture (or mixture velocity) as described below

$$\boxed{\mathbf{U}_{mk} = \mathbf{U}_k - \mathbf{U}_m} \tag{4.16}$$

Using Equation 4.16, the second term of Equation 4.15 can be rewritten as

$$\begin{aligned}\nabla \cdot \sum_{k=1}^{n}\left(\phi_k \rho_k \mathbf{U}_k \mathbf{U}_k\right) &= \phi_d \rho_d \mathbf{U}_d \mathbf{U}_d + \phi_c \rho_c \mathbf{U}_c \mathbf{U}_c \\ &= \phi_d \rho_d \left(\mathbf{U}_{md} + \mathbf{U}_m\right)^2 + \phi_c \rho_c \left(\mathbf{U}_{cd} + \mathbf{U}_m\right)^2\end{aligned} \tag{4.17}$$

Further, with the help of the constitutive relation of diffusion velocity ($\sum \phi_k \rho_k \mathbf{U}_{mk} = 0$) and ρ_m, the convective part is described as

$$\nabla \cdot \sum_{k=1}^{n}\left(\phi_k \rho_k \mathbf{U}_k \mathbf{U}_k\right) = \nabla \cdot \left(\rho_m \mathbf{U}_m \mathbf{U}_m\right) + \nabla \cdot \sum_{k=1}^{n}\phi_k \rho_k \mathbf{U}_{mk} \mathbf{U}_{mk} \tag{4.18}$$

Finally, after replacing the Equation 4.18 with minor rearrangements the conservation of linear momentum can be formulated as

$$\boxed{\begin{aligned}\frac{\partial \rho_m \mathbf{U}_m}{\partial t} + \nabla \cdot (\rho_m \mathbf{U}_m \mathbf{U}_m) = -\nabla p_m + \nabla \cdot \boldsymbol{\tau}_m + \nabla \cdot \boldsymbol{\tau}_{Dm} \\ + \rho_m \mathbf{g} + \mu_o (\mathbf{M} \cdot \nabla) \mathbf{H}\end{aligned}} \tag{4.19}$$

where all the corresponding substitutions are further described below

$$\begin{aligned}&\text{Viscous stress} \rightarrow \boldsymbol{\tau}_m = \sum_{k=1}^{n} (\phi_k \boldsymbol{\tau}_k) = \mu_m \sum_{k=1}^{n} \left[\nabla \mathbf{U}_k + (\nabla \mathbf{U}_k)^{\mathrm{T}} - \nabla \cdot \frac{2}{3} \mathbf{I} \mathbf{U}_k \right] \\ &\text{Diffusion stress} \rightarrow \boldsymbol{\tau}_{Dm} = -\sum_{k=1}^{n} (\phi_k \rho_k \mathbf{U}_{mk} \mathbf{U}_{mk}) \\ &\text{Mixture pressure gradient} \rightarrow \nabla p_m = \sum_{k=1}^{n} \phi_k \nabla p_{\mathrm{k}}\end{aligned} \tag{4.20}$$

In Equation 4.19, the diffusion stress refers to the momentum transfer due to relative motion between dispersed phase and the carrier phase[III]. Additionally, the last term refers to the KFD experienced by the mixture due to the presence of non-uniform magnetic field distribution as described in Section 1.3.

As mentioned earlier, in the DMM formulation only a single momentum equation is solved for both the phases. Thus, to complement the existing set of governing equation, a supplementary continuity equation for the dispersed phase is required as shown below:

$$\frac{\partial}{\partial t} (\phi_d) + \nabla \cdot (\phi_d \mathbf{U}_m) = -\nabla \cdot (\phi_d \mathbf{U}_{md}) \tag{4.21}$$

The above formulation involves the diffusion velocity that eventually enables to resolve the velocity of both $\mathbf{U}_d$ and $\mathbf{U}_c$. To do so, $\mathbf{U}_{md}$ is represented in terms of a slip velocity ($\mathbf{U}_{sl}$) that governs the relative difference between the dispersed phase and the carrier phase as shown below:

$$\mathbf{U}_{md} = \frac{\phi_c \rho_c \mathbf{U}_{sl}}{\rho_m} \quad \text{and} \quad \mathbf{U}_{mc} = -\frac{\phi_d \rho_d \mathbf{U}_{sl}}{\rho_m} \tag{4.22}$$

[III] Influence of $\boldsymbol{\tau}_{Dm}$ is completely ignored in the ASMM, whereas with DFM a $\mathbf{U}_{jk}$ based formulation is used to calculate diffusion stress.

To accurately compute $\mathbf{U}_{sl}$, influence of all forces must be considered that results in relative motion between the suspended particles and its surrounding fluid. For a conventional solid-liquid system, there exist different correlations that takes into account several factors to compute $\mathbf{U}_{sl}$ such as drag force, Basset force, virtual mass force etc. However, in the present context as the dispersed particles are magnetic in nature and are present within a $\mathbf{H}$ distribution, an appropriate correlation [173] is used to compute the relative slip between the Calorivac particles and surrounding Galinstan as shown below[IV]

$$\sum F_p = 0 \quad \text{thus} \quad \frac{(\rho_d - \rho_c)\,\pi\, d_p^3}{6}\left(\mathbf{g} - \frac{\partial \mathbf{U}_m}{\partial t}\right) - 3\,\pi\,\mu_c\, d_p\, \mathbf{U}_{sl} + \mu_o\, m_p\, L(\xi)\,\nabla \mathbf{H} = 0 \tag{4.23}$$

$$\boxed{\mathbf{U}_{sl} = \mathbf{U}_d - \mathbf{U}_c = \frac{(\rho_d - \rho_c)\, d_p^2}{18\,\mu_c}\left(\mathbf{g} - \frac{\partial \mathbf{U}_m}{\partial t}\right) + \frac{\mu_o\, m_p\, L(\xi)\,\nabla \mathbf{H}}{3\,\pi\,\mu_c\, d_p}} \tag{4.24}$$

To govern the non-uniform temperature distribution within our incompressible magnetic system, the generalised Energy equation can be written as [174]

$$\underbrace{\frac{De}{Dt}}_{\substack{\text{Total rate of}\\ \text{change in}\\ \text{internal energy}\\ \text{per unit volume}}} = \underbrace{-\nabla\cdot\dot{Q}}_{\substack{\text{Rate of internal}\\ \text{energy change}\\ \text{per unit}\\ \text{volume via}\\ \text{conduction}}} + \underbrace{(\tau : \nabla\mathbf{U})}_{\substack{\text{Rate of change}\\ \text{in internal}\\ \text{energy per unit}\\ \text{volume by}\\ \text{viscous dissipation}}} + \underbrace{\cancelto{0}{-p\nabla\cdot\mathbf{U}}}_{\substack{\text{Rate of internal}\\ \text{energy change}\\ \text{per unit}\\ \text{volume via}\\ \text{compression}}} + \underbrace{\dot{Q}_{\text{MCE}}}_{\substack{\text{Rate of internal}\\ \text{energy change per}\\ \text{unit volume}\\ \text{via magnetic work}}} \tag{4.25}$$

In the above equation, $\dot{Q}_{\text{MCE}}$ represents the temperature rise/drop within the Calorivac-Galinstan mixture due to the MCE. On substituting e in terms of enthalpy where h is further simplified using T, the overall governing equation for thermal transport can be rewritten as shown below: [15]

$$(\rho C_p)_m \left[\frac{\partial T}{\partial t} + (\mathbf{U}_m\cdot\nabla)\,T\right] = -\nabla\cdot(k_m\nabla T) + (\tau : \nabla\mathbf{U}_m) + \dot{Q}_{\text{MCE}} \tag{4.26}$$

[IV] For the present system, the effect of the Basset force and the virtual mass force is neglected as the γ (ρ_d/ρ_c) is larger than 1 [171].

The above equation can be further simplified by replacing $\dot{Q}_{\mathrm{MCE}}$ from Equation A.9

$$(\rho C_p)_m \left[\frac{\partial T}{\partial t} + (\mathbf{U}_m \cdot \nabla) T\right] = -\nabla \cdot (k_m \nabla T) + (\tau : \nabla \mathbf{U}_m) - \mu_o T \left(\frac{\partial M}{\partial T}\right)_H \left(\underbrace{\cancelto{0}{\frac{\partial \mathbf{H}}{\partial t}}}_{\text{For permanent magents}} + (\mathbf{U}_m \cdot \nabla) \mathbf{H} \right) \tag{4.27}$$

$$\boxed{(\rho C_p)_m \left[\frac{\partial T}{\partial t} + (\mathbf{U}_m \cdot \nabla) T\right] = -\nabla \cdot (k_m \nabla T) + (\tau : \nabla \mathbf{U}_m) - \mu_o T \left(\frac{\partial M}{\partial T}\right)_H ((\mathbf{U}_m \cdot \nabla) \mathbf{H})} \tag{4.28}$$

As mentioned earlier, to have a closure on the number of independent variables, various constitutive relations are used along with the available governing equations as described below

$$\begin{aligned} \text{Saturation condition} &\rightarrow \sum_{k=1}^{n} \phi_k = 1 \\ \text{Interfacial mass conservation} &\rightarrow \sum_{k=1}^{n} \Gamma_k = 0 \\ \text{Kinematic closure condition} &\rightarrow \sum_{k=1}^{n} \phi_k \rho_k \mathbf{U}_{mk} = 0 \end{aligned} \tag{4.29}$$

CHAPTER 5

Realising Magnetically Driven Energy Transport

For achieving magnetically driven momentum/energy transport, it is first necessary to comprehend the complex interaction of magnetic fields and magnetic fluids. To do so, the computationally least expensive approach (refer Figure 4.3) is used in the initial stages. For that purpose, two different case studies have been performed using single phase analysis. This is done to evaluate changes in hydro-thermal characteristics as a response to an externally applied magnetic field. In Section 5.2, influence of a magnetic dipole is studied on a ferrofluid enclosed in semicircular annulus. Later, the effect of permanent magnet on a Gadolinium mixture within a circular annulus is discussed in Section 5.3. All sections of the current chapter are adapted from two different published manuscripts Dalvi et al. [175,176]. The main purpose of this work

is to obtain preliminary data for magnetically driven momentum/energy transport devices. This can be further used to find a feasible design that can ensure continuous flow and self-sustained heat transfer solely because of magnetic forces.

5.1 Overview of Existing Works

For the past few years, a lot of work is done to use these magnetically induced body forces for operating automated energy transport devices. Several researchers performed numerous experimental and numerical studies to investigate different possible configurations. Fumoto et al. [177] performed various experiments on an oval loop of 2 mm inner diameter for small scale heat transport, using TMC principles. It is stated that, by changing position and strength of the magnet, flow velocity of TSMF can be controlled. Lian et al. [178] developed a method, which uses TMC and illustrated that it can be used for automatic energy transfer. Authors compared experimental data with numerical results and studied the effect of different heat loads, temperature and magnetic field distributions. Xuan and Lian [179] extended this work and came up with an improved experimental design which can be used for cooling of electronic equipments using thermo-magnetic effect of ferrofluid. Authors concluded that a higher heat dissipation rate can be achieved with increasing heat load as it leads to greater TMC. Lian et al. [180] experimentally examined a small automatic energy transport device with micro-scale PIV technique. It is shown that an internal thermal gradient and an external magnetic field can be used to regulate energy transport in such devices. Among all three configurations studied by them, a circular configuration with two magnets is found to be optimal. Iwamoto et al. [181] used binary TSMF to operate a heat transport device which is solely driven by magnetic body force. With the help of experimental and theoretical formulations, it is put forward that buoyancy of gas phase helps in increasing magnetic body force at low magnetic fields. Yamaguchi and Iwamoto [182] further redesigned the device for its performance under various magnetic field orientations. It is experimentally

demonstrated that, the device is able to transfer thermal energy over a distance of 5 m. A toroidal loop is numerically investigated for its heat transfer and flow characteristics in the presence of magnetic field by Bahiraei and Hangi [183]. Different parameters including the amount of heat flux in the heat source, temperature of the heat sink, magnet position and its magnetic strength are studied.

5.2 Interaction of Ferrofluid with Magnetic Dipole[I]

A numerical study is performed to examine the influence of a non-uniform magnetic field on the thermo-hydraulic behaviour of a ferrofluid. The analysis is done in the context of a differentially heated semi-circular annulus where a magnetic dipole with its distinct location and dipole strength is used to obtain different configurations. The field variables are computed by solving the coupled set of flow equations, energy equations and the Maxwell's magneto-statics equations. A detailed description is provided on the flow and thermal response after observing different parameters at both global and local scale. Comparison of streamlines and isotherms with a reference case of natural convection concludes that the recirculation zones are responsible for the increased velocity and heat transfer magnitudes. Another key finding is about the possibility to locally improve the thermal performance of heat exchangers at any desired position along the circumference. To keep the present chapter concise, details of grid independence study, model validation, and numerical methods are not mentioned here and can be obtained from Dalvi et al. [175].

5.2.1 Problem Description and Numerical Methodology

The geometrical details of the present problem statement along with grid distribution is shown in Figure 2.3 and Figure 2.4 respectively. In this work, all three magnetic

[I]The following work is an excerpt from the published article by Dalvi et al. [175]

field variables ($\mathbf{B}$, $\mathbf{H}$, and $\mathbf{M}$) are considered with the help of Maxwell's equations of magneto-statics as shown in Equation 5.1.

Maxwell's Equations

$$\nabla \cdot \mathbf{B} = 0, \quad \nabla \times \mathbf{H} = 0, \quad \text{and} \quad \mathbf{B} = \mu_o \left(\mathbf{H} + \mathbf{M}\right) \tag{5.1}$$

Here, $\mathbf{B}$ refers to the magnetic flux density, $\mathbf{H}$ is the magnetic field, and both are coupled via magnetic permeability ($\mu_0 = 4\pi \times 10^{-7}$ kg.m/s^2.A^2) and magnetization ($\mathbf{M}$). To approximate this magnetization of the ferrofluid mixture, a superparamagnetic law [23] is implemented that takes into account the effect of varying T, H and ϕ as shown below in Equation 5.2:

$$\mathbf{M} = M_d\, \phi \left[\coth(\alpha) - \frac{1}{\alpha}\right] \quad \text{where } \alpha = \frac{\mu_0 m H}{K_B T} \tag{5.2}$$

In the above equation, M_d (446 kA/m) represents the bulk magnetization of solid Fe_3O_4 particles and K_B (1.3×10^{-23} kg.m/s^2.K) is the Boltzmann constant. In addition to the magnetic field variables, flow field variables (p, $\mathbf{U}$, and T) for an incompressible, non - isothermal, and electrically non - conducting ferrofluid are determined with the help of Equation 5.3 - Equation 5.5 as displayed below

Continuity Equation

$$\nabla \cdot \mathbf{U} = 0 \tag{5.3}$$

Momentum Equation

$$\rho_{nf} \left[\frac{\partial \mathbf{U}}{\partial t} + \left(\mathbf{U} \cdot \nabla\right) \mathbf{U}\right] = -\nabla p + \mu_{nf} \nabla^2 \mathbf{U} + \mu_0 \left(\mathbf{M} \cdot \nabla\right) \mathbf{H} + g(\rho_{nf} - \rho_\infty) \tag{5.4}$$

Energy Equation

$$(\rho C_p)_{nf} \left[\frac{\partial T}{\partial t} + \left(\mathbf{U} \cdot \nabla\right) T\right] = k_{nf} \nabla^2 T \tag{5.5}$$

In Equation 5.3 - Equation 5.5, $\mathbf{U}$, t, p, and T represent velocity, time, pressure, and temperature of the entire mixture, respectively. In Equation 5.4, $\mu_0 \left(\mathbf{M} \cdot \nabla\right) \mathbf{H}$ represents a volumetric body force experienced by the Fe_3O_4 mixture due to the

presence of a non-uniform magnetic field. This term is often referred as the Kelvin Force Density (KFD) which results in the motion of the working fluid towards the region of higher magnetic field. Additionally, $g(\rho_{nf} - \rho_{\infty})$ refers to the Boussinesq approximation that takes into account the movement of ferrofluid solely due to the density difference.

The afore-stated group of governing equations is closed by using the boundary conditions for the respective field variables (as defined in Table 5.1) along with the dimensionless parameters mentioned below

$$Ra = \frac{g\beta(T_H - T_C)L_c^3}{\nu_{nf}\alpha_{nf}} \quad \text{and} \quad Mn = \frac{\mu_0 \widetilde{H}^2 L_c^2}{\rho_{nf}\alpha_{nf}^2} \quad \text{where} \quad \widetilde{H} = \frac{\gamma}{2\pi b} \tag{5.6}$$

Table 5.1: Information about boundary conditions

	Inner Wall	Outer Wall	Left walls
p	$\partial p/\partial n = 0$	$\partial p/\partial n = 0$	$\partial p/\partial n = 0$
U	$u, v = 0$	$u, v = 0$	$\partial U/\partial n = 0$
T	T_H	T_C	$\partial T/\partial n = 0$
M	$Mx, My = 0$	$\partial M/\partial n = 0$	$\partial M/\partial n = 0$
H	$\partial H/\partial n = 0$	$Hx, Hy = 0$	$Hx, Hy = 0$

5.2.2 Results and Discussions

To understand the influence of varying locations and magnetic dipole strengths on the TMC, all 9 arrangements are analysed for their hydro-thermal behaviour at global as well as at local scales.

Globally, the magnitude of U_{Mean} and Nu_{avg} is compared among all the configurations as shown in Figure 5.1 and Figure 5.2, respectively. The U_{Mean} is computed for the complete domain, whereas the Nu_{avg} is defined only for the inner hot wall. It can be observed from both aforementioned figures, the magnitude of Nu_{avg} as well as the U_{Mean} increases with the increment in Mn at all dipole locations. However,

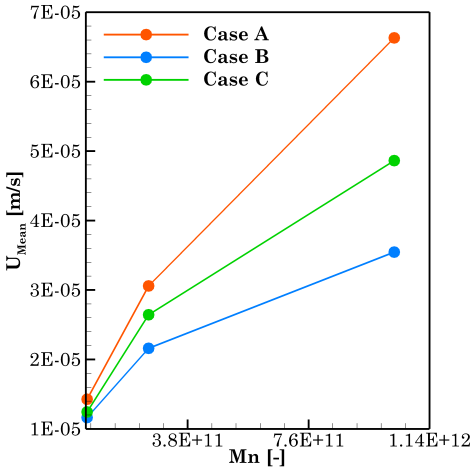

Figure 5.1: Variation of U_{Mean} at $Ra = 10^6$ for different positions of wire and Mn

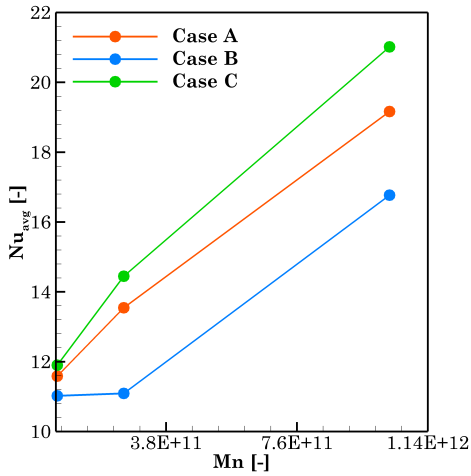

Figure 5.2: Variation of Nu_{avg} at $Ra = 10^6$ for different positions of wire and Mn

at all three Mn, the maximum U_{Mean} is obtained for case A, whereas case C has the largest Nu_{avg}. To understand the reasoning for this complex global behaviour, it is essential to observe the flow characteristics at regional scales. Thus, further local insights are obtained by comparing the U_{Mean} contours and streamline distribution along with a reference case of $Mn = 0$ at $Ra = 10^6$.

The effect of the different dipole locations at the highest Mn is shown in Figure 5.3. In the absence of a magnetic dipole, the streamlines exhibit a typical buoyancy driven flow characteristics. The fluid adjacent to the inner wall retains higher temperature (T_H) relative to its surrounding fluid. Such comparably less denser fluid moves in the upward direction creating a clockwise (CW) plume within the ferrofluid domain as shown in Sub-figure 5.3a. However, existence of a non-uniform magnetic field from the magnetic dipole results in the presence of KFD (as discussed in Section 5.2.1). Such unbalanced body forces disturb the afore-stated typical arrangement and lead to the formation of local vortices. This phenomenon can be clearly noticed from the Sub-figure 5.3b - Sub-figure 5.3d where recirculation zones are present within the entire domain at all three dipole locations. Most notably, a large CW recirculation is

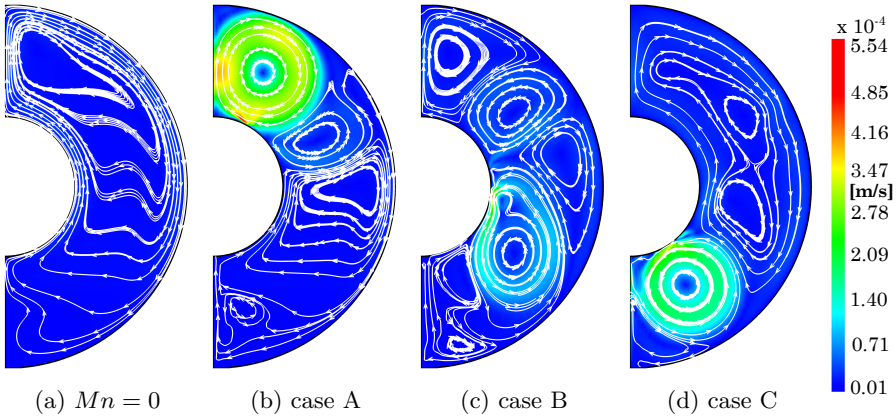

(a) $Mn = 0$ (b) case A (c) case B (d) case C

Figure 5.3: Comparison of streamline distribution and U_{Mean} contours at $Mn = 1.029 \times 10^{12}$ (With the reference case of $Mn = 0$)

observed at the top for case A and an anti-clockwise (ACW) recirculation is noticed at the bottom of semi-circular annulus for case C.

The strength of both aforementioned vortices is relatively larger than case B and can be clearly confirmed from the magnitudes of U_{Mean} contour. Such strong recirculation zones also improve the overall heat transfer by enhancing the ferrofluid mixing which subsequently increases Nu_{avg} as compared to case B for all Mn. At location B however, alternate CW and ACW vortices at the local scale nullify each others contribution which result in the lower global values for both U_{Mean} and Nu_{avg} as shown in Figure 5.1 and Figure 5.2, respectively. Further, the combined outcome of CW vertical plume from the buoyancy force and a CW recirculation at the top results in the highest U_{Mean} magnitudes for case A at all Mn. On the other hand, the presence of relatively longer recirculation zone along with the larger U_{Mean} magnitude is responsible for the maximum Nu_{avg} observed at location C.

On the similar lines, the influence of Mn on the flow distribution of TMC is compared for the case B as shown in Figure 5.4. The presence of magnetic dipole at $\theta = 0°$ lead to the major flow disturbances near the central region at all Mn. It is to be noted that the number of recirculation zones increases with the increase in Mn, as

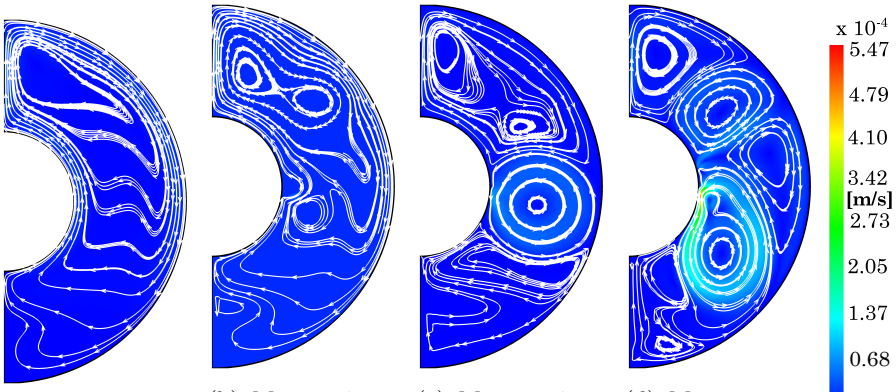

(a) $Mn = 0$ (b) $Mn = 6.433 \times 10^{10}$ (c) $Mn = 2.573 \times 10^{11}$ (d) $Mn = 1.029 \times 10^{12}$

Figure 5.4: Streamline distribution and U_{Mean} contours for case B

shown in Sub-figure 5.4b - Sub-figure 5.4d. This significant observation is attributed mainly to the presence of KFD that elongates the distinct CW vertical plume of the buoyancy driven flow. This stretching of the recirculation zone results in the formation of a smaller pair of CW vortices (refer Sub-figure 5.4b). With the further increase in Mn, such smaller vortices eventually separate and develop in their size. This local observation justifies the increased global values of U_{Mean} and Nu_{avg} with respect to Mn at all dipole locations as demonstrated in Figure 5.1 and Figure 5.2.

To further complement our understanding about the hydrodynamic interactions of TMC, isotherms and Nu_{local} distributions are also observed for all configurations. As shown in Figure 5.5, influence of the strength and the location of the magnetic dipole is compared for all cases along with a reference case of $Mn = 0$ at $Ra = 10^6$. For the aforementioned reference case, a typical thermal plume is obtained at the top of annulus as shown in Sub-figure 5.5a. Also, the Nu_{local} distribution for the same follows an approximate decreasing linear trend with maxima at the bottom of the inner hot wall (at $\theta = -90°$) (Figure 5.6 and Figure 5.7). Such peculiar distribution of local Nu and isotherm can also be confirmed from the seminal works of Kuehn and Goldstein [184] and Abu-Nada et al. [185] where exactly similar results are reported

for natural convection.

On the other hand, it is identified that the presence of magnetic dipoles affects the overall thermal distribution within the domain. For case A (Sub-figure 5.5b - Sub-figure 5.5d) and case B (Sub-figure 5.5f - Sub-figure 5.5h), the lower half of the annulus exhibits smaller temperatures. However, relatively larger magnitude of T is present throughout the domain for location C (Sub-figure 5.5j - Sub-figure 5.5l), resulting in the improved values of local (Figure 5.6) as well as average Nu (Figure 5.2) at all Mn. Also, analogous to the streamlines, all isotherms exhibits major variations in the vicinity of their corresponding dipole location. To be specific, even for smallest Mn, improved thermal performance is noticed along the inner hot wall in the upper half for case A (Sub-figure 5.5b), near the centre for case B (Sub-figure 5.5f), and in the lower half for case C (Sub-figure 5.5j). This behaviour subsequently leads to the presence of local peaks in the Nu_{local} distribution at different θ corresponding to its dipole location as shown in Figure 5.6. In addition to the local peaks, the minute undulations of case B signifies the chaotic nature of the flow structures present within the domain. Moreover, as discussed earlier, the presence of increased recirculation zones at higher Mn eventually improves the heat transfer from the inner hot wall to the surrounding ferrofluid. This specific finding can also be confirmed from the Figure 5.7, where proportional increment of Nu_{local} peaks is observed with the increase in Mn for case B.

5.3 TMC within a Circular Annulus[II]

In alignment with the work of automated heat transport devices, a numerical study is carried out for a circular annulus, where simulations are performed for three different values of remanent flux density (Br = 0.5 Tesla, 1 Tesla, and 1.5 Tesla) and three different L/D ratios (L/D = 0.125, 0.25, 0.5, refer Figure 5.8). The flow field is closely analysed with the help of local as well as averaged velocity distributions,

[II]The following work is an excerpt from the published article Dalvi et al. [176]

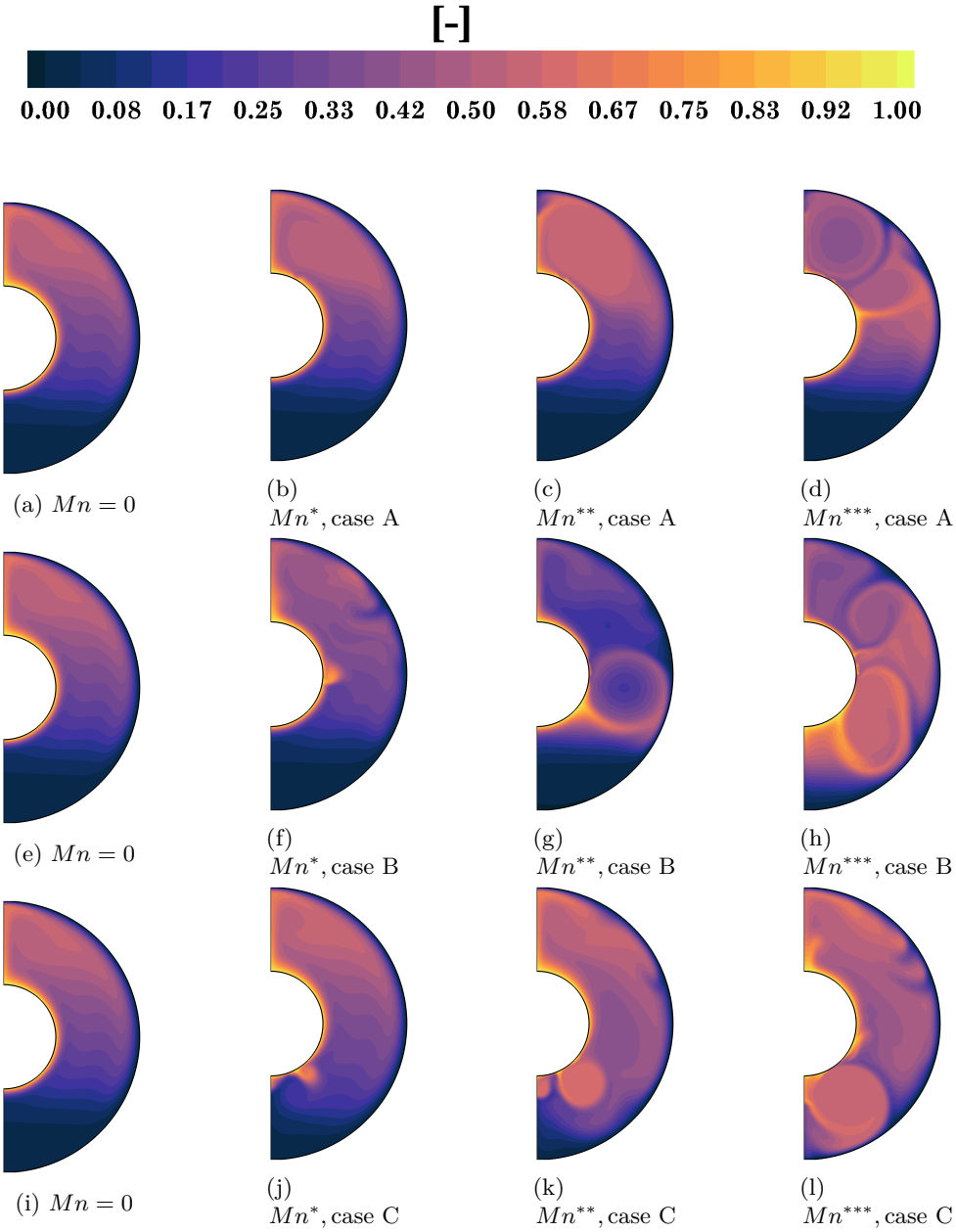

Figure 5.5: Variation of isotherms for different locations and Mn, where Mn^*, Mn^{**}, Mn^{***} corresponds to $Mn = 6.433 \times 10^{10}, Mn = 2.573 \times 10^{11}$, and $Mn = 1.029 \times 10^{12}$, respectively

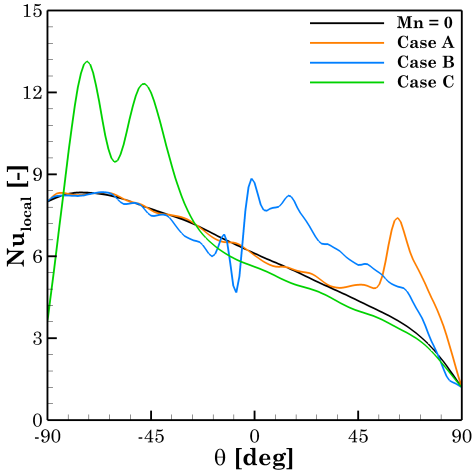

Figure 5.6: Nu_{local} distribution for different locations at $Mn = 6.433 \times 10^{10}$

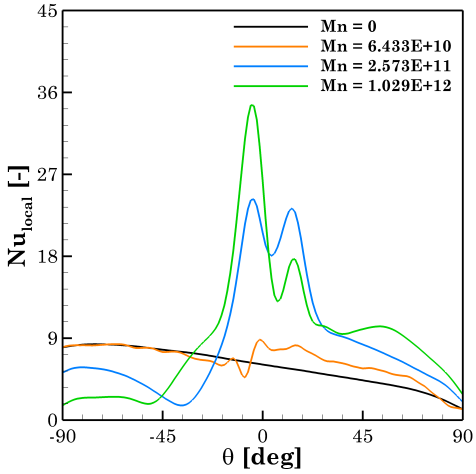

Figure 5.7: Nu_{local} distribution at different Mn for case B

and the magnitude of Nu is also compared for all distinct variations. Weiss Mean Field Theory (WMFT) is used to calculate characteristic magnetic properties and an improved viscosity model is implemented with individual precise models to determine

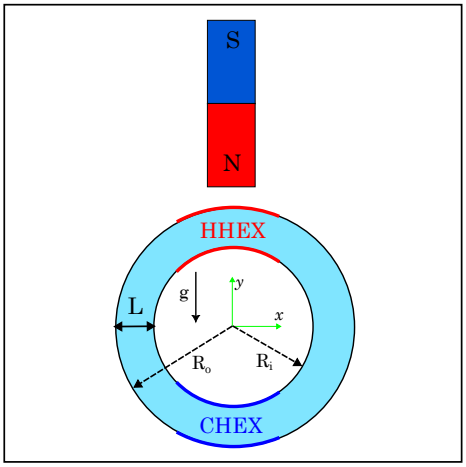

Figure 5.8: Geometrical representation of present case (Figure not to scale)

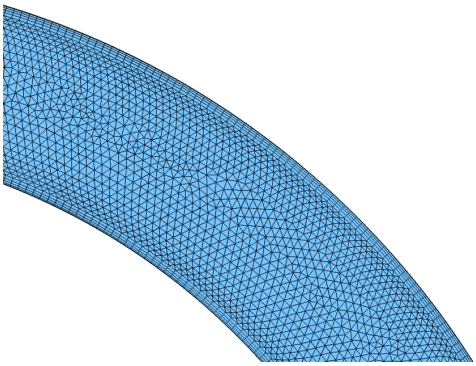

Figure 5.9: Enlarged view of discretized circular annulus

the total specific heat. Finally, to ensure that the resulting fluid motion is not merely the result of density differences, a comparison is made with and without considering the buoyancy term in the momentum equations. To keep the present chapter concise, details of grid independence study, model validation, and thermophysical properties are not mentioned here and can be obtained from Dalvi et al. [176].

5.3.1 Problem Description

For the present analysis, a magneto-caloric fluid is studied in a 2-D circular annulus with three different L/D ratios, where L represents the width between outer and inner radius, and D is the inner diameter ($D = 2Ri$) of the enclosure having a value of 0.1m. The fluid consist of a colloidal suspension of 5% Gadolinium (Gd) in kerosene. The circular enclosure is placed at the centre of a square domain with a permanent magnet at the top of it as shown in Figure 5.8. To cover the whole extent of field generated by the permanent magnet, a square domain of length $4D$ is considered as bounding region. The magnet is located at an immediate distance of $0.075D$ with its north pole facing towards the annulus. The permanent magnet used to produce the magnetic field is $1.6D$ long and has a square pole face with width of $0.4D$. As the main interest of the present analysis is to investigate the TMC in the context of MCE. To achieve the maximum magnitude of MCE, which has higher value around (T_C) [186], the initial temperature of magneto-caloric nanofluid is taken as T_C of Gd which is 292.15K [187].

5.3.1.1 Magneto-Caloric Properties

The magnitude of MCE is mainly dependent on the type of magneto-caloric material (MCM), temperature (T), and strength of magnetic field (H). For the present study, to obtain maximum MCE, we are only interested in a narrow range around T_C. At T_C, materials lose their preferred spin axis which results in decreased magnetization and undergoes a phase transition from the ferromagnetic to paramagnetic behaviour.

Due to this phase transition, qualitative or many times quantitative changes are observed in the characteristics properties of MCM. For certain MCM's, (such as Gd) a database is available that explains the variation of these properties at phase transition, but such data does not ensure overall stability and energy conservation [16]. Thus, to obtain a continuous and an approximate solution near this transition, Mean Field Theories (MFT) are widely used [188, 189].

In order to determine the characteristic properties of MCM in the present analysis, Weiss Mean Field Theory is used [188, 190]. These properties are magnetization ($M = \rho m$), partial derivative of magnetization over temperature $\left(\left(\frac{\partial M}{\partial T}\right)_H\right)$ and specific heat (C_H). Theoretical specific magnetization (m) and also its partial derivative with temperature are calculated as mentioned in literature [16, 188–191]. It is clear from Equation 5.7 - Equation 5.9, that the magnitude of m varies significantly with both T and B, so its variation is plotted as shown in Figure 5.10. These characteristic properties are then used as an input function during calculation of source terms in continuity and momentum equations (see Eq. 5.15 - 5.17).

$$m = N_s g_J J \mu_B B_J(\chi) \tag{5.7}$$

In Equation 5.7, $B_J(\chi)$ refers to the Brillouin function, which is a set of implicit equations (Eq. 5.8 and Eq. 5.9) as shown below. Here, χ represents the ratio of the

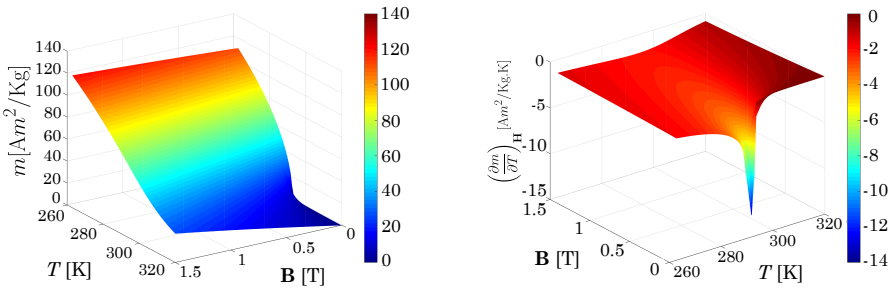

(a) (b)

Figure 5.10: Variation of magneto-caloric properties for different T and B (a) m, (b) $\left(\frac{\partial m}{\partial T}\right)_H$

Table 5.2: List of constant value parameters used in the present study

Symbol	Description	Value	Units
μ_0	Permeability of free space	1.256×10^{-6}	N/A^2
μ_B	Bohr magneton	9.274×10^{-24}	J/T
γ_e	Sommerfeld constant	6.93×10^{-2}	$J/(kg.K^2)$
N_s	Number of magnetic spins per kg	3.83×10^{24}	kg^{-1}
K_B	Boltzmann constant	1.381×10^{-23}	$m.kg/(s^2K)$
T_{Debye}	Debye temperature for Gd	169	K
χ_{vf}	Volume magnetic susceptibility of fluid	8.8×10^{-6}	m^3/kg

Zeeman energy to the thermal energy, g_J is the Landé factor, J is angular momentum. The values of all constant parameters used in the present study are mentioned in Table 5.2.

$$B_J(\chi) = \frac{2J+1}{2J}\coth\left(\frac{2J+1}{2J}\chi(B_J)\right) - \frac{1}{2J}\coth\left(\frac{1}{2J}\chi(B_J)\right) \tag{5.8}$$

$$\chi(B_J) = \frac{g_J J \mu_B \mu_0 H}{k_B T} + \frac{3T_{Curie}J}{T(J+1)}B_J(\chi) \tag{5.9}$$

5

5.3.2 Computational Methodology

5.3.2.1 Governing Equations and Boundary Conditions

Owing to their negligible conducting properties, ferromagnetic fluids are often treated as electrically insulated [30,31,192]. In accordance with this, Maxwell's Equations are solved for the present analysis as mentioned in Equation 5.1. Additionally, the flow is considered laminar, incompressible, and of Newtonian rheological behaviour. In the current study, as the volume fraction of Gd is small thus, it is assumed that nanoparticles and base fluid are in thermal equilibrium, therefore the single phase approach is used. The governing equations used to calculate the magnitude of all field variables are written in conservation form as shown below:

Continuity Equation

$$\frac{\partial u}{\partial x} + \frac{\partial v}{\partial y} = 0 \tag{5.10}$$

x - Momentum Equation

$$\rho_{nf}\left(\frac{\partial u}{\partial t}+u\frac{\partial u}{\partial x}+v\frac{\partial u}{\partial y}\right)=-\frac{\partial p}{\partial x}+\mu_{nf}\left(\frac{\partial^2 u}{\partial x^2}+\frac{\partial^2 u}{\partial y^2}\right)+F_{\mathrm{Kx}} \tag{5.11}$$

y - Momentum Equation

$$\rho_{nf}\left(\frac{\partial v}{\partial t}+u\frac{\partial v}{\partial x}+v\frac{\partial v}{\partial y}\right)=-\frac{\partial p}{\partial y}+\mu_{nf}\left(\frac{\partial^2 v}{\partial x^2}+\frac{\partial^2 v}{\partial y^2}\right)+F_{\mathrm{Ky}}+F_{\mathrm{B}} \tag{5.12}$$

Energy Equation

$$(\rho c_H)_{nf}\left(\frac{\partial T}{\partial t}+u\frac{\partial T}{\partial x}+v\frac{\partial T}{\partial y}\right)=k_{nf}\left(\frac{\partial^2 T}{\partial x^2}+\frac{\partial^2 T}{\partial y^2}\right)+\dot{Q}_{MCE} \tag{5.13}$$

Here, u, v denote x and y components of velocity respectively, T denotes temperature, and p is pressure. Density variation of the present magnetic fluid is taken into account using the Boussinesq Approximation which will generate a buoyancy force (F_B) as shown below:

$$F_{\mathrm{B}}=\rho_{nf}\beta_{nf}\left(T-T_{init}\right)g \tag{5.14}$$

Moreover, due to the response of MCM to the applied magnetic field, additional source terms such as the Kelvin force density (F_K) and the magneto-caloric heating ($\dot{Q}_{MCE}$) are considered in both momentum (Eq. 5.11 and Eq. 5.12) and energy Equation (Eq. 5.13) respectively. F_K represents the magnetic body force experienced by fluid elements [23] and when the domain is considered to be free from electric current it is calculated as shown in Equation 5.15. Being a vector quantity, F_K acts individually in both x-momentum and y-momentum equations as $F_{\mathrm{Kx}}\left(\mu_0 M\frac{\partial H}{\partial x}\right)$ and $F_{\mathrm{Ky}}\left(\mu_0 M\frac{\partial H}{\partial y}\right)$, respectively .

$$F_{\mathrm{K}}=\mu_0 M\nabla H \tag{5.15}$$

Again, to maintain the highest accuracy and replicate exact behaviour, individual contributions from fluid and solid parts are considered while calculating M, as presented in Equation 5.16.

$$M=M_f+M_s=\left(1-\phi_v\right)\rho_f\chi_{vf}H+\phi_v\rho_s m \tag{5.16}$$

Here ρ represents density of the corresponding part, χ_f denotes volume susceptibility of the base fluid, and m is calculated using Equation 5.7 - Equation 5.9. $\dot{Q}_{MCE}$ denotes cooling or heating of magnetic material in the presence of varying magnetic field [16] and it's expression is given by Equation 5.17. As the field generated by permanent magnet does not vary significantly within the present simulation time $\left(\frac{\partial H}{\partial t} \approx 0\right)$, first term of $\dot{Q}_{MCE}$ is not considered while solving equations.

$$\dot{Q}_{MCE} = -\mu_0 T \left(\frac{\partial M}{\partial T}\right)_H \frac{\partial H}{\partial t} - \mu_0 T \left(\frac{\partial M}{\partial T}\right)_H \left(u\frac{\partial H}{\partial x} + v\frac{\partial H}{\partial y}\right) \tag{5.17}$$

5.3.2.2 Numerical Procedure

For the present study, computations of all field variables are performed with the commercial software COMSOL - Multiphysics 5.4 using FEM technique [193]. Initially, the magnetic field is calculated for the whole square enclosure using Equation 5.1. This magnetic field (H) is then used along with M to solve all governing equations and calculate temperature and velocity field distributions throughout the computational domain. To handle the system of non-linear equations, a fully coupled approach is implemented and PARDISO is used as direct linear system solver. Being an unsteady analysis, four different probes are observed for their behaviour over time and all the data shown here are taken only when probes show converged values. Additionally, to ensure the continuous fluid flow, a linear gradient of temperature is implemented at both heat exchangers in horizontal direction as shown in Figure 5.11. The gradients are applied to ensure that the maximum temperature inside the annulus is at rightmost region of HHEX and the minimum temperature is at leftmost region of CHEX. The model which is used to obtain such a temperature gradient is shown in Equation 5.18.

$$\text{HHEX} = T_C + \left(\frac{x + |x_s|}{2|x_s|}\right), \ \text{CHEX} = T_C - \left(\frac{x + |x_s|}{2|x_s|}\right), \ \text{X*} = \frac{x}{\pi D} \tag{5.18}$$

Here, x is the local coordinate in the horizontal direction and x_s denotes the x coordinate at the starting point of the HEX length. The non-dimensionalised

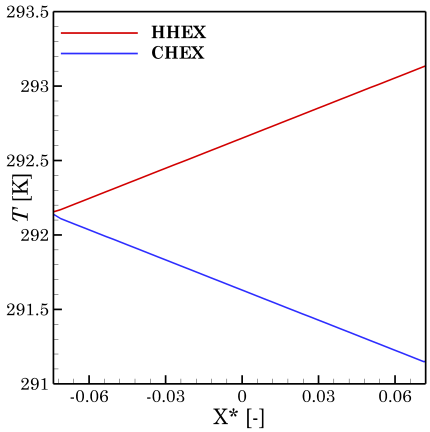

Figure 5.11: Fixed temperature gradients over length of HEX's

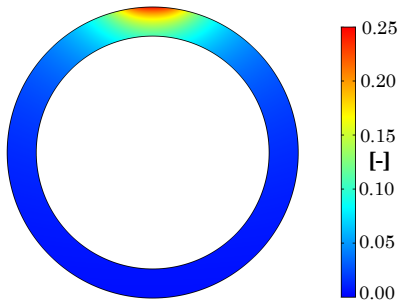

Figure 5.12: Distribution of $H^{'}$ within circular annulus for L/D of 0.125

magnetic field ($H' = \mu_0 H/Br$) produced by the permanent magnet is also shown for the smallest L/D ratio considered in Figure 5.12.

5.3.3 Results and Discussion

For the current analysis, the behaviour of TMC is studied for different Br and L/D ratios based on their flow and thermal response. The comparison is made with the help of local as well as averaged velocity distribution for all cases. Being representative of flow characteristics, velocity contours are closely observed for their unsteady behaviour. Their variation over time is plotted in non - dimensionalised form ($t^* = t/t_p$) for each case according to Equation 5.19, where S represents surface area of the annulus and t_p is the total time period taken by a fluid particle to complete one cycle. As it can be observed from Figure 5.13, the normalised surface averaged magnitude of velocity (U^*_{avg}) shows a periodic behaviour for all cases.

$$\bar{U_{avg}} = \frac{1}{S}\int_0^S U_{local}\, dS, \quad U^*_{avg} = \frac{\bar{U_{avg}}}{\left(\bar{U_{avg}}\right)_{max}}, \quad and \quad U_{avg} = \frac{1}{t_p}\int_0^{t_p} \bar{U_{avg}}\, dt \tag{5.19}$$

It is noticed from the power spectrum that, for a specific L/D, frequency and

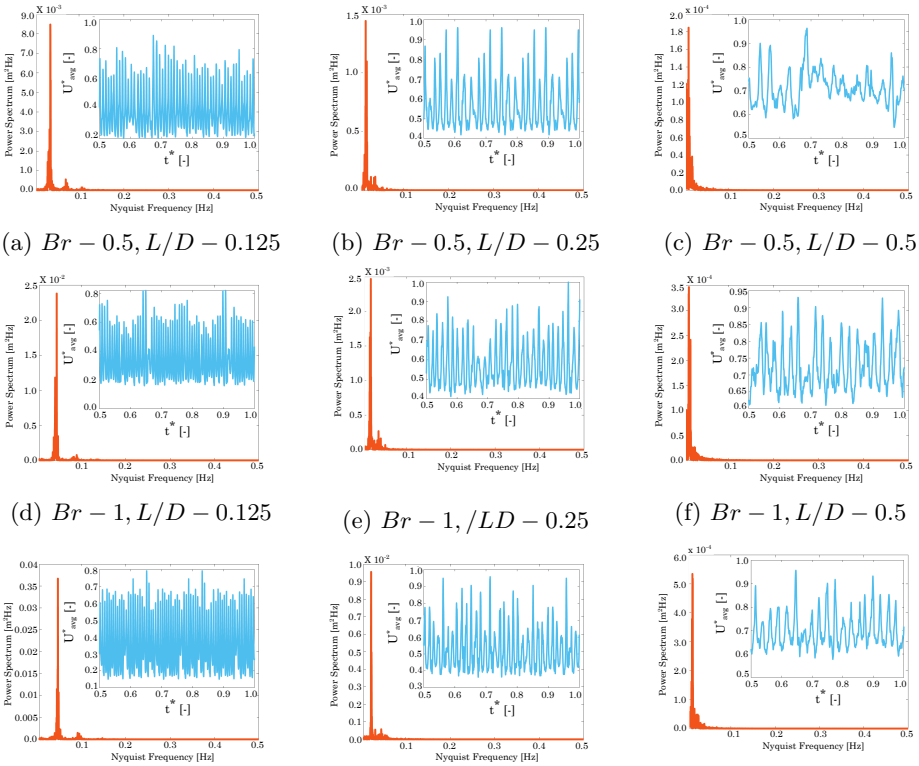

(a) $Br - 0.5, L/D - 0.125$ (b) $Br - 0.5, L/D - 0.25$ (c) $Br - 0.5, L/D - 0.5$

(d) $Br - 1, L/D - 0.125$ (e) $Br - 1, /LD - 0.25$ (f) $Br - 1, L/D - 0.5$

(g) $Br - 1.5, L/D - 0.125$ (h) $Br - 1.5, L/D - 0.25$ (i) $B - 1.5, L/D - 0.5$

Figure 5.13: Power spectrum of U_{avg} for different Br and L/D (For an enlarged version of these figures, all readers are humbly requested to refer Dalvi et al. [176])

strength increases with increase in magnitude of the applied field. It means that for the same geometrical configuration, less time is required for fluid particles to complete its cycles within the annulus. This eventually will improve heat transfer rate between both heat exchangers. It can be explained as, the value of U^*_{avg} depends considerably on the magnitude of the source terms in both momentum and energy equation. These source terms (F_K and $\dot{Q}_{MCE}$) again rely upon the strength of the externally applied magnetic field. Thus, for increased values of Br an improved TMC mechanism is observed for a particular L/D ratio. On the other hand, if we compare three different geometrical configurations of the same Br, a totally contrary trend

is observed. For all three magnitudes of Br, frequency as well as strength of U^*_{avg} decreases with increase in L/D value. This is mainly because for a specific Br, the influence of source terms reduces as the driving force gets distributed over a wider region with increase in L/D. Among all cases, the maximum frequency is observed for the highest magnetic field and smallest L/D i.e. Figure 5.13g.

For a complete insight of flow structures and their development, velocity contours for three different geometrical configurations of highest Br are compared over time in Figure 5.14. Initially, for all configurations, fluid elements are randomly arranged throughout the annulus with no specific orientation preferences. But as time progresses, due to the combined effect of $\dot{Q}_{MCE}$ and the applied temperature gradient, fluid particles adjacent to the rightmost part of HHEX will gain some energy and reach to higher temperature relative to its surrounding fluid. Now, due to their thermo-magnetic characteristics, fluid particles with increased T experience a reduced value of the magnetic susceptibility. This susceptibility difference eventually results in movement of these fluid elements to the region of lower magnetic field which is in the bottom half of annulus as can be seen from Figure 5.12. When these fluid particles enter CHEX, they exchange heat and reach to the leftmost part with having temperature values smaller than their ambient fluid. It results in an increase in magnetisation and particles will try to reach to the high magnetic field zone i.e. the upper half. This is how the fluid elements within the annulus are exhibiting a periodic fluid motion in clockwise direction. In general, it is observed that the magnitude of the local velocity decreases with the increase in the width between outer and inner radius. Thus, its highest value is observed for L/D of 0.125. For all three configurations, few fluid elements near to CHEX also try to reach to higher magnetic region along the inner circumference. This flow offers some resistance on the right half, while work in favour of mainstream velocity for the left half of annulus. As a result of this, some interesting flow patterns are observed for L/D of 0.5. Due to its wider span, this combination of opposite flow streams along inner and outer circumference results in the formation of alternate clockwise and anticlockwise local

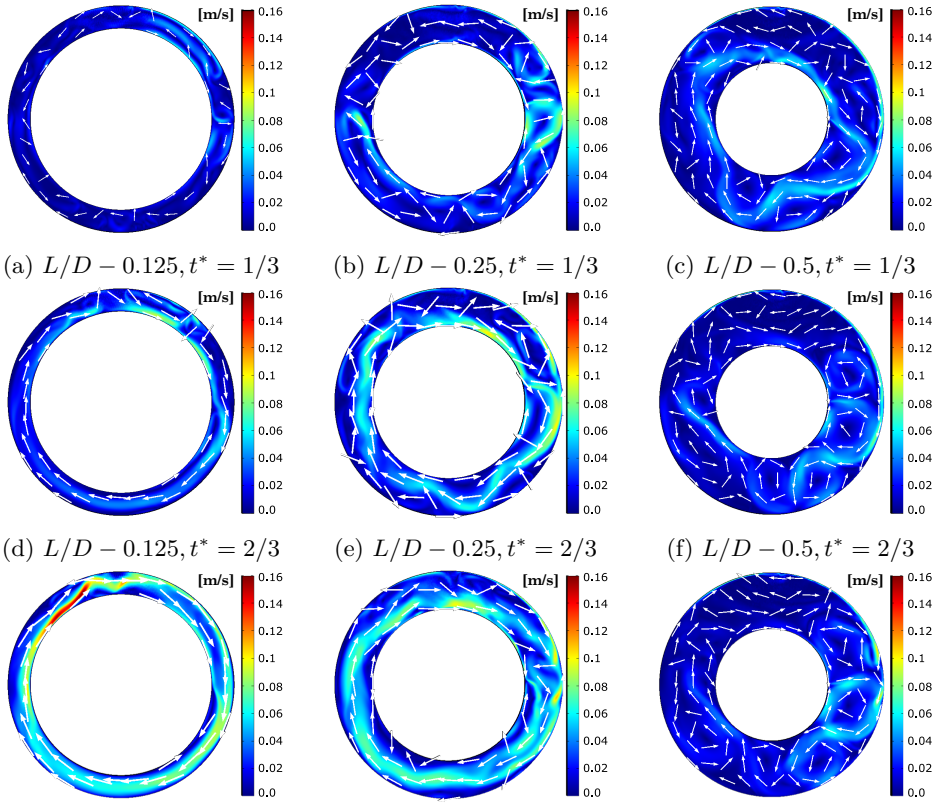

(a) $L/D - 0.125, t^* = 1/3$ (b) $L/D - 0.25, t^* = 1/3$ (c) $L/D - 0.5, t^* = 1/3$

(d) $L/D - 0.125, t^* = 2/3$ (e) $L/D - 0.25, t^* = 2/3$ (f) $L/D - 0.5, t^* = 2/3$

(g) $L/D - 0.125, t^* = 1$ (h) $L/D - 0.25, t^* = 1$ (i) $L/D - 0.5, t^* = 1$

Figure 5.14: Development of velocity contours over time for different L/D at Br of 1.5 Tesla

vortices on the right half of the domain as displayed in Figure 5.14f and Figure 5.14i. This formation of alternative vortices is also responsible for the reduced magnitude of average velocities for all cases of 0.5 L/D. As it can be clearly noticed from Figure 5.15, for a distinct magnetic field, the magnitude of U_{avg} shows lower value for a wider geometrical configuration. On the other hand, a substantial increment is observed if we raise the magnetic strength for a particular L/D. This behaviour can be primarily attributed to the influence of F_K term in the momentum equations.

Also, to have a better understanding about heat transfer mechanism, Nu_{avg} is

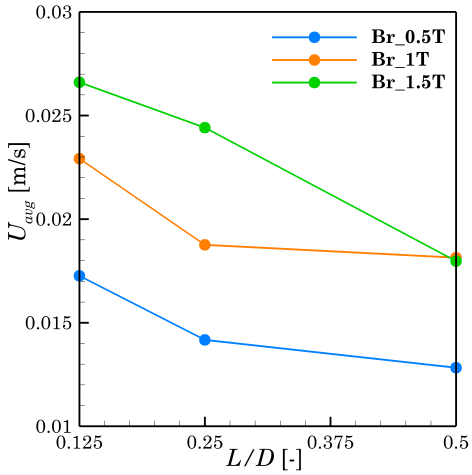

FIGURE 5.15: Comparison of U_{avg} with L/D for different Br

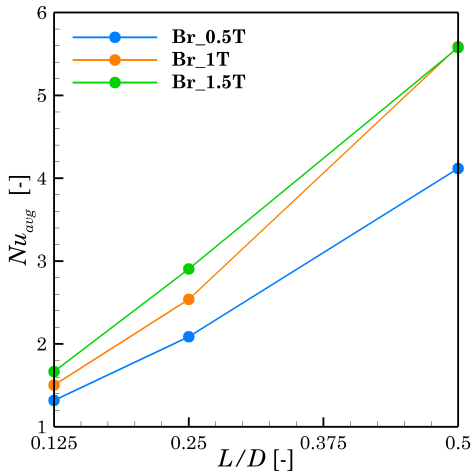

FIGURE 5.16: Comparison of Nu_{avg} with L/D for different Br

plotted for all three variations of Br and L/D. The time averaged value of Nu is integrated over the whole domain and compared for all cases. It is observed that, for a specific L/D, the magnitude of Nu_{avg} increases with increase in Br. It is mainly because, as mentioned in Equation 5.20, Nu_{avg} is directly influenced by the magnitude of net convective heat flux (Q_c). This Q_c is further affected by the strength of $\dot{Q}_{MCE}$ which again increases with Br. A similar trend of increment in Nu_{avg} is observed if we go on increasing L/D for a particular Br. Thus, the maximum value of Nu_{avg} is obtained for the case of 0.5 L/D with highest Br as shown in Figure 5.16.

$$Nu_{local} = \frac{Q_c L}{k_{nf} T}, \quad \bar{Nu} = \frac{1}{S}\int_0^S Nu_{local}\, dS, \quad and \quad Nu_{avg} = \frac{1}{t_p}\int_0^{t_p} \bar{Nu}\, dt \tag{5.20}$$

TABLE 5.3: Effect of F_B on U_{avg} and Nu_{avg} for L/D of 0.125 at $Br = 1.5$ Tesla

Case	$U_{avg}[m/s]$	$Nu_{avg}[-]$	% Error
With F_B	0.026607	1.666349	1.153
Without F_B	0.026914	1.678811	0.747

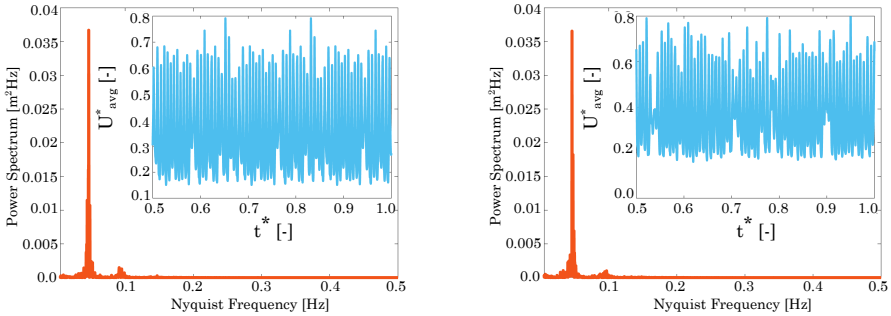

Figure 5.17: Comparison of power spectrum of U_{avg} for L/D of 0.125 at $Br = 1.5$ Tesla (a) With F_B, (b) Without F_B

At the end, in order to closely analyse the exclusive contribution of the buoyancy force to the fluid rotation, a comparison is made with and without including the F_B term in the y- momentum equation (Eq. 5.12). Values of U_{avg} and Nu_{avg} are compared for the case of highest magnetic strength and smallest L/D along with their power spectrums. As it is clearly observed from Table 5.3 and Figure 5.17, F_B has an insignificant contribution in flow development. Thus, it can be evidently said that for all the cases of current framework, the fluid flow is occurring entirely because of magnetic forces (F_K and $\dot{Q}_{MCE}$) and is not an outcome of the density difference inside the annulus.

CHAPTER 6

Prototype Simulations of Cooling Systems

In the present chapter, the numerical model described in Section 4.4 is implemented to replicate MCE based cooling process. To do this, the thermo-physical and the magnetic properties from Chapter 3 are used. Initially, a single stage cooling system is best understood with the help of different flow variables. The numerical methodology used for single stage configuration is discussed extensively in Section 6.2 along with the grid convergence study and discretization schemes. Finally, two distinct multi-stage arrangements are discussed in Sub-section 6.3.2 which employs cascading principle to expand the operational temperature span.

6.1 Problem Description

6.1.1 Geometrical Details

To obtain a room temperature cooling effect using the MCE, a single 3D toroidal loop has been considered as shown in Figure 6.1. The proposed design consists of a Hot Heat Exchanger (HHEX), a Cold Heat Exchanger (CHEX), a magnetic field source, MCS, and a magnetic pump. The MCS consists of a colloidal mixture of MCM particles in a heat transfer fluid. The MCM used in the present work is LaFeMnSiH (Calorivac - H) which is commercially offered by Vacuumschmelze GmbH. Whereas, a liquid metal GaInSn-68.5%21.5%10% (often termed as Galinstan) is used as base fluid for its superior thermal properties (higher k and smaller Cp) over conventional heat transfer fluids. The magnetic field source is employed to stimulate the adiabatic temperature rise/drop of MCM within the system. The overall setup operates on a

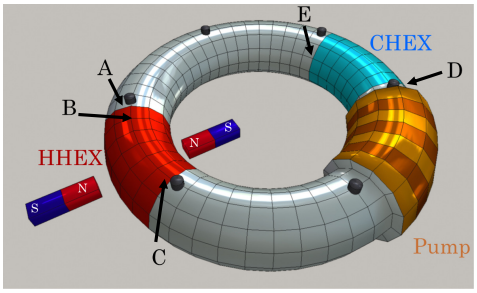

Figure 6.1: Schematic of the 3D toroidal prototype

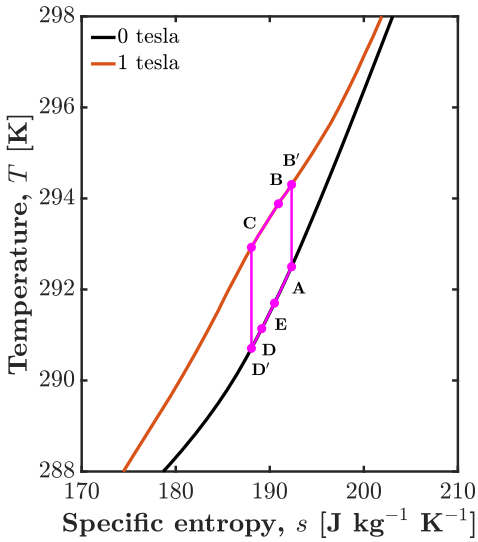

Figure 6.2: $T - s$ curve of magnetic Brayton cycle for Calorivac - H (From Rajamani [19])

magnetic Brayton cycle, where each thermodynamic process is described as follow

- *Adiabatic magnetization* (process A - B) : Due to the MCE, as the MCS enters the strong magnetic field region, it experiences sudden rise in temperature (to conserve the $\Delta S = 0$) as explained in Section 1.2.

- *Isomagnetic heat rejection* (process B - C) : This supplementary heat is then transferred to the surrounding domain via a HEX in the constant magnetic field.

- *Adiabatic demagnetization* (process C - D) : Once the MCS exit from HHEX, it experiences a loss of magnetic field as it enters an adiabatic region where its temperature further drops.

- *Isomagnetic heat absorption* (process D - A) : This aforementioned MCS (which is at a relatively lower T) is then passed through a CHEX where the heat is absorbed from surrounding and the desired cooling effect is achieved.

The equivalent representation of all the above processes on the $T - s$ curve is shown in Figure 6.2. The data is plotted for the Calorivac - H at two different **H** magnitudes (0 Tesla and 1 Tesla), where process B'- B and process D'- D are assumed to be instantaneous.

However, a more pragmatic and an experimentally feasible design is chosen initially for single stage system that has a 3D U shape arrangement with circular cross-sectional area as shown in Figure 6.3. Based on the previous work done in the similar context [19], the D_h for the circular cross-section is selected as 0.02m and both HEX are considered to be 0.5m long. An additional length is provided before HHEX and after CHEX to avoid sudden flow disturbances. Further, the

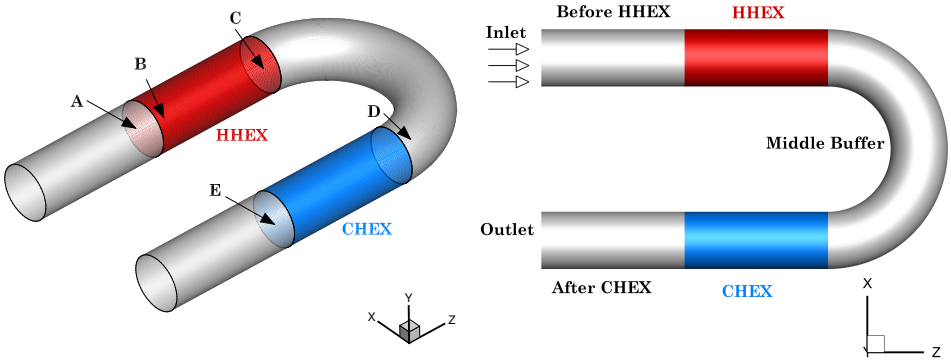

(a) (b)

Figure 6.3: Description of the 3D U shape domain (not to scale) (a) Iso-metric view with notations for thermodynamic process, (b) Top view

HHEX and CHEX are separated by a "Middle Buffer" length to allow the adiabatic demagnetization of the MCS.

6.1.2 H Field Arrangement & Thermo-physical Properties

As discussed in Section 1.2, the magnitude of adiabatic temperature rise/drop is proportional to the strength of applied magnetic field. Thus, a strong magnetic field is desired for the maximum temperature changes within the current system. The foremost preference for a strong uniform **H** is an electromagnet due to its precise ability to generate magnetic field by passing varying current. However, owing to the associated Joule heating, use of electromagnets is neglected as it contradicts the essential objective of the present setup i.e to have a cooling effect. Hence, to obtain a large, uniform magnetic field, the possibility of using permanent magnets is explored.

After careful comparison [194], an enclosed Halbach array is considered in which a set of eight permanent magnets are arranged in a specific manner as shown in Figure 6.5a.

The magnets are arranged around a central void that refers to the HHEX region where the strong field is required. The obtained **H** distribution is computed in COMSOL - Multiphysics [193] and its variation at a cross-section is visualised as shown in Figure 6.5b. Moreover, this exact field distribution with a H_{max} of 1.03 T is then implemented in OpenFOAM (via `funkySetFields`) for the 3D U shape to replicate the Halbach array as shown in Figure 6.4.

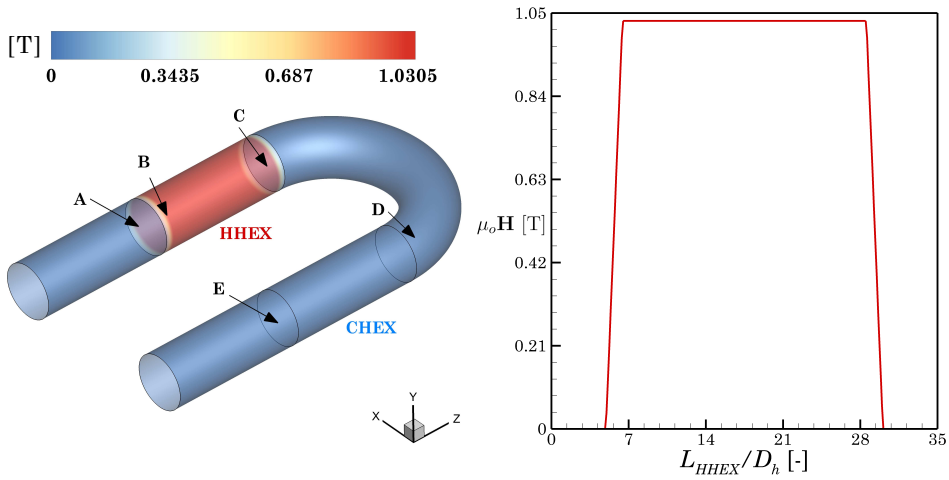

(b)

(a)

Figure 6.4: Implementation of the Halbach array for single stage analysis in the OpenFOAM framework (a) Iso-metric contour, (b) **H** variation along the axis of HHEX

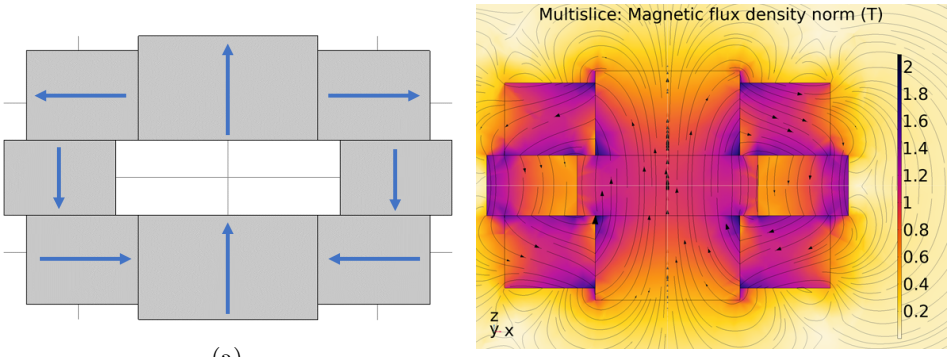

(a) (b)

Figure 6.5: Visualization of the Halbach array (From Groot [194]) (a) Direction of the internal field for each distinct magnet, (b) Cross-sectional view of magnetic field distribution

Moreover, to optimize the system performance, the initial temperature of MCS is chosen to be 292.5K. Furthermore, the boundary condition for all flow variables are mentioned in Table 6.1, whereas the required thermophysical properties are determined according to Table 6.2. Here, the inlet velocity (U_{in}) of the MCS is finalised based on a specific heat transfer requirement. For the current objective, energy gained due to MCE should be transferred to surrounding domain within HHEX region (process B - C). Thus, only the radial heat transfer is beneficial for the present context. However, owing to the large thermal conductivity of Galinstan,

Table 6.1: Information about the boundary conditions used in the present work

Patch	p	U	T
Inlet	$\partial p/\partial n = 0$	U_{in}	T_{amb}
Before HHEX Wall	$\partial p/\partial n = 0$	$U_i = 0$	T_{amb}
HHEX Wall	$\partial p/\partial n = 0$	$U_i = 0$	T_{amb}
Middle Buffer Wall	$\partial p/\partial n = 0$	$U_i = 0$	$\partial T/\partial n = 0$
CHEX Wall	$\partial p/\partial n = 0$	$U_i = 0$	T_{CHEX}
After CHEX Wall	$\partial p/\partial n = 0$	$U_i = 0$	T_{amb}
Outlet	p_{atm}	$\partial U/\partial n = 0$	$\nabla T \cdot n = 0$

Table 6.2: Details of the thermo-physical variables

Variable	Obtained from
ρ_m	Equation 3.2
μ_{MCS}	Figure 3.11 and Equation 3.7 - 3.9
k_m	Equation 3.3
$(C_p)_m$	Figure 3.8 and Equation 3.4
$\mathbf{M}$	Figure 3.5
$\left(\frac{\partial M}{\partial T}\right)_H$	Figure 3.6

there exists a possibility of heat transfer in the axial direction. Hence, to avoid it, the Pe is kept at a higher magnitude ($Pe > 50$), such that the axial conduction is insignificant [195]. This criteria results in the distinct inlet velocities (U_{in}) for each ϕ_d that ensures the dominating radial heat transfer.

6.2 Computational Methodology

6.2.1 Grid Distribution & Grid Convergence Study

In accordance with the circular cross-section of the considered geometry, O-grid arrangement is implemented for the domain discretization. The structured non-uniform hexahedral mesh elements are generated using the non-orthogonal block arrangement. The grid distribution for the complete domain along with the cross-sectional area is shown in Figure 6.6. As discussed in Section 4.1, the current solid-liquid interaction belongs to a dispersed flow category. To resolve such a class of multiphase flows using an Eulerian based approach, the major objective is to bypass the exact spatial resolution of the secondary phase while replicating the interactions via correlations. This is essential to support the mathematical formulations that are used in determining the complete system behaviour. Thus, to ensure this constraint,

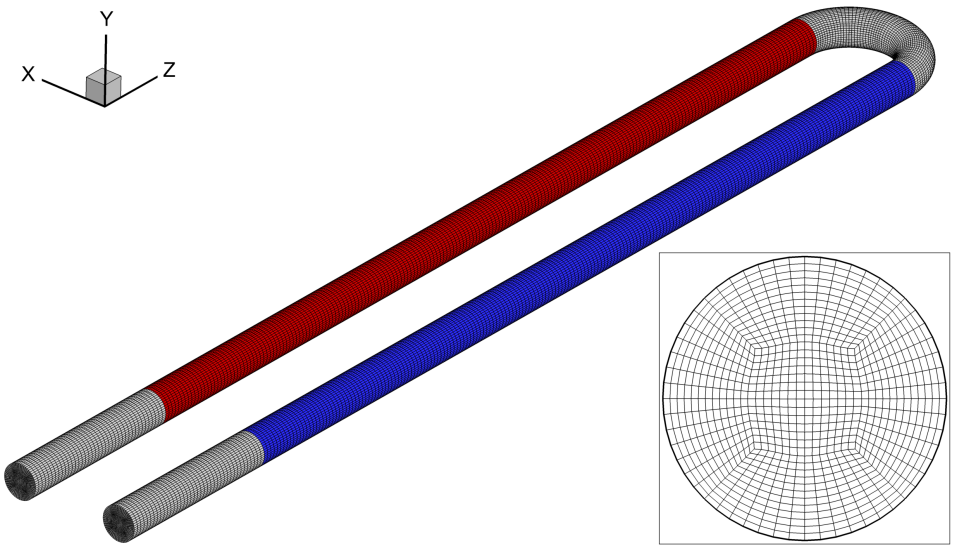

Figure 6.6: Grid distribution of the considered domain

the hexahedral cells are generated such that the min edge length in the domain is several times larger than the particle size of the Calorivac.

Further, to establish the least possible discretization error, 5 different grids are compared for their thermo-fluid behaviour. The comparison is performed for the flow of 40% Calorivac-H with d_p of 50 µm. The **H** field distribution is implemented based on Figure 6.4b and the remaining variables are assigned as per Table 6.2. For all the considered grids, the variation of T distribution along the axial centreline

Table 6.3: Details about the grid independence study

	Total elements	$\widetilde{U}_{y=0}$ [m/s]	$\widetilde{T}_{y=0}$ [K]
Grid 1	129360	1.248134×10^{-2}	291.9621
Grid 2	209088	1.268292×10^{-2}	291.9619
Grid 3	321074	1.172241×10^{-2}	291.9599
Grid 4	456568	1.169577×10^{-2}	291.9597
Grid 5	634740	1.161474×10^{-2}	291.9595

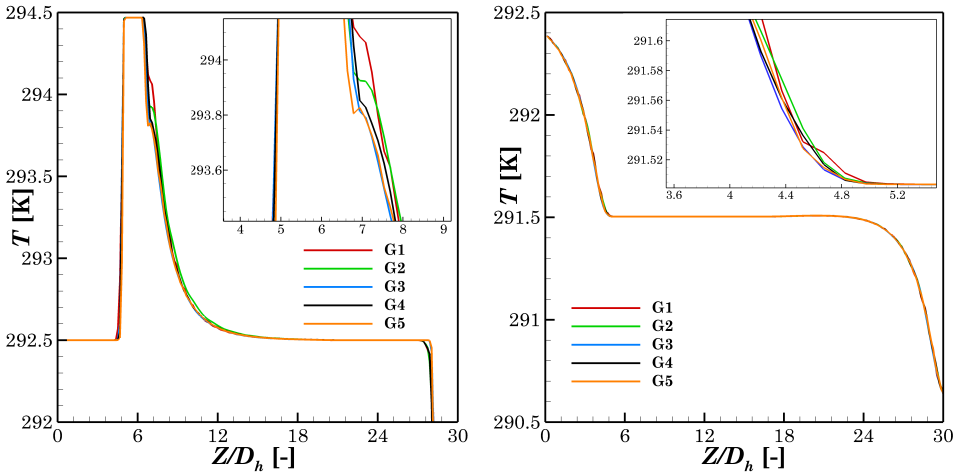

(a) (b)

Figure 6.7: T variation along the axial centreline for (a) HHEX (flow direction from $Z/D_h = 0$ to $Z/D_h = 30$), (b) CHEX (flow direction from $Z/D_h = 30$ to $Z/D_h = 0$)

of both HEX domain is shown in Figure 6.7. The decreasing slope in HHEX curve (Sub-figure 6.7a) represents the heat rejection by MCS, while the Sub-figure 6.7b refers the temperature gain from ambient within CHEX. Additionally, the surface averaged magnitude of velocity ($\widetilde{U}$) and temperature ($\widetilde{T}$) (defined in Equation 6.1) is compared at the axial mid section ($y = 0$) in Table 6.3. Based on these observations, Grid 4 is finalised for all the remaining simulations to secure a stable equilibrium between computational cost and numerical accuracy.

$$\widetilde{T} = \frac{1}{S}\int_0^S T\, dS \;\text{ and }\; \widetilde{U} = \frac{1}{S}\int_0^S U\, dS \;\text{ where }\; U = \sqrt{{U_x}^2 + {U_y}^2 + {U_z}^2} \tag{6.1}$$

6.2.2 Model Validation

No work is available in the literature that provides experimental measurements in a similar context of internal MCM flow for room temperature cooling applications. However, to authenticate our work, an analogous case is chosen where the flow domain, volume fraction (ϕ_d), and solid particle size (d_p) are within a comparable range of the present numerical work. The validation study is carried out to replicate the experimental work performed by Zambrano et al. [147] that investigates the internal flow of a dense slurry in a straight horizontal pipe. The slurry used for the measurements consists entirely of asphaltic residuals of mean particle size 500µm suspended within a de-asphalted oil. Authors reported the mixture pressure drop (Δp_m) measured across a section of 2.5m using Differential Pressure Transducers (DPT) for 2 specific weight fractions (C_w) and 5 different $\mathbf{U}_m$. In addition to the experimental measurements, the numerically obtained Δp_m is also compared with the theoretical values using the Darcy–Weisbach equation mentioned below

$$\Delta p_m = \frac{f_D L \rho_m \mathbf{U}_m^2}{2D_h} \quad \text{where} \quad f_D = \frac{16}{Re_p}, \qquad Re_p = \frac{\rho_c U_t d_p}{\mu_c}, \quad \text{and} \quad U_t = \frac{(\rho_d - \rho_c)\, g d_p^2}{18\mu_c} \tag{6.2}$$

6

Overall, it can be observed from the Figure 6.8 that Δp_m increases with the increase in U_m, whereas for a specific mixture velocity, the pressure drop improves with the C_w. This is mainly as increased solid particles in the slurry will enhance the overall mixture viscosity that results in higher frictional losses. Further, it is also noticed that at smaller $\mathbf{U}_m$, the numerical results agree closely with the experimental as well as with the theoretical values computed using the Equation 6.2. However, with the increase in $\mathbf{U}_m$, a discrepancy is observed between experimental measurements and theoretical magnitude. This deviation is mainly attributed by

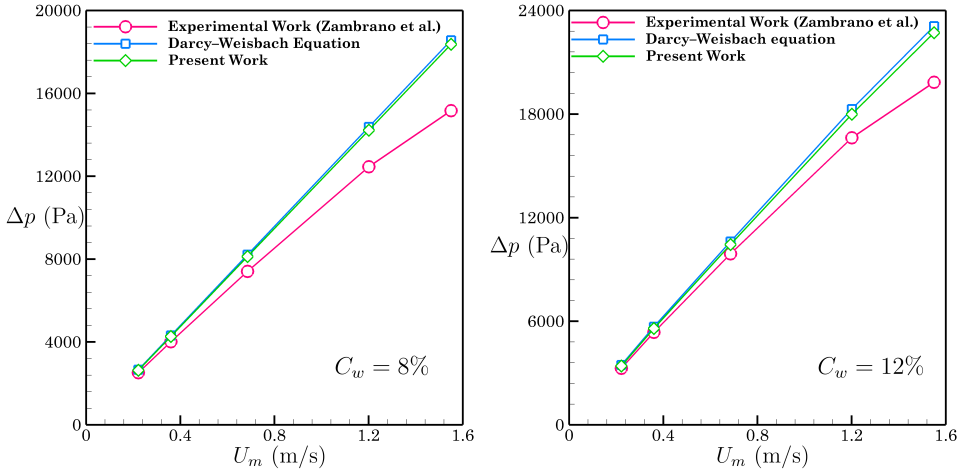

(a) (b)

Figure 6.8: Comparison of numerical Δp_m for various U_m with the Darcy–Weisbach equation and Zambrano et al. [147] at different weight fractions (a) For $C_w = 8\%$, (b) For $C_w = 12\%$

the authors to the partial breakdown of solid particles inside the slurry besides the change of thermo-physical properties with temperature.

6.2.3 Numerical Method

The aforediscussed governing equations of Section 4.4 are solved with the help of a C++ based open-source CFD Toolbox OpenFOAM [38]. It is a general purpose PDE solver that implements Finite Volume Method based discretization for all the flow variables. The diffusive terms of all governing equations are discretized using a second order central difference scheme, whereas the convective terms are solved using an upwind biased second order accurate scheme. Additionally, the temporal marching of the simulation is performed using the second order backward difference scheme. The pressure velocity coupling is obtained with the help of PIMPLE algorithm [196] that

is specific to OpenFOAM framework. It is essentially a combination of PISO and SIMPLE algorithm [197,198] that enables computing the stiff system of PDE's such as complex transient flows. Moreover, while solving iterative matrices, the corresponding $\mathbf{M}$ and $\left(\frac{\partial M}{\partial T}\right)_H$ at each time step is obtained as a multi-variable function using Figure 3.5 and Figure 3.6, respectively. Finally, the generalised algebraic multi grid solver is used to solve the symmetric matrices of the resulting algebraic equations, whereas smooth-Solver is used for asymmetric part along with diagonal based incomplete LU preconditioner.

6.3 Results & Discussion

6.3.1 Single Stage Arrangement

The present section discuss the overall behaviour of a MCE based single stage cooling effect observed within a 3D U shape arrangement shown in Figure 6.6. The boundary conditions and the thermophysical properties of all field variables are implemented as per Table 6.1 and Table 6.2, respectively. In addition to this, suspended Calorivac-H particles of 50 µm are used with the $\mathbf{H}$ distribution of 1.03 Tesla and T_{amb} of 292.5K. In order to comprehend different underlying mechanisms, each test case is analysed by observing flow variables. Overall, it is noticed that the presence of additional volumetric magnetic forces results in distinct hydro-thermal interactions.

6

6.3.1.1 Effect of ϕ_d

To understand the influence of MCM used, a comparative study is performed at three different volume fractions ($\phi_d = 20\%, \phi_d = 30\%,$ and $\phi_d = 40\%$) of Calorivac-H[I] where

[I] The largest ϕ_d considered for comparison is chosen based on the DMM validity constraint obtained from Equation C.4

T of CHEX wall is set at 292K. The temperature distribution contours are observed at two mid planes for each ϕ_d as shown in Figure 6.9. Overall, it is noticed that the temperature span across the domain is proportional to the amount of Calorivac used. In alignment with the processes discussed in Section 6.1, MCS demonstrate the increased T magnitude at the entry of HHEX for each ϕ_d. This elevated temperature is then transferred to the surrounding domain along the flow direction. Once the MCS comes out of HHEX, the T contours exhibit reduced magnitude in the middle buffer length (curved section) due to adiabatic demagnetization. This eventually enables heat transfer from the neighbouring area to MCS via CHEX at all three ϕ_d.

Moreover, the thermal statistics ($T_{min}, T_{max}, T_{avg}$) are also compared for different volumetric domains (HHEX, Middle Buffer and CHEX) as shown in Sub-figure 6.10a - Sub-figure 6.10c, respectively. It is noticed that for the HHEX region, increment in T_{max} and reduction in T_{min} is proportional with ϕ_d. This can be mainly attributed to the T_{ad} change (Equation A.8) that eventually depends on the amount of MCM used. On similar lines, the lowest T_{min} is noticed for the highest ϕ_d within Middle Buffer. Additionally, as this region is not interacting any energy with its surrounding, both T_{max} and T_{avg} also decrease with ϕ_d. The MCS with such lower T_{min} then enters the CHEX, where it absorbs the heat that enables its T_{avg} and T_{max} to saturate around T_{amb}. Lastly, the Heat Rejection Rate and Cooling Capacity (shown in Equation 6.3) are also compared which confirms the overall improved performance of HHEX and CHEX at higher ϕ_d.

$$\begin{aligned} \text{HRR} &= \dot{m}\,(C_p)_m\,(T_{max,\text{HHEX}} - T_{min,\text{HHEX}}) \text{ and} \\ CC &= \dot{m}\,(C_p)_m\,(T_{max,\text{CHEX}} - T_{min,\text{CHEX}}) \end{aligned} \tag{6.3}$$

Furthermore, the distribution of temperature gradient along both angular (θ) and axial (z) direction is also observed at both HEX's as demonstrated in Figure 6.11.

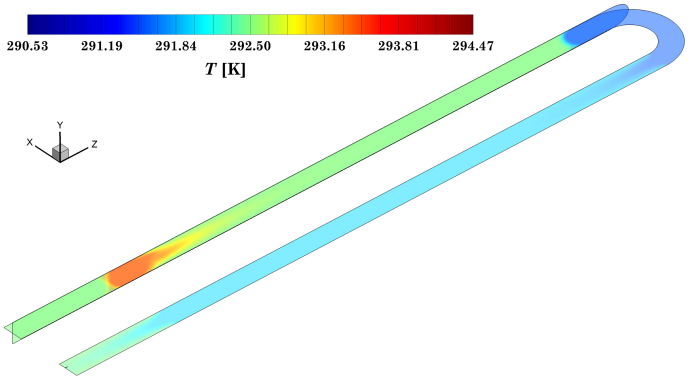

(a)

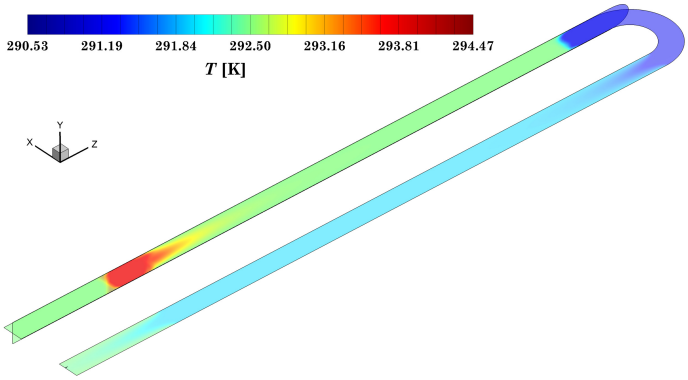

(b)

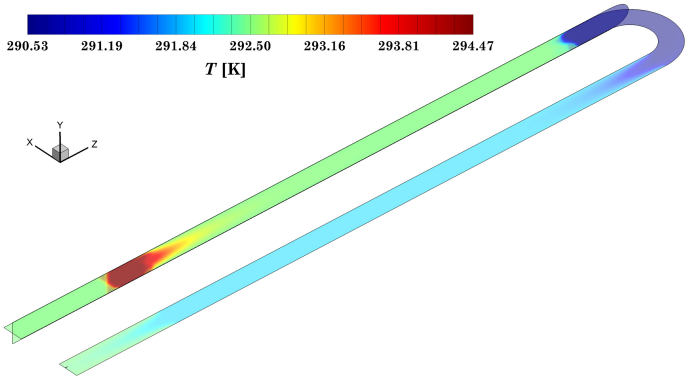

(c)

Figure 6.9: Comparison of T distribution at different volume fractions (a) For $\phi_d = 20\%$, (b) For $\phi_d = 30\%$, (c) For $\phi_d = 40\%$

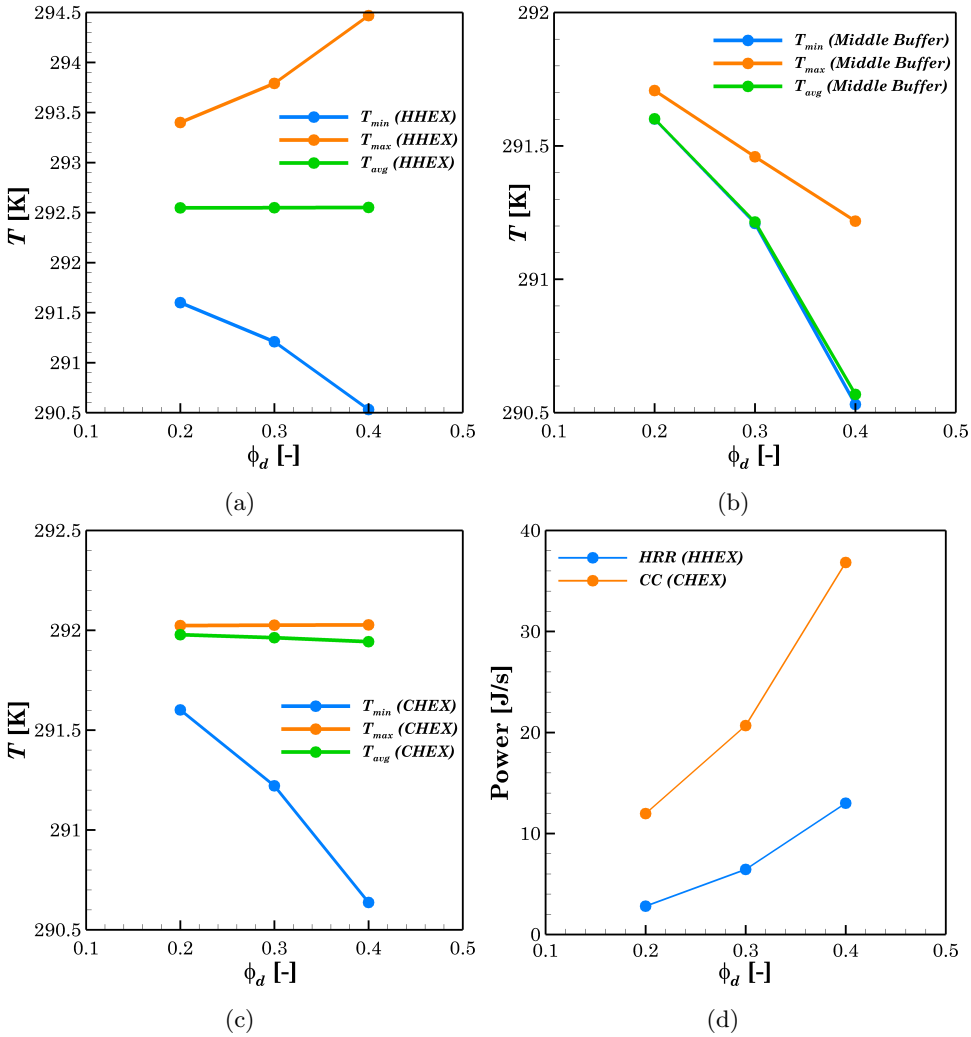

Figure 6.10: Effect of ϕ_d on (a) T stats of HHEX, (b) T stats of Middle buffer, (c) T stats of CHEX, (d) Heat Rejection Rate and Cooling Capacity

Overall, for both HHEX and CHEX, the $\partial T/\partial n$ exhibits proportional increment with ϕ_d. It is noticed that for all HHEX (Sub-figure 6.11a - Sub-figure 6.11e), $\partial T/\partial n$ shows negative magnitudes at the entry, whereas positive values are noticed towards the exit of HHEX. This is mainly attributed to the T_{ad} rise which leads to the heat

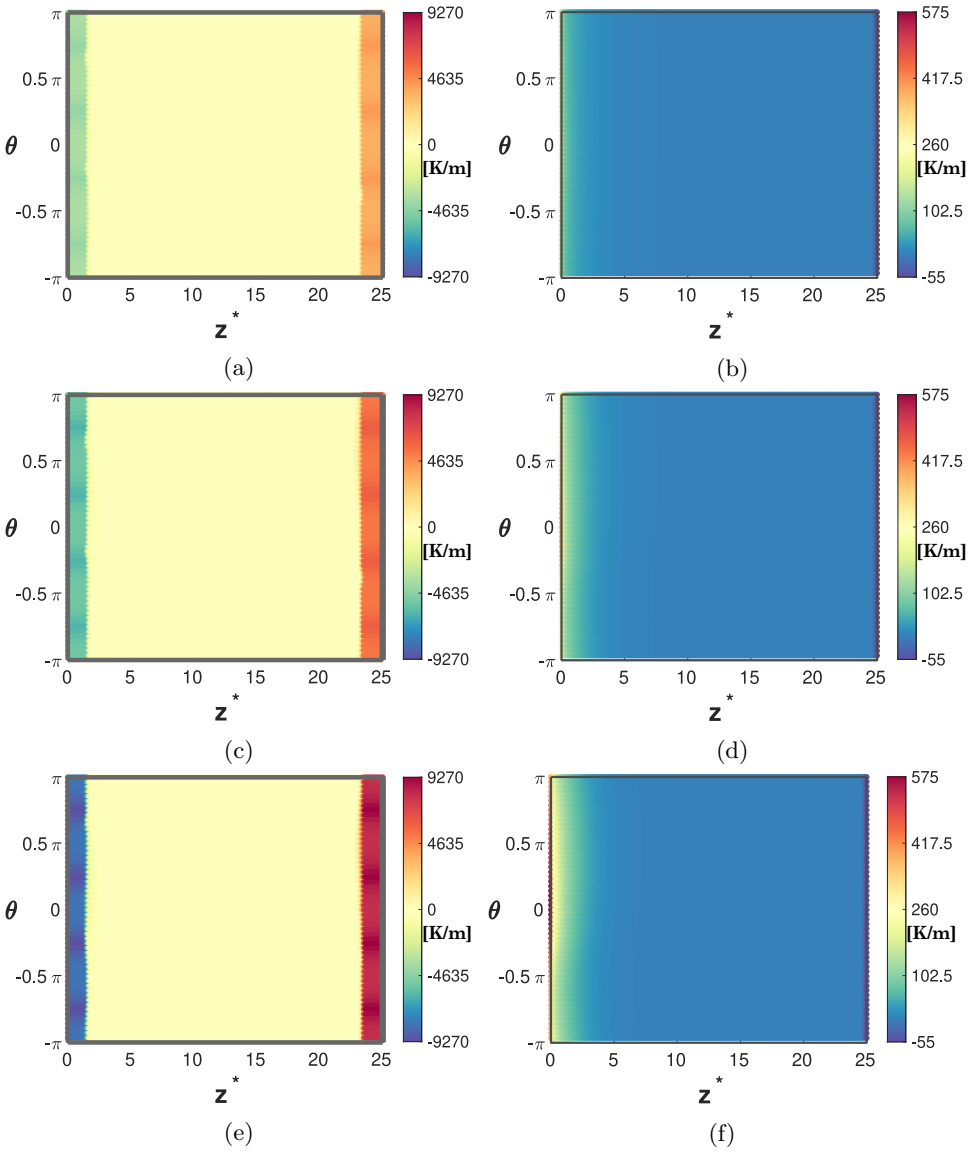

Figure 6.11: $\partial T/\partial n$ distribution in the axial ($z^* = z/D_h$) and angular (θ) direction (a) For $\phi_d = 20\%$ at HHEX, (b) For $\phi_d = 20\%$ at CHEX, (c) For $\phi_d = 30\%$ at HHEX, (d) For $\phi_d = 30\%$ at CHEX, (e) For $\phi_d = 40\%$ at HHEX, (f) For $\phi_d = 40\%$ at CHEX

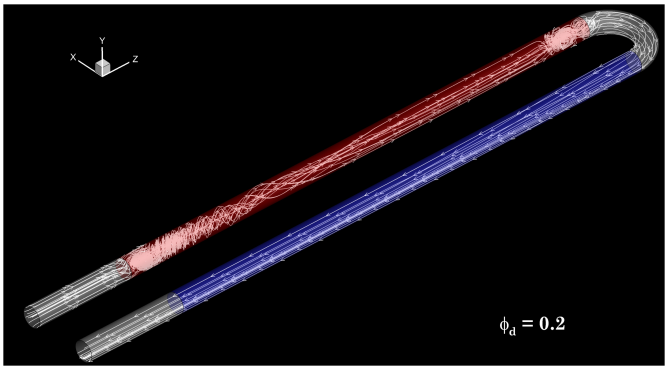

(a)

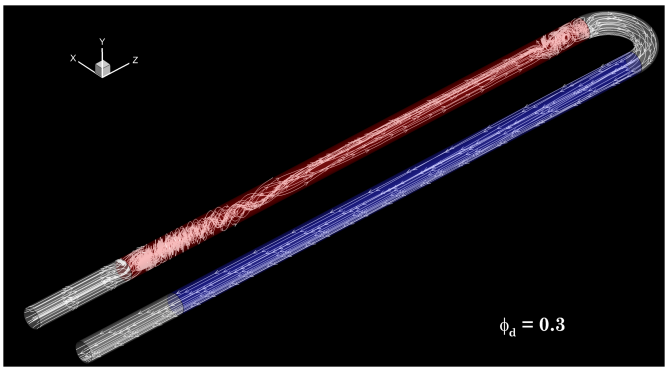

(b)

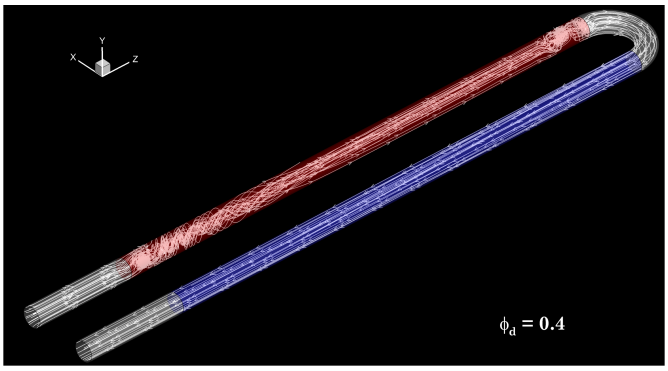

(c)

Figure 6.12: Comparison of streamlines at different volume fractions (a) For $\phi_d = 20\%$, (b) For $\phi_d = 30\%$, (c) For $\phi_d = 40\%$

transfer from the MCS to ambient at entry and vice versa at exit. The axial span of $\partial T/\partial n$ at both ends of HHEX corresponds to the **H** distribution (from sub-figure 6.4b) which results in T_{ad} rise/drop due to MCE. In the context of CHEX (Sub-figure 6.11b - Sub-figure 6.11f), the heat is absorbed from the surrounding in the entry region leading to the positive $\partial T/\partial n$. This added heat is then dissipated along the flow direction until it approaches T_{amb}, thus resulting in near zero thermal gradient for latter half of CHEX surface.

To understand the flow characteristics, 3D streamline distribution is also compared for all three ϕ_d as shown in Figure 6.12. For accurate comparison, the flow trajectories are evaluated at the exact coordinates which are equally spaced along axial and angular direction. In general, it is observed that near the entry and exit of the HHEX, all three volume fractions exhibit major flow recirculation. Such local recirculation zones occur due to the presence of axial Kelvin Force Density owing to the presence of non-uniform H gradient at both ends (refer Figure 6.4b). These volumetric forces then stimulate the disturbances within the MCS which lead to the aforementioned vortices. Moreover, strength of these recirculation zones grows proportionally as the KFD ($\mu_o\,(\mathbf{M}\cdot\nabla)\,\mathbf{H}$) depends on magnetization of MCS that increases with ϕ_d.

6.3.2 Multi-Stage Arrangement

Based on the obtained results, it is noticed that even for the largest ϕ_d of 40%, the obtained temperature drop corresponds to $\approx$ 1.9K at 1.03 Tesla as shown in Figure 6.9c. Such small temperature drop is appreciated considering the operation of single stage arrangement without any mechanical energy input. However, to make the current prototype more compatible, it is essential to expand its existing functional T span. Thus, two distinct multi-stage cooling arrangements (Figure 6.15 and Figure

6.18) have been explored such that the overall temperature span of the cooling system can be further increased. The considered configurations operate essentially on the cascading principle where the CHEX of one stage is coupled with the HHEX of the next stage via an Intermediate Heat EXchanger (IHEX).

To effectively implement the cascading principle, an indirect contact type recuperative HEX is chosen that allows the heat exchange between simultaneous flow streams through an intermediate medium. Additionally, for its efficient operation, the flow direction in each subsequent HEX is opposite to its counterpart from the previous stage. Moreover, a rectangular cross section is considered for both multi-stage arrangements as it offers the maximum surface area for a fixed enclosed volume. To be specific, a one inch wide and a half inch high rectangular duct is simulated as this configurations is also easily available for experimental replication. Furthermore, similar to single stage, the working fluid in each loop of both multi-stage arrangements is a mixture of 40 % Calorivac-H and Galinstan. Based on the preliminary calculations of T_{ad}[II] and overall energy balance between MCM and MCS, various possible multi-stage arrangements have been explored. After careful comparison among all configurations, a constant temperature drop of 0.8K ($T_{\mathrm{HHEX}} - T_{\mathrm{CHEX}} = 0.8$) is considered at each stage for safe operation[III]. To reduce overall computational efforts, the results for both cascade prototypes are obtained using a single phase steady state Newtonian solver. All flow variables are investigated for both multi-stage prototypes however, for the sake of brevity, only temperature distribution is discussed in the subsequent sections.

[II] The variation of T_{ad} with T_{ini} for Calorivac-H is obtained from the manufacturers datasheet [199].

[III] Based on the T_{ad}, the min/max of MCS within each stage can be determined. This is then further used to estimate a T_{CHEX} such that $T_{\mathrm{MCS}} < T_{\mathrm{CHEX}}$ is always maintained for cooling.

6.3.3 Planar Halbach Array and Magnetic Shielding

As mentioned earlier, for expanding the T span via recuperative HEX both flow streams must have indirect physical contact through an intermediate wall. However, the existing Halbach arrangement (shown in Figure 6.5a) offers a hindrance to this approach as it encloses the HHEX surface from all directions. Thus, distinct Halbach arrays are considered for both multi-stage arrangements where several permanent magnets are arranged on the same plane. Each consecutive magnet in this arrangement is $\pi/2$ out of phase with its surrounding neighbours. This allows to have a strong one sided flux distribution as shown in Figure 6.13. Such an arrangement ideally provides twice the magnetic field of a conventional magnet while also minimizing the undesirable influence of stray magnetic fields on the opposite side.

Moreover, while operating the cascade arrangement it is crucial to minimise the influence of $\mathbf{B}$ on CHEX. This is necessary as any exposure of magnetic field will

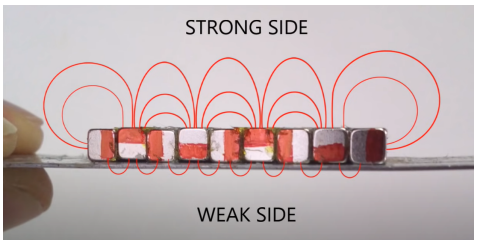

Figure 6.13: Visualisation of the planar Halbach arrangement. Here, the red and silver colour on the magnet represents the north pole and south pole respectively (From [200])

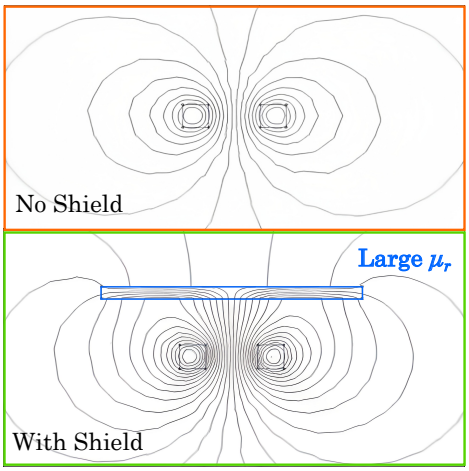

Figure 6.14: Illustration of the magnetic shielding principal

Table 6.4: Comparison of different materials for IHEX

Material [-]	κ[W/mK]	μ_r [-]	IHEX Thickness[I] [m]	Bi [-]
Copper	398	0.999994	9.9035	0.23979
Aluminium	247	1.000022	9.9032	0.41785
Nickel	90	600	16.505×10^{-3}	0.001018
Low Carbon Steel	54	1800	5.501×10^{-3}	0.001833

[I] The thickness of IHEX is determined based on the magnetic shielding correlation $B_x = B_{ref} \times exp(-\mu_r x)$.

result in an undesirable T rise of MCS. Thus, it is essential to isolate the CHEX of each consecutive stage from the strong magnetic field of previous stage. To summarize, a two-fold solution is needed in cascading arrangement that essentially allows for effective heat transfer along with the magnetic separation between HEX's. To achieve this through recuperative IHEX, the desired material should have higher thermal conductivity and large magnetic permeability. The κ is aimed at the heat transfer rate, whereas large μ_r offers the magnetic flux lines a path of least resistance. Hence, the flux lines obey the solenoidal field ($\nabla \cdot \mathbf{B} = 0$) without penetrating beyond the large μ_r material as shown in Figure 6.14. This effect of passively protecting the domain of interest through bypassing the magnetic flux lines is known as magnetic shielding[IV]. To successfully achieve the aforementioned binary purpose (higher κ and larger μ_r), different potential materials are compared as shown in Table 6.4. Based on the shielding factor calculations, it is noticed that IHEX made of low carbon steel can be a suitable choice for the present objective. Additionally, the T distribution within the IHEX is assumed to be uniform (lumped system analysis [201]) as the $Bi << 0.1$, and hence is not simulated for both multi-stage arrangements.

[IV] For effective magnetic shielding, there exist peculiar materials termed as Mu-metals that have μ_r in the range of 80,000 - 100,000. However, due to their low saturation density ($\approx$ 8000 Gauss), Mu-metals are not suitable for the current objective.

6.3.4 U Shape Staircase Arrangement

In continuation with the previously discussed structure (shown in Figure 6.3), a 3D U shaped domain with rectangular cross section is considered for a single stage. All individual components and their relative placement are shown in Figure 6.15a along

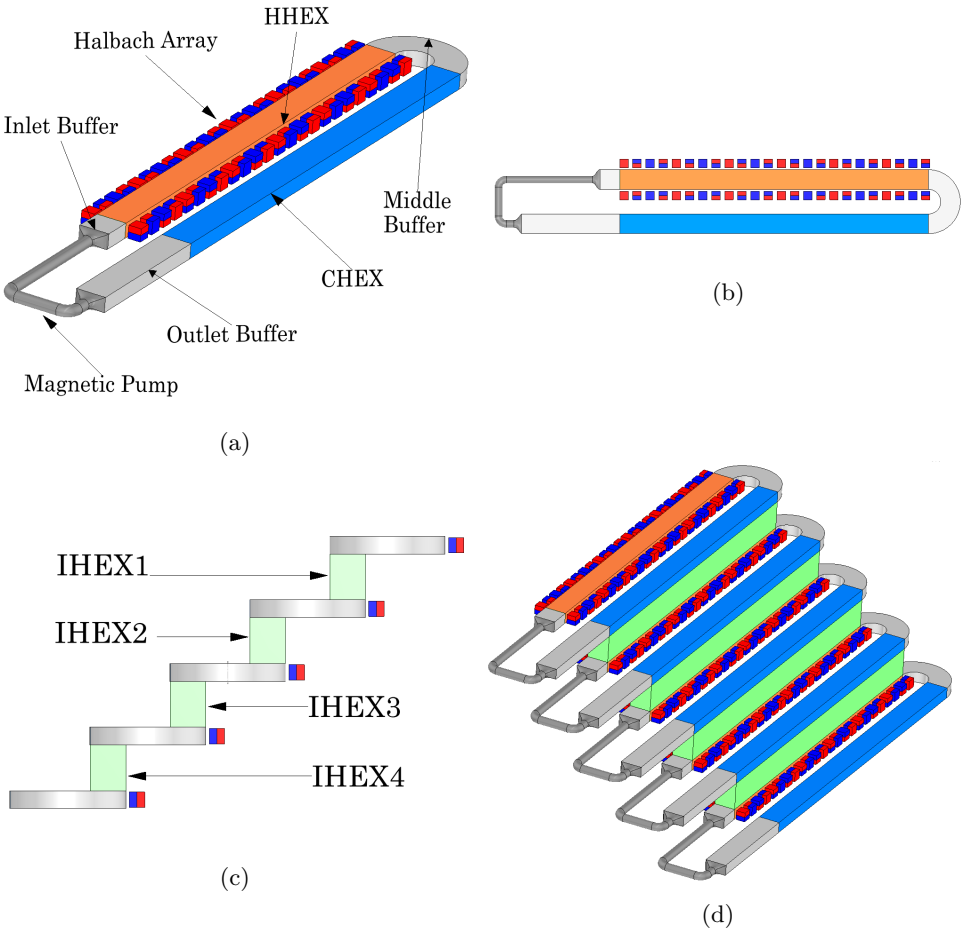

Figure 6.15: Schematic of the (a) Isometric view for a single stage configuration, (b) Top view for a single stage system, (c) Side view for the entire cascade system, (d) Isometric view for complete multi-stage staircase arrangement. Here, red and dark blue colour in the Halbach array represents the north pole and south pole respectively

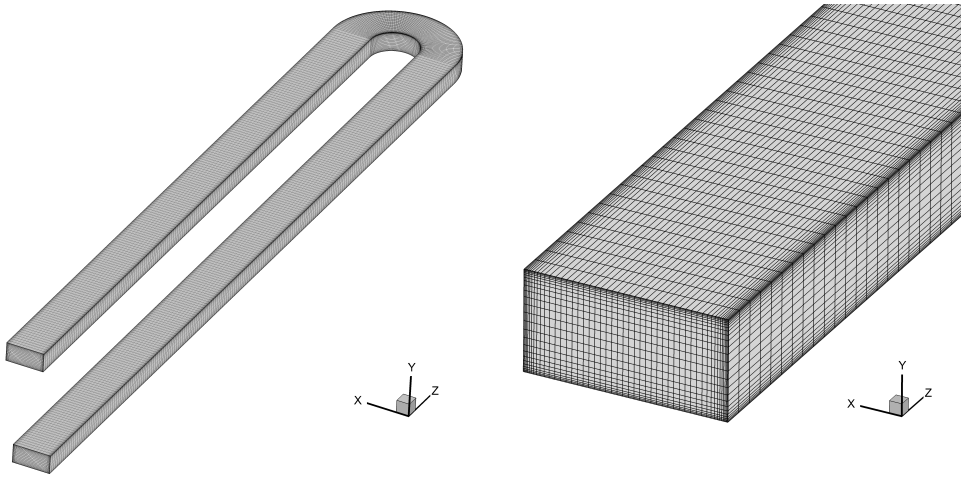

(a) (b)

Figure 6.16: Grid distribution for a U shape cascade arrangement; (a) Isometric view, (b) Enlarged view

with a magnetic pump[V]. The magnetic pump is aimed to recirculate MCS within the loop to ensure continuous operation of each stage. The length of both HEX and middle buffer length is considered identical as discussed in the Sub-section 6.1.1. Based on the primary results obtained, a one inch long inlet buffer and a five inch long outlet buffer is provided for each stage.

In accordance with cascading principal, the CHEX of each stage is coupled with HHEX of next stage through an IHEX. This criteria result in a peculiar staircase structure as shown in the Figure 6.15c, where each stage is at offset from its neighbours in both horizontal and vertical plane.

To simulate the multi-stage arrangement, a structured and non-uniform hexahedral grid distribution is used as shown in Figure 6.16a. Additionally, extra refinement is provided in the middle buffer region to capture the flow variation due to curvature.

[V] For representational purposes, the magnetic pump is drawn in a same horizontal plane. In an actual scenario, a bend in the vertical plane is required to push MCS as discussed in Rajamani [19].

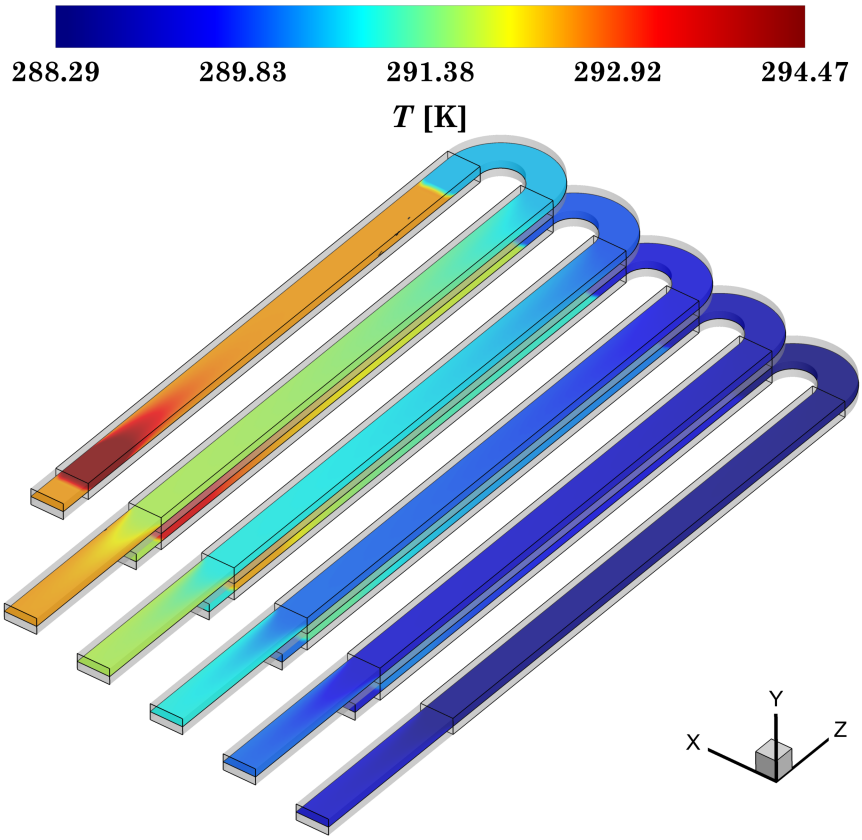

Figure 6.17: Temperature distribution along the axial mid-plane of each stage for a U shape based multi-stage cascade arrangement

6

For realising the large gradient of field variables, a local refinement is also provided near all bounding walls as shown in Figure 6.16b. To analyse the capabilities of such multistage configuration, the T contours along the axial mid-plane for each stage is observed as shown in Figure 6.17. It is noticed that a temperature span of 6.08K can be obtained for a 40% mixture of Calorivac – H and Galinstan at 1.03 Tesla using a five-stage cascade arrangement.

6.3.5 Vertically Stacked Circular Arrangement

Aforementioned U shape cascade arrangement requires large space in both vertical and horizontal plane leading to an overall bulky setup. Thus, to achieve a similar

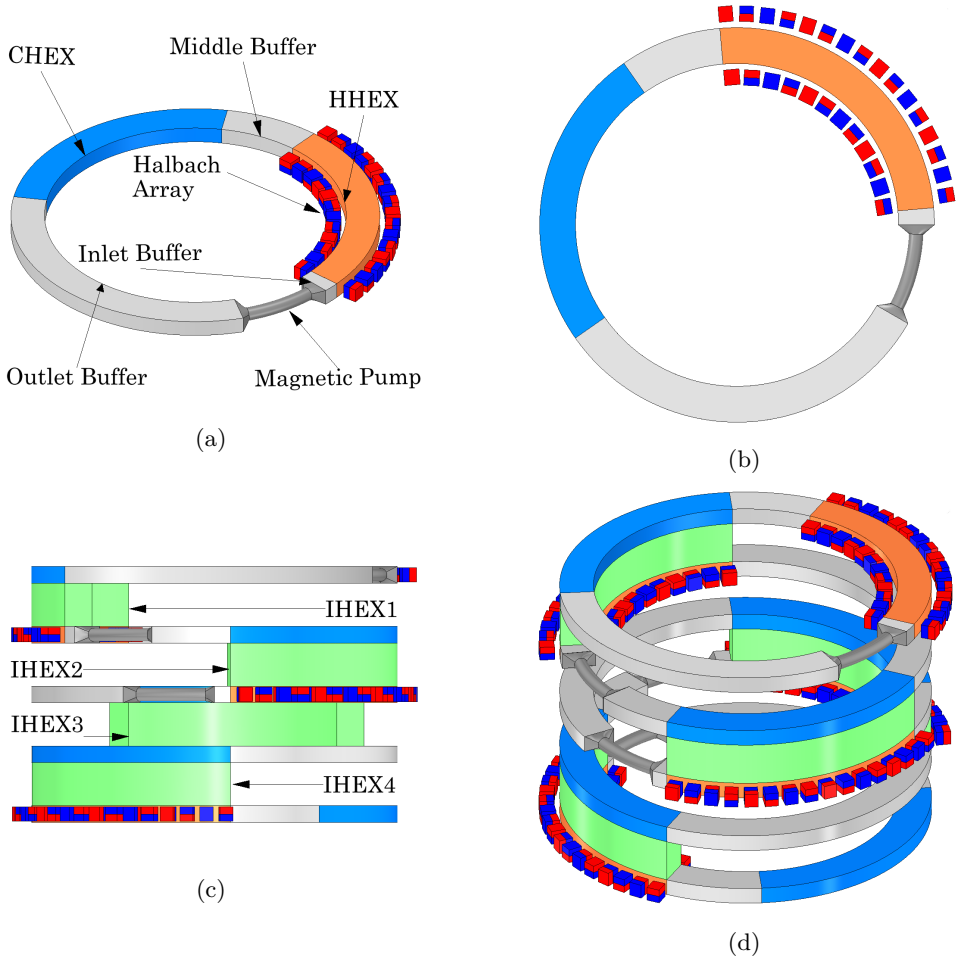

Figure 6.18: Schematic of (a) Isometric view for a single stage circular setup, (b) Top view for a single stage configuration, (c) Side view of the entire cascade assembly, (d) Isometric view for a five-stage vertically stacked configuration. Here, red and dark blue colour in the Halbach array represents the north pole and south pole respectively

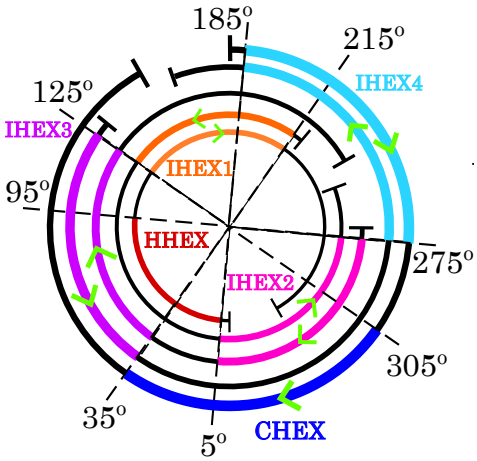

Figure 6.19: Angular placement of all HEX for the entire cascade configuration. Here, the innermost circular arc refers to the first stage, and subsequent stages are shown with different radii solely for illustrative purposes

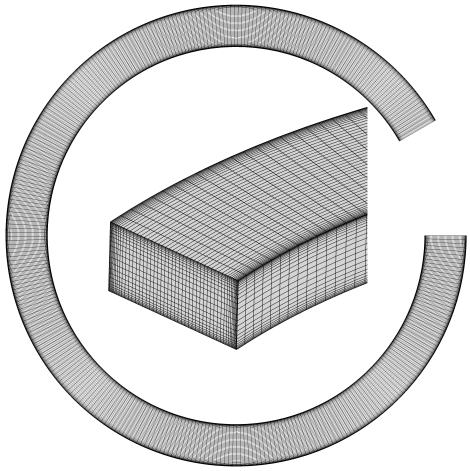

Figure 6.20: Schematic of the grid distribution for a vertically stacked circular cascade arrangement

T span with a more compact cascading setup, a vertically stacked circular system has been investigated as shown in Figure 6.18. A circular duct having exactly alike rectangular cross-section (one inch wide and a half inch high) is considered for each stage as displayed in Figure 6.18a. After several comparisons, an annular section of 330° with a major radius of 5 inch is finalised for each stage[VI]. The additional 30 degree section is intended to implement the magnetic pump assembly. Moreover, within each stage, both HEX correspond to the radial arc length of 90°. In alignment with the axial dimension requirement of Sub-section 6.3.4, radial arc length corresponding to 5° and 25° is provided for inlet buffer and outlet buffer respectively. On similar basis, both HEX are separated with a middle buffer of 30°

[VI] Different combinations of major radius (R_{maj}) and the angular section (θ) can be used to obtain radial arc length (L_{radial}) that is equal to the total axial length of U shape arrangement, where $L_{radial} = \theta/360 \times 2\pi R_{maj}$

arc length for adiabatic demagnetization.

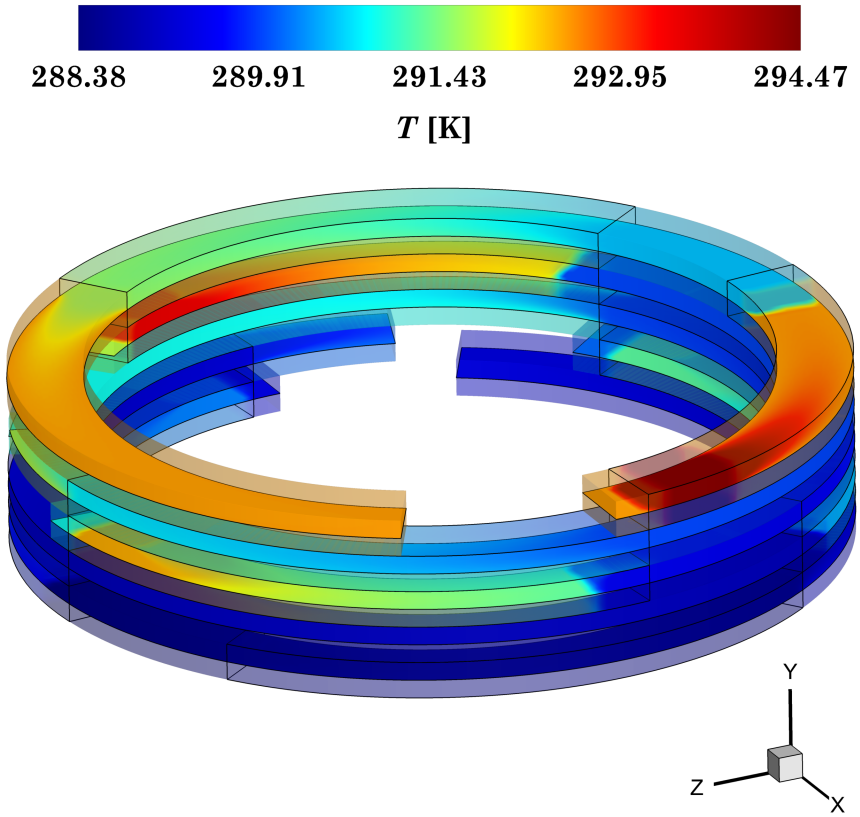

Figure 6.21: Temperature distribution along the axial mid-plane of each stage for a vertically stacked circular cascade arrangement

Owing to the cascading criteria, a vertically stacked arrangement is obtained as displayed in Figure 6.18d, where each stage has a different location for inlet and outlet. The precise angular positioning of all stages with respect to a common origin is shown in Figure 6.19. Due to the same cross-section, an exactly similar grid distribution is used for the simulations of vertically stacked arrangement as shown in 6.20. Moreover, in alignment with U shaped staircase arrangement, the heat

distribution for the entire system is observed by comparing the axial mid-plane T contours. It can be confirmed from Figure 6.21 that a similar temperature drop of 6.08K can be obtained with the help of this compact vertically staggered circular setup.

CHAPTER 7

Conclusions and Outlook

The present numerical work is a sincere effort toward developing a novel MCE based room temperature cooling device that operates without any mechanical motion. The current research offers better insights into the design and functioning of such a setup, as well as its potential challenges. The major outcomes of the present work are discussed below, along with a few suggestions for further research.

7.1 Concluding Remarks

In the beginning, considerable efforts are put to comprehend the magnetic field distribution, as it is the core driving element for all the volumetric forces desired in the present context. To do so, different solvers are developed in the OpenFOAM framework for computing complete 3D field distributions of magnetic dipole, permanent magnet, and DC solenoid. All the solvers are thoroughly validated with the

experimental/analytical results to authenticate their accuracy. It is observed that for maximum cooling, the permanent magnet is more convenient than electromagnet and it must be positioned as near as possible to the MCS. However, for efficient magnetic pumping, there exists an optimal spacing between the coil winding and the pipe surface. This is mainly as the distant solenoid winding cannot generate sufficient magnetic field gradient in axial direction to pump MCS, whereas closely attached coils result in large undesired magnetic field gradient in radial direction near both solenoid ends as shown in Figure 2.14.

Additionally, to capture the magnetic response of MCS, different magnetization models are compared in detail along with relaxation mechanisms. Further, temperature and magnetic field dependent experimentally measured data is used to compute the ΔT_{ad} of MCS. This has helped to avoid discrepancies associated with the results from the MFT. Moreover, an effective Herschel-Bulkley model is used to obtain the rheology of present MCS that also incorporates the magneto-viscous effect. For thermal properties, Rayleigh's correlation is used for κ, whereas experimentally measured T dependent data is used for specific heat. Based on Gillies stability criteria, the CDV is finalised, which is then used as a threshold value to avoid the settling of MCM particles.

After discussing briefly about different solid-liquid modelling approaches, an Euler-Euler based framework is finalised for the present work. To be specific, three different mixture models are considered and finally the governing equations for the Diffusion Mixture Models are derived. Inclusion of the source terms for both momentum equation and energy equation are justified which originates from the interaction of magnetic fluids and magnetic field. Moreover, a preliminary DEM work is performed to initiate the larger context of micro-macro coupling. It is observed that the dynamics of an individual Calorivac particle vary significantly in each direction according to $\mathbf{H}$ distribution.

The hydro-thermal response of magnetic fluids is studied initially in two distinct physical configurations using different sources of magnetic fields. For a differentially

heated semi-circular domain, it is noticed that the magnetic dipole stimulates the formation of flow vortices that significantly alter the overall flow behaviour. Such modifications are found to be highly dependent on the dipole location and its magnitude. As a result of this, the magnitudes of both Nu_{avg} and U_{Mean} increases with Mn and their highest values are observed for topmost and bottommost dipole location, respectively. Additionally, the presence of localised peaks is noticed in the Nu_{local} distribution corresponding to its dipole location. On the other hand, the heat transport process within a circular annulus is replicated using a magneto-caloric nanofluid and permanent magnet. Results show a periodic fluid rotation in a clockwise direction for all cases and highest frequency of this rotation corresponds to the smallest L/D and maximum Br. Nu_{avg} shows improved values for higher strength of the applied field and larger span between the annulus. It is also found that, for a specific L/D ratio, the flow velocity increases with intensity of the applied magnetic field whereas at a particular Br, it decreases with an increase in span-wise width.

Finally, a novel Diffusion Mixture solver is devised in the OpenFOAM framework to simulate the MCE based cooling systems. At first, the performance of a single stage setup is investigated with the help of several local and global field variables. To authenticate the numerical results, a detailed grid independence analysis is performed along with a validation study. It is concluded that ΔT_{ad} and the cooling capacity of single stage system is proportional to the amount of MCM used. For a MCS of 40% Calorivac-H and Galinstan, a temperature drop of 1.9K is obtained using 1.03 Tesla. Later, two different multi-stage prototypes are studied that function on a cascading principle to further expand this cooling span. Contrary to the enclosed Halbach structure of single stage arrangement, a planar Halbach array is used for cascading system. This is done to enable the physical contact between the HEX of subsequent stages. After comparing different potential materials, a magnetic shield cum HEX of low carbon steel is finalised to execute heat transfer while maintaining the magnetic isolation. For both multi-stage arrangements, a temperature drop of

6.08K is achieved with five stage cascading setup.

7.2 Recommendations

Although the present work provides considerable insights into the modelling of MCE based cooling devices, there still exists several aspects that can be further improved. Thus, following suggestions can be implemented in alignment with the current objective to better our understanding:

- **Modelling Framework** - The present work is based on the Euler-Euler approach and thus offers limited insights into the complete flow physics. For improved resolution of the entire system, a VOF-DEM approach should be implemented. The VOF method can capture the behaviour of continuous phases (air/Galinstan) in the context of magnetic pumping, whereas DEM is able to resolve the dispersed medium interactions. Although it is quite challenging to compute such a multi-scale problem considering non-Newtonian rheology and the presence of an external magnetic field. However, several existing frameworks, namely XDEM and LIGGGHTS, can be used as a first step for such a complex yet interesting journey.

- **Thermophysical Properties** - While solving the governing equations, effect of magnetic field is considered only for few thermophysical parameters i.e $\mathbf{M}$ and $(\partial\mathbf{M}/\partial T)_{\mathbf{H}}$. It would be valuable to include a similar experimental dataset for the magnetic field dependent variation of density and specific heat. In addition, although the magneto-viscous effect is taken into account, exact rheological measurements at different shear rates for the MCS should be used. This will ease the computational efforts required for stable implementation of the Herschel-Bulkley model in OpenFOAM. Further, the current thermal conductivity correlation only considers the effect of volume fraction. However, as highlighted in literature, the $\mathbf{H}$ dependent increment of κ is subjective

to particle size and volume fraction. Thus, a more comprehensive input for thermal conductivity can be included to achieve more accurate behaviour.

- **Treatment of MCM** - In the present work, all the Calorivac-H particles are assumed to be spherical and of a uniform diameter. Nonetheless, later, it is observed from the micro-CT measurements that MCS contains different non-spherical particles. Such non-uniform distribution reduces the overall viscosity and increases thermal conductivity, which needs to be addressed. Further, the particle-particle interaction is neglected in the present work as the inter-particle spacing is large for the current MCS (Equation C.4). Moreover, particle clustering is less likely to occur due to the large resistance offered by the highly viscous Galinstan. However, considering the large **H** magnitude, possibility of agglomerate formations and their influence on the overall system performance should be investigated.

- **Magnetic Assembly** - The design of the magnetic field source is a critical bottleneck for all MCE devices. Although, the planar Halbach array offers an assured solution for the current multi-stage arrangements. A detailed parametric study should be performed to optimise magnet dimensions that can further reduce the overall cost and bulkiness of the present setup.

- **Numerical Simulations** - Currently, only a single particle diameter is considered in all computational results of this thesis. Thus, influence of different MCM sizes on particle clustering and system performance needs to be addressed. Additionally, a thorough validation study should be carried out with actual experimental measurements of an MCS operated setup. This will help in improved system prediction by implementing a better-suited slip velocity model in the present numerical work. Further, possibility to employ different MCS in each stage with customised T_{Curie} can be explored. This will enable to obtain variable temperature drops across each stage of the cascading system.

APPENDIX A

Derivation of the MCE

The MCE discussed in Section 1.2 can be mathematically expressed in two different ways i.e. an isothermal entropy change or an adiabatic temperature change. In the present work, the adiabatic temperature change formulation is used to quantify the overall change in the energy conservation as shown in Equation 4.25.

For a thermodynamically open system (where MCM can cross across magnetic field boundaries), the change of specific entropy (ds) is represented as a dependent function of temperature and applied field as shown below

$$ds(T,H) = \left(\frac{\partial s}{\partial T}\right)_H dT \; + \; \left(\frac{\partial s}{\partial H}\right)_T dH \tag{A.1}$$

Based on the change of specific entropy from Equation A.1, the specific heat change

(dq) for a reversible process can be written as

$$dq = Tds = C_H\left(T,H\right)dT \;+\; C_T\left(T,H\right)dH \quad \text{where}$$
$$C_H = \left(\frac{\partial q}{\partial T}\right)_H = T\left(\frac{\partial s}{\partial T}\right)_H \text{ and } C_T = \left(\frac{\partial q}{\partial H}\right)_T = T\left(\frac{\partial s}{\partial H}\right)_T \tag{A.2}$$

Additionally, the Maxwell's relation for the corresponding variables can be written as [15]

$$\left(\frac{\partial s}{\partial H}\right)_T = \mu_o\left(\frac{\partial M}{\partial T}\right)_H \tag{A.3}$$

Furthermore, the entropy change for an isothermal process can be simplified as

$$ds(T,H) = \underbrace{\cancelto{0}{\left(\frac{\partial s}{\partial T}\right)_H dT}}_{\text{Isothermal process}} + \left(\frac{\partial s}{\partial H}\right)_T dH \tag{A.4}$$

After doing the equivalent substitution from Equation A.3, the isothermal entropy change of a Magneto-caloric process can be written as

$$\boxed{\textit{Isothermal entropy change} \longrightarrow \quad ds = \mu_o\left(\frac{\partial M}{\partial T}\right)_H dH} \tag{A.5}$$

The rise/drop of temperature due to a change in magnetic field is the obvious and noticeable characteristic of MCE. Owing to its adiabatic nature (where the change of entropy is zero i.e. $ds = 0$), Equation A.1 can be rewritten as

$$\underbrace{\left(\frac{\partial s}{\partial T}\right)_H dT = -\left(\frac{\partial s}{\partial H}\right)_T dH}_{\text{From Equation A.1}} \quad \text{where} \quad \underbrace{\left(\frac{\partial s}{\partial H}\right)_T dH = \mu_o\left(\frac{\partial M}{\partial T}\right)_H dH}_{\text{From Equation A.3}} \tag{A.6}$$

Since the heat change (dq) is also zero for an adiabatic process, the specific heat ratios can be correlated from Equation A.2 as

$$dT = \frac{-C_T\left(T,H\right)dH}{C_H\left(T,H\right)} \implies \frac{-1}{C_H\left(T,H\right)}\underbrace{\left[T\left(\frac{\partial s}{\partial H}\right)_T\right]}_{\text{From Equation A.2}} dH$$

$$dT = \frac{-T}{C_H\left(T,H\right)}\underbrace{\left[\mu_o\left(\frac{\partial M}{\partial T}\right)_H\right]}_{\text{From Equation A.3}} dH \tag{A.7}$$

A

Thus, the adiabatic temperature change for a Magneto-caloric process is determined as

$$\boxed{\textit{Adiabatic temperature change} \longrightarrow \quad dT = -\frac{\mu_o T}{C_H}\left(\frac{\partial M}{\partial T}\right)_H dH} \tag{A.8}$$

The aforementioned specific temperature change can be converted to the rate of energy change per unit volume solely because of MCE ($\dot{Q}_{\mathrm{MCE}} = C_{\mathrm{H}} \times dT$) as shown below [15]

$$\boxed{\dot{Q}_{\mathrm{MCE}} = -\mu_o T\left(\frac{\partial M}{\partial T}\right)_H \left(\frac{\partial \mathbf{H}}{\partial t} + (\mathbf{U}\cdot\nabla)\,\mathbf{H}\right)} \tag{A.9}$$

A

A

APPENDIX B

Magnetic Field Distribution of Finite Solenoid

The OpenFOAM environment does not have an inbuilt way to solve some of the advanced mathematical functions such as complete elliptic integrals, hypergeometric functions, and the Legendre polynomials etc. Thus, its equivalent formulations are solved in terms of the Bessel functions, to compute the magnetic field distributions. The distributions are defined for an azimuthally symmetric solenoid of length L_s and radius a $(D_s/2)$ which consists of N number of turns, and through which a fixed magnitude of current I flows continuously. Both the numerical computations (Figure 2.13) are carried out for an iron free, thin finite solenoid using cylindrical coordinates system (ρ, θ, z).

For MATLAB calculations, the field distributions (Equation B.1 - Equation B.5)

are provided using complete elliptic integrals based on the work done by Callaghan et al. [62] and Cebron [202] in which the radial magnetic field variation (B_ρ) is given as

$$B_\rho = -\frac{\mu_0 N I}{\pi}\sqrt{\frac{a}{\rho}}\left[\frac{2-\omega^2}{2\omega}K(\omega) - \frac{E(\omega)}{\omega}\right]_{\omega_-}^{\omega_+} \tag{B.1}$$

Here, K and E refer to the complete elliptic integral of the first kind and second kind respectively, where,

$$\omega_\pm = \sqrt{\frac{4a\rho}{(a+\rho)^2+\lambda_\pm^2}} \quad \text{and} \quad \lambda_\pm = z \pm L_s/2 \tag{B.2}$$

Whereas, the axial magnetic field (B_z) is defined based on the maximum value of a non - dimensional parameter (ζ_+), which is described for a combination of radial as well as axial location.

For $\zeta_+ < 1$,

$$B_z = \frac{\mu_0 N I}{\pi}\frac{a}{(a+\rho)}\frac{1}{(\gamma+1)}\left[\chi_\pm\left(K\left(\sqrt{1-\zeta_\pm^2}\right)\right]_-^+ + \frac{\mu_0 N I}{\pi}\frac{a}{(a+\rho)}\frac{1}{(\gamma+1)}\left[\gamma\,\Pi\left(1-\gamma^2, \sqrt{1-\zeta_\pm^2}\right)\right]_-^+ \tag{B.3}$$

For $\zeta_+ \geq 1 org$,

$$B_z = \frac{\mu_0 N I}{\pi}\frac{a}{(a+\rho)}\frac{1}{\gamma(\gamma+1)}\left[\frac{\chi_\pm}{\zeta_\pm}\,\gamma\,K\left(\sqrt{1-\frac{1}{\zeta_\pm^2}}\right)\right]_-^+ + \frac{\mu_0 N I}{\pi}\frac{a}{(a+\rho)}\frac{1}{\gamma(\gamma+1)}\left[\frac{\chi_\pm}{\zeta_\pm}\,\Pi\left(1-\frac{1}{\gamma^2}, \sqrt{1-\frac{1}{\zeta_\pm^2}}\right)\right]_-^+ \tag{B.4}$$

In addition to the previously defined parameters, Π is the complete elliptic integral of the third kind, and

$$\gamma = \frac{(a-\rho)}{(a+\rho)}\ , \quad \chi_\pm = \frac{\lambda_\pm}{\sqrt{(a+\rho)^2+\lambda_\pm^2}}\ , \quad \text{and} \quad \zeta_\pm = \sqrt{\frac{(a-\rho)^2+\lambda_\pm^2}{(a+\rho)^2+\lambda_\pm^2}} \tag{B.5}$$

For OpenFOAM computations, both the radial and the axial field variations of a solenoid are solved in terms of the Bessel functions [61,67] as shown in Equation B.6 - Equation B.8 .

$$B_\rho = -\frac{\mu_0 D_s N I}{4L_s} \int_0^\infty dk \frac{1}{k} \frac{df(k;z)}{dz} J_1(k\rho) J_1(ka) \tag{B.6}$$

$$B_z = \frac{\mu_0 D_s N I}{4L_s} \int_0^\infty dk f(k;z) J_0(k\rho) J_1(ka) \tag{B.7}$$

where $f(k;z)$ is defined as a piece-wise function for different values of z,

$$f(k;z) = \begin{cases} e^{-k(z-L_s)} - e^{-kz}, & z \geq L_s \\ 2 - e^{-k(L_s-z)} - e^{-kz}, & 0 \leq z < L_s \end{cases} \tag{B.8}$$

Here, J_n for n $\geq$ 0 is the Bessel functions of the first kind.

Finally, to compare the precision of the Bessel function calculations in the OpenFOAM framework, the obtained field distributions are compared against the inaugural work of Callaghan et al. [62] (using complete elliptic integral formulations in MATLAB) as shown in Figure 2.13.

B

B

APPENDIX C

Diffusion Mixture Model

C.1 Validity of DMM

The Euler-Euler based mixture model approach can be only applied to certain multi-phase flow configurations. One of the major constraints required for its legitimacy is the existence of local equilibrium over the short spatial length scale. This simply means that dispersed phase must closely follow the continuous phase in its immediate vicinity. Due to this criteria, the behaviour of solid-liquid systems can be more accurately computed than gas-liquid systems using mixture models [145].

The aforesaid qualitative criteria can be converted to a quantitative correlation which implies that the characteristic length scale of particle (l_{sp}) must be always smaller than the system length scale ($l_{sp} << D_h$) [171]. Further, the l_{sp} is defined as the distance travelled by the particle at terminal velocity (U_t) within its relaxation

Table C.1: Magnitude of required parameters

Symbol	Description	Value	Units
$\phi_{d,max}$	Maximum Volume fraction	0.4	-
D_h	Hydraulic diameter of the domain	0.02	m
d_p	Particle diameter	50×10^{-6}	m
μ_c	Dynamic viscosity of Galinstan	2.4×10^{-3}	kg/m.s
Eu	Euler's number	2.71828	-
ρ_d	Density of dispersed phase	7200	kg/m^3
ρ_c	Density of continuous phase	6440	kg/m^3

time (t_p) as shown below[I]

$$l_{sp} = \frac{t_p U_t}{Eu} \quad \text{where} \quad t_p = \frac{\rho_d d_p^2}{18\mu_m} \quad \text{and} \quad U_t = \frac{(\rho_d - \rho_c)\, d_p^2 g}{18\mu_c} \tag{C.1}$$

However, as suggested by the Manninen et al. [145], the true/corrected length scale of particle (l'_{sp}) can be one order of magnitude larger than l_{sp}. Hence, to examine the validity of DMM, l'_{sp} is used in the present work to ensure $l'_{sp} << D_h$. The assessment is done for the worst case scenario so that the criteria is safely fulfilled for the normal operational range. To do so, the highest ϕ_d (based on C.4) and the largest d_p are considered. After substituting the corresponding values from Table C.1, the magnitude of l_{sp} is computed using Equation C.1 as shown below

$$U_t = \frac{(7200 - 6440) \times (50 \times 10^{-6})^2 \times 9.81}{18 \times 2.4 \times 10^{-3}} \longrightarrow 4.3143 \times 10^{-4}\,\mathrm{m\,s^{-1}}$$

$$t_p = \frac{7200 \times (50 \times 10^{-6})^2}{18 \times 0.0136} \longrightarrow 7.3125 \times 10^{-5}\mathrm{s} \tag{C.2}$$

$$\text{thus} \quad l_{sp} = \frac{4.3143 \times 10^{-4} \times 7.3125 \times 10^{-5}}{2.71828} \longrightarrow 1.1605 \times 10^{-8}\mathrm{m}$$

[I] Here, the mixture viscosity is computed based on the Thomas' correlation mentioned in Equation 3.7.

Now, following the Manninen's criteria, the l'_{sp} is 1.1605×10^{-8}m, which is six orders of magnitude smaller than the $D_h(2 \times 10^{-2}\text{m})$. Thus, it can be evidently said that the fundamental requirement of the local equilibrium ($l'_{sp} << D_h$) is always justified for the present multiphase system.

C.2 Limitations of DMM

As discussed in Section 4.4, the current DMM formulations are derived based on two way coupling between the dispersed phase and its carrier phase. However, such a formulation is not universally valid as at higher ϕ_d, the suspended particles affect its surrounding neighbourhood and these interaction becomes too significant to be neglected. Hence, there exists a constraint for the maximum allowable volume fraction ($\phi_{d,max}$) within which the current DMM can provide accurate results. The magnitude of $\phi_{d,max}$ varies for each multiphase system based on the specific thermo-physical properties of its dispersed and continuous phase.

The inter-particle spacing (L_d) among the dispersed phase of specific d_p having a known ϕ_d can be computed using the work of Crowe et al. [203] as shown below

$$\frac{L_d}{d_p} = \left[\left(\frac{\pi}{6}\right)\left(\frac{1+\varpi}{\varpi}\right)\right]^{\frac{1}{3}} \quad \text{where} \quad \varpi = \frac{\Upsilon}{\gamma} = \frac{\phi_d}{\phi_c}, \quad \Upsilon = \frac{\phi_d \rho_d}{\phi_c \rho_c}, \quad \text{and} \quad \gamma = \frac{\rho_d}{\rho_c} \tag{C.3}$$

Further, for similar intermediate particulate loading (Υ), Nayak et al. [149] suggested the limiting magnitude of $L_d/d_p = 1.093$ to implement two way coupling. Based on this, the $\phi_{d,max}$ can be computed as shown below

$$\left(\frac{L_d}{d_p}\right)_{limit} = 1.093 \quad \Longrightarrow \quad \underbrace{\left[\left(\frac{\pi}{6}\right)\left(\frac{1+\varpi}{\varpi}\right)\right] = (1.093)^3}_{\text{Equating RHS of Equation C.3}} \tag{C.4}$$

$$\underbrace{\left[\left(\frac{\pi}{6}\right)\left(\frac{1}{\phi_{d,max}}\right)\right]}_{\text{Substitute } \varpi \text{ from Equation C.3}} = 1.30575 \quad \Longrightarrow \quad \phi_{d,max} = 0.4009$$

Thus, for the considered multiphase system, the current (two-way coupled) DMM formulations can provide accurate results only till ϕ_d of 40%. For $\phi_d > \phi_{d,max}$, additional modifications should be made that incorporate the particle-particle interactions of the dispersed phase.

Scientific Output

List of Journal Publications

- Shubham Dalvi, ECJ Karaliolios, Theo H van der Meer, Mina Shahi, *"Thermo-magnetic convection in a circular annulus filled with the magnetocaloric nanofluid"*, International Communications in Heat and Mass Transfer, Jul 2020
- Shubham Dalvi, Theo H van der Meer, Mina Shahi, *"Hydro-thermal interactions of a ferrofluid in a non-uniform magnetic field"*, Heat and Mass Transfer, Aug 2022
- Shubham Dalvi, Theo H van der Meer, Mina Shahi, *"Numerical evaluation of the ferrofluid behaviour under the influence of three-dimensional non-uniform magnetic field"*, International Journal of Heat and Fluid Flow, Apr 2022
- Shubham Dalvi, Keerthivasan Rajamani, Theo H van der Meer, Mina Shahi, *"Thermo-hydraulic assessment of a MagnetoCalorics based room temperature cooling system"*, International Journal of Multiphase Flow, To be submitted

List of Conference Contributions

❖ Poster Presentation

- *"Numerical Analysis of Magneto-Caloric Effect within a Circular Annulus"*, Delft Days on Magneto Calorics (DDMC), TU Delft, The Netherlands, November 18-19, 2019

❖ Oral Presentations

- *"Numerical Investigation of Ferrofluid and its Magnetization behaviour"*, Thermag IX 2021 - 9th IIR International Conference on Caloric Cooling and Applications of Caloric Materials, University of Maryland, USA, June 7-11, 2021 (virtual)

- *"Modelling Thermo - Hydraulic Characteristics of a Magneto – Caloric Slurry"*, Eurotherm 2021 - Caloric Heating and Cooling Seminar, University of Twente, The Netherlands, July 13-15, 2021 (virtual)
- *"Investigating the Effects of a Non - Uniform Magnetic Field on Heat and Flow Characteristics of a Ferrofluid"*, 8th European Thermal Sciences Conference, Lisbon, Portugal, September 20-23, 2021 (virtual)

❖ Invited Talk

- *"Understanding a FerroHydroDynamics solver in OpenFOAM"*, OpenFOAM Workshop - TU Delft Institute for Computational Science and Engineering (DCSE), TU Delft, The Netherlands, July 8, 2022

Acknowledgements

"*If you enjoy being on a roller coaster ride, you should definitely try out finishing a PhD*". This one-liner of mine might not earn claps, but it is an undeniably accurate description of my last four and a half years. However, it was these highs and lows that led to this adventurous journey worthy of reaching this milestone. Besides the circumstances, I'm truly grateful for all the individuals and would like to acknowledge them for their direct/indirect help that led to my personal as well as professional growth.

First, I would like to thank my daily supervisor and promoters for giving me the opportunity to work on this research venture. All three of you were there during the initial interview, when the idea of contributing to this project felt like a distant dream to me. **Mina**, thank you so much for giving me the freedom to wander around in different research directions, while at the same time getting me back on track whenever I was lost. You are a great team leader, someone who knows how to manage people and get the work done in an efficient manner. During these years, your mantra of "*Don't just teach them, but also try to educate them*" has considerably enhanced my presentation skills. **Theo**, you are very open-minded person and your enthusiasm for trying out new challenging things, like learning French, is truly inspiring. Your feedback during our progress meetings was always to the point and has helped me improve my work. It's fun every time to interact with you, as your diverse range of experiences across countries/cultures brings a unique depth to all

conversations. Thank you **Gerrit** for always encouraging us to focus on the bigger picture/ultimate goals of our research, or as you usually say "*the helicopter view*". Your praise has always meant a lot to me. Be it for my first TE presentation or the farewell speech at Keerthi's defense dinner, you are always generous to really appreciate and support your students.

I would also like to thank all the committee members **Prof. Dr. Bernhard Peters**, **Prof. Dr. Ekkes Brück**, **Prof. Dr. Ir. Bernard Geurts**, **Prof. Dr. Ir. Wilko Rohlfs**, and **Prof. Dr. Ir. Harm Askes** for their feedback, which eventually helped to further improve this thesis.

During these years, there were several administrative tasks that just could not be completed without the support of wonderful people we have in our group. **Sally**, **Sylvia**, **Susan**, and **Henk-Jan** thanks a lot for responding to my queries and arranging everything within due time. **Wouter**, I can't appreciate you enough for responding to my naive cluster related queries/requests. You were always so kind to help and every time I learned something new from your feedback. I also want to acknowledge the support of **Martin** who efficiently carry forwarded this legacy in the later phase of my research.

I would like to thank **Amir** for giving me the opportunity to be a teaching assistant in the Transport Phenomenon course. Working with you and experiencing your unique sense of humour was a valuable learning experience for me. I also extend my gratitude to **Khurram Bhai** for always being there to help me with the XDEM framework. I would also like to thank **Aastha** for spending hours discussing the DEM fundamentals, and I really appreciate your patience in answering my novice questions. **Keerthi**, You are a person with so few vices, which frequently creates the false impression that you are too good to be true. Right from the start, you've consistently been there to patiently answer all my naive, sometimes foolish, and occasionally irritating questions. It was a great experience to work with you, and I wish you good luck as you continue your future path of research in TE.

Despite being away from home, I was lucky to be surrounded by a group of

individuals who made Enschede inhabitable for me. Thank you **Harsha Bhai** for everything. You are with me since the first day of this PhD, and have supported me through all the joys and sorrows of my time at UT. From the countless chai sessions to our endless political discussions, your advise of *learn to respect every individual's journey* has surely helped me grow. **Balan**, many thanks for organising all those sports activities and our memorable trips to Iceland, Italy, and Poland. I do miss our fun Friday hangouts where we used to play poker/play station and complain how difficult our PhD is :-). **Timm**, you are a humble person, a hard-working fellow, and a great bluff master when it comes to poker :-). *There's nothing that a little bit of positivity and planning can't overcome.* This message from you during one of our conversations is something that you truly live by. Besides multiple visits to Belgium and Germany, our road trip to Paris with Edmond is going to be etched in my memory forever. Many thanks to **Edmond**, for resonating with my sense of humour and laughing at my weird jokes. You always reminded me that *sometimes it's okay to be not okay* and *balance is an essential key to growth.* I really wish more people could experience how creative and witty your imagination can be.

Umair, you will always be my Bhaijaan !! Someone who shares the same taste and respect not just for the music but also for lyrics. We've several amazing memories together, and I'm going to miss our office gupshups quite a lot. Many thanks to **Laila** for inviting me on several occasions and bringing back memories of home with her delicious food. **Sathya** you are one brave soul. It takes enormous courage to speak our brains out and be as transparent as you are. **Jie Wang**, I always look up to you as someone who has mastered the concept of work life balance. Thank you for all the wonderful memories we shared, whether it was over our office-brewed coffee, the hotpot, or the Antwerp pub-crawl. Thank you **Yan** for all the heartfelt conversations and for being such a great officemate. You were always so supportive of me and would consistently encourage me to excel in everything I did. **Mohammad**, you are an inspiring researcher. The small pep talks with you have always helped me to further push myself. I just wish I could've defeated you a few more times in our

poker games to settle our final score :-). **Sara** you are one of the humblest people I've met so far. A lot to learn from you on that front.

Marijn, I admire you for being diligent and methodical when it comes to the quality of the research. We share several fun memories from our old office, and I want to give you a special thanks for helping me with the samenvetting of this thesis. Thank you **Sara** for those gifts from your home-town and for your helpful words. I still remember the advise you gave me during one of our conversations: *You just need to convince one person and make sure that is you.* **Alireza**, thank you for organising all those large gatherings at your mansion. You made sure to inform us of everything about anything that's in the current news. Thank you **Citra** for always being so cheerful and spreading your positive vibes. **Michael**, I always remember you for your consistent punctuality, and many thanks for introducing me to *Tompouce*. Special thanks to **Yousef** for all those memorable poker games and spreading happiness with his humble smile. Thank you **Juan** for showing how sincerely we all should work during our office hours :-). Thanks to **Sriram** for all the chess games and off course for the gossips. During this time, many new candidates joined our research group. I also want to appreciate them and wish them great success in their respective projects.

Thanks a lot **Yash Bhai** for your invaluable support during my initial days in Enschede. Without your help, it would have been too difficult to become familiar with everything. Many thanks to **Saurabh** for his company during these years and for the several great memories we shared together over badminton/cricket. You would always spread your infectious enthusiasm during our conversations and keep insisting: *Baba, tum apne aap ko thoda free karo yaar* :-). **Bharath**, you are a true wanderluster who knows how to appreciate his friends and the memories shared with them. Thank you for all the amazing time we spent together and for those healthy discussions over several different topics. Many thanks to **Bala** for being such a fun guy to hang around with and for the many great moments we shared. I would also like to appreciate **Halvor**, **Julian**, and **Katerina** for their company and sharing

special moments with me over the years.

I was fortunate to have a strong remote support system whose guidance and encouragement have helped me through the thick and thin of my PhD. Thank you **Shwetank** for always being there to give me a reality check. I admire you for your constant support as well as your blunt criticism. **Tusha**, you are one strong rebellious girl who has repeatedly shown me how important it is to be brave and embrace our flaws. Thank you **Rinkesh** for our deep philosophical conversations and for being there through my difficult phase. Many thanks to **Ravi** for our numerous wholehearted conversations and your consistent support during these years. **Varad**, you are a great listener and its always fun to discuss tech and politics with you. I would also like to thank **Tejas** for his genuine companionship and for keeping me informed about the industrial aspects of CFD. **Shivam**, I often introduce you as my *Sangharsh ka saathi*. You were there to understand and empathize with my PhD journey, and you have always encouraged me to focus on the silver-lining. Many thanks to **Soni ji** as well for bringing joy to all our conversations with his unique comments. Special thanks to **Ketan & Kalashree** for hosting me and imparting much needed wisdom on life and personal finance. I would also like to thank **Nilesh**, **Suraj**, **Sameep**, and **Chandra** for reaching out during this time. Additionally, I extend my gratitude to my seniors, **Ranjit sir** and **Sachin sir**, for being there to motivate me.

My journey to this milestone would not have been possible without the help of excellent teachers I had. While it's impossible to list them all, I must acknowledge a few who have had a significant impact on my path. Thank you **Dr. Virendra Bhojwani** and **Dr. Pradeep Patil**, for providing a solid foundation in the fundamental subjects during my graduate studies. Many thanks to **Dr. Vilas Kalamkar** for introducing me to the vast ocean of CFD through his engaging classroom lectures. I would also like to extend my special gratitude to **Dr. Trushar Gohil** for being such an excellent mentor. This PhD journey would not have initiated without your encouragement and pivotal guidance.

I extend appreciation to my family members for their constant encouragement throughout my Ph.D. journey. I'm grateful to my late grandfather for the wisdom and humility I learned from him. Thank you **Aaji** for cultivating good habits since childhood that have helped me become a better person. Thanks to **Bhau**, **Mothi Aai**, **Naana**, and **Naani** for their consistent support and blessings during these years. I would also like to appreciate **Sachin Dada** and **Reshma Tai** for always keeping me in their thoughts. Special thanks to **Simran**, **Samta** and **Mohit** for their affection and all the joyful conversations.

Finally, I would like to address the three "*constants*" of my life who defined my trajectory in this world of "*variables*". **Mummy-Pappa**, words won't do enough justice to describe the unconditional love and support that you have provided me throughout my life. You are the major source of all the positive values that help me grow as a person with each passing day. **Bhakti**, I'm truly fortunate to have a sister like you. You were always just a phone call away, patiently listening to my numerous problems and offering words of comfort. Thank you for being the wind beneath my wings. This journey would have been impossible without your constant emotional support and motivation.

Now, I would like to thank you (yes, you!) for (not) taking the time to go through this thesis :-). And in case you do, I hope you had relatively less trouble in reading the text than I had while writing it. Until we cross our paths again, take care, keep laughing, and ciao ciao!!

Shubham Dalvi
Enschede, August 2023

Bibliography

[1] M. Mokhlesi, *Traditional refrigerators, the forgotten masterpieces*, in *the Second Congress on Architecture and Urban Planning History*, volume 2, pages 685–98 [1985].

[2] D. Lynn, *Persia - exhibition catalog* [2005].

[3] S. Dalley, *Mari and karana: two old babylonian cities*, in *Mari and Karana: Two Old Babylonian Cities*, Gorgias Press [2002].

[4] M. Mahdavinejad & K. Javanrudi, *Assessment of ancient fridges: a sustainable method to storage ice in hot-arid climates*, Asian Culture and History, volume 4(2), page 133 [2012].

[5] *Cooling and refrigeration sector: the Cinderella of the EU's energy system* , https://www.euractiv.com/section/energy/opinion/cooling-and-refrigeration-sector-the-cinderella-of-the-eus-energy-system/ [2017].

[6] S. Anderson, E. Bandarra, C. Bhushan, N. Borgford-Parnell, Z. Chen, J. Christensen, S. Devotta, M. Lal Dhasan, G. Dreyfus, J. Dulac *et al.*, *Cooling emissions and policy synthesis report: Benefits of cooling efficiency and the kigali amendment* [2020].

[7] J. S. Brown & P. A. Domanski, *Review of alternative cooling technologies*, Applied Thermal Engineering, volume 64(1-2), pages 252–262 [2014].

[8] R. Lindsey & L. Dahlman, *Climate Change: Global Temperature* , https://www.climate.gov/news-features/understanding-climate/climate-change-global-temperature#:~:text=Earth's%20temperature%20has%20risen%20by,0.18%C2%B0%20C)%20per%20decade. [2022].

[9] V. K. Pecharsky & K. A. Gschneidner Jr, *Magnetocaloric effect and magnetic refrigeration*, Journal of Magnetism and Magnetic Materials, volume 200(1), pages 44–56 [1999].

[10] G. Brown, *Magnetic heat pumping near room temperature*, Journal of Applied Physics,

volume 47(8), pages 3673–3680 [1976].

[11] A. Smith, *Who discovered the magnetocaloric effect?*, The European Physical Journal H, volume 38(4), pages 507–517 [2013].

[12] P. Weiss & A. Piccard, *Le phénomène magnétocalorique*, J. Phys. Theor. Appl., volume 7(1), pages 103–109 [1917].

[13] K. Gschneidner Jr & V. Pecharsky, *Thirty years of near room temperature magnetic cooling: Where we are today and future prospects*, International journal of refrigeration, volume 31(6), pages 945–961 [2008].

[14] B. Yu, M. Liu, P. W. Egolf, & A. Kitanovski, *A review of magnetic refrigerator and heat pump prototypes built before the year 2010*, International Journal of refrigeration, volume 33(6), pages 1029–1060 [2010].

[15] A. Kitanovski, J. Tušek, U. Tomc, U. Plaznik, M. Ozbolt, & A. Poredoš, *Magnetocaloric energy conversion*, Springer [2016].

[16] A. M. Tishin & Y. I. Spichkin, *The magnetocaloric effect and its applications*, CRC Press [2016].

[17] S. Choi, U. Han, H. Cho, & H. Lee, *Recent advances in household refrigerator cycle technologies*, Applied Thermal Engineering, volume 132, pages 560–574 [2018].

[18] P. Bansal, E. Vineyard, & O. Abdelaziz, *Advances in household appliances-a review*, Applied Thermal Engineering, volume 31(17-18), pages 3748–3760 [2011].

[19] K. Rajamani, *A magnetocaloric mixture based refrigerator: From material to system level analysis*, PhD Thesis, University of Twente [2023].

[20] J. L. Neuringer & R. E. Rosensweig, *Ferrohydrodynamics*, The Physics of Fluids, volume 7(12), pages 1927–1937 [1964].

[21] R. Rosensweig, *Ferrohydrodynamics cambridge university press cambridge*, New York, Melbourne [1985].

[22] R. E. Rosensweig, *Magnetic fluids*, Annual review of fluid mechanics, volume 19(1), pages 437–461 [1987].

[23] R. E. Rosensweig, *Ferrohydrodynamics*, Courier Corporation [2013].

[24] I. Nkurikiyimfura, Y. Wang, & Z. Pan, *Heat transfer enhancement by magnetic nanofluids—a review*, Renewable and Sustainable Energy Reviews, volume 21, pages 548–561 [2013].

[25] M. Bahiraei & M. Hangi, *Flow and heat transfer characteristics of magnetic nanofluids: a review*, Journal of Magnetism and Magnetic Materials, volume 374, pages 125–138 [2015].

[26] M. Alsaady, R. Fu, B. Li, R. Boukhanouf, & Y. Yan, *Thermo-physical properties and thermo-magnetic convection of ferrofluid*, Applied Thermal Engineering, volume 88, pages 14–21 [2015].

[27] D. C. Giancoli, *Physics for scientists & engineers with modern physics*, Pearson [2014].

[28] J. D. Jackson, *Classical electrodynamics* [1999].

[29] D. J. Griffiths, *Introduction to electrodynamics*, American Association of Physics Teachers [2005].

[30] R. Ganguly, S. Sen, & I. K. Puri, *Thermomagnetic convection in a square enclosure using a line dipole*, Physics of Fluids, volume 16(7), pages 2228–2236 [2004].

[31] A. Mukhopadhyay, R. Ganguly, S. Sen, & I. K. Puri, *A scaling analysis to characterize thermomagnetic convection*, International Journal of Heat and Mass Transfer, volume 48(17), pages 3485–3492 [2005].

[32] R. Ganguly, S. Sen, & I. K. Puri, *Heat transfer augmentation using a magnetic fluid under the influence of a line dipole*, Journal of Magnetism and Magnetic Materials, volume 271(1), pages 63–73 [2004].

[33] T. Strek & H. Jopek, *Computer simulation of heat transfer through a ferrofluid*, Physica status solidi (b), volume 244(3), pages 1027–1037 [2007].

[34] M. Goharkhah & M. Ashjaee, *Effect of an alternating nonuniform magnetic field on ferrofluid flow and heat transfer in a channel*, Journal of Magnetism and Magnetic Materials, volume 362, pages 80–89 [2014].

[35] F. Selimefendigil & H. F. Öztop, *Effect of a rotating cylinder in forced convection of ferrofluid over a backward facing step*, International Journal of Heat and Mass Transfer, volume 71, pages 142–148 [2014].

[36] B. Ghorbani, S. Ebrahimi, & K. Vijayaraghavan, *CFD modeling and sensitivity analysis of heat transfer enhancement of a ferrofluid flow in the presence of a magnetic field*, International Journal of Heat and Mass Transfer, volume 127, pages 544–552 [2018].

[37] R. K. Shah & S. Khandekar, *Exploring ferrofluids for heat transfer augmentation*, Journal of Magnetism and Magnetic Materials, volume 475, pages 389–400 [2019].

[38] H. G. Weller, G. Tabor, H. Jasak, & C. Fureby, *A tensorial approach to computational continuum mechanics using object-oriented techniques*, Computers in physics, volume 12(6), pages 620–631 [1998].

[39] H. Andersson & O. Valnes, *Flow of a heated ferrofluid over a stretching sheet in the presence of a magnetic dipole*, Acta Mechanica, volume 128(1), pages 39–47 [1998].

[40] *Permanent Magnet Guidelines*, https://www.intemag.com/images/MMPAPMG-88.pdf [1996].

[41] J. Gould, *Permanent magnet applications*, IEEE Transactions on Magnetics, volume 5(4), pages 812–821 [1969].

[42] M. McCaig & A. G. Clegg, *Permanent magnets in theory and practice*, Pentech press,2nd Edition [1987].

[43] E. P. Furlani, *Permanent magnet and electromechanical devices: materials, analysis, and applications*, Academic press [2001].

[44] J. Coey, *Permanent magnet applications*, Journal of Magnetism and Magnetic Materials, volume 248(3), pages 441–456 [2002].

[45] V. T. Nguyen, *Magnetic field distribution of a conical permanent magnet with an application in magnetic resonance imaging*, Journal of Magnetism and Magnetic Materials, volume 498 [2020].

[46] S. Hart, K. Hart, & J. P. Selvaggi, *Analytical expressions for the magnetic field from axially magnetized and conically shaped permanent magnets*, IEEE Transactions on Magnetics, volume 56(7), pages 1–9 [2020].

[47] H. L. Rakotoarison, J.-P. Yonnet, & B. Delinchant, *Using coulombian approach for modeling scalar potential and magnetic field of a permanent magnet with radial polarization*, IEEE Transactions on Magnetics, volume 43(4), pages 1261–1264 [2007].

[48] R. Ravaud & G. Lemarquand, *Comparison of the coulombian and amperian current models for calculating the magnetic field produced by radially magnetized arc-shaped permanent magnets*, Progress In Electromagnetics Research, volume 95, page 309 [2009].

[49] J. S. Agashe & D. P. Arnold, *A study of scaling and geometry effects on the forces between cuboidal and cylindrical magnets using analytical force solutions*, Journal of Physics D: Applied Physics, volume 41(10), page 105001 [2008].

[50] N. Derby & S. Olbert, *Cylindrical magnets and ideal solenoids*, American Journal of Physics, volume 78(3), pages 229–235 [2010].

[51] R. Ravaud, G. Lemarquand, S. Babic, V. Lemarquand, & C. Akyel, *Cylindrical magnets and coils: Fields, forces, and inductances*, IEEE Transactions on Magnetics, volume 46(9), pages 3585–3590 [2010].

[52] C. M. Oldenburg, S. E. Borglin, & G. J. Moridis, *Numerical simulation of ferrofluid flow for subsurface environmental engineering applications*, Transport in Porous Media, volume 38(3), pages 319–344 [2000].

[53] G. Xiao-Fan, Y. Yong, & Z. Xiao-Jing, *Analytic expression of magnetic field distribution of rectangular permanent magnets*, Applied mathematics and mechanics, volume 25(3), pages 297–306 [2004].

[54] A. Arrott & T. Templeton, *Physical measurements in a permanent magnet field varying spatially*, Journal of applied physics, volume 99(8), page 08B507 [2006].

[55] K. Vervaeke, *6D magnetic field distribution measurements of permanent magnets with magnetic field camera scanner*, in *2015 5th International Electric Drives Production Conference (EDPC)*, pages 1–4, IEEE [2015].

[56] T.-C. Jue, *Analysis of combined thermal and magnetic convection ferrofluid flow in a cavity*, International communications in heat and mass transfer, volume 33(7), pages 846–852 [2006].

[57] D. Zablotsky, A. Mezulis, & E. Blums, *Surface cooling based on the thermomagnetic convection: Numerical simulation and experiment*, International Journal of Heat and Mass Transfer, volume 52(23-24), pages 5302–5308 [2009].

[58] M. Ashouri, B. Ebrahimi, M. Shafii, M. Saidi, & M. Saidi, *Correlation for nusselt number in pure magnetic convection ferrofluid flow in a square cavity by a numerical investigation*, Journal of Magnetism and Magnetic Materials, volume 322(22), pages 3607–3613 [2010].

[59] M. Ashouri & M. B. Shafii, *Numerical simulation of magnetic convection ferrofluid flow in a permanent magnet–inserted cavity*, Journal of Magnetism and Magnetic Materials, volume 442, pages 270–278 [2017].

[60] J. Joubert, M. Sharifpur, A. B. Solomon, & J. Meyer, *Enhancement in heat transfer of a ferrofluid in a differentially heated square cavity through the use of permanent magnets*, Journal of Magnetism and Magnetic Materials, volume 443, pages 149–158 [2017].

[61] V. Labinac, N. Erceg, & D. Kotnik-Karuza, *Magnetic field of a cylindrical coil*, American journal of physics, volume 74(7), pages 621–627 [2006].

[62] E. E. Callaghan & S. H. Maslen, *The magnetic field of a finite solenoid* [1960].

[63] S. Dalvi, T. H. van der Meer, & M. Shahi, *Numerical evaluation of the ferrofluid behaviour under the influence of three-dimensional non-uniform magnetic field*, International Journal of Heat and Fluid Flow, volume 94, page 108901 [2022].

[64] J. T. Conway, *Exact solutions for the magnetic fields of axisymmetric solenoids and current distributions*, IEEE transactions on magnetics, volume 37(4), pages 2977–2988 [2001].

[65] B. B. Dasgupta, *Magnetic field due to a solenoid*, AmJPh, volume 52(3), pages 258–258 [1984].

[66] S. R. Muniz, V. S. Bagnato, & M. Bhattacharya, *Analysis of off-axis solenoid fields using the magnetic scalar potential: An application to a zeeman-slower for cold atoms*, American Journal of Physics, volume 83(6), pages 513–517 [2015].

[67] P. Papadopoulos, P. Vafeas, & P. Hatzikonstantinou, *Ferrofluid pipe flow under the influence of the magnetic field of a cylindrical coil*, Physics of Fluids, volume 24(12), page 122002 [2012].

[68] *Projekt Elektronik, Axial probe 2000 mT (AS-NAP)*, https://www.projekt-elektronik.com/wp-content/uploads/sites/3/data-sheet-AS-active-probe-0203-5.2.pdf#page=16 [2021].

[69] Brandon, *Magnetic Materials: Types of Magnetism, Applications, and Origin of Magnetism*, https://msestudent.com/magnetic-materials-types-of-magnetism-applications-and-origin-of-magnetism/ [2022].

[70] M. Shliomis, *Magnetic fluids*, Soviet Physics Uspekhi, volume 17(2), page 153 [1974].

[71] M. I. Shliomis, *Ferrohydrodynamics: Testing a third magnetization equation*, Physical Review E, volume 64(6), page 060501 [2001].

[72] M. I. Shliomis, *Ferrohydrodynamics: Retrospective and issues*, in *Ferrofluids*, pages 85–111, Springer [2002].

[73] R. Kaiser & R. E. Rosensweig, *Study of ferromagnetic liquid*, volume 1407, National Aeronautics and Space Administration [1969].

[74] L. Mao, S. Elborai, X. He, M. Zahn, & H. Koser, *Direct observation of closed-loop ferrohydrodynamic pumping under traveling magnetic fields*, Physical review B, volume 84(10), page 104431 [2011].

[75] M. Martsenyuk, Y. L. Raikher, & M. Shliomis, *On the kinetics of magnetization of ferromagnetic particle suspensions*, Sov. Phys. JETP, volume 38, page 413 [1974].

[76] R. E. Rosensweig, *Heating magnetic fluid with alternating magnetic field*, Journal of magnetism and magnetic materials, volume 252, pages 370–374 [2002].

[77] J. Amaral, S. Das, & V. Amaral, *The mean-field theory in the study of ferromagnets and the magnetocaloric effect*, Thermodynamics: Systems in Equilibrium and Non-Equilibrium, volume 173 [2011].

[78] K. Ajith, A. S. Pillai, I. M. V. Enoch, & A. B. Solomon, *Effect of magnetic field on the thermophysical properties of low-density ferrofluid with disk-shaped mgfe2o4 nanoparticles*, Colloids and Surfaces A: Physicochemical and Engineering Aspects, volume 613, page 126083 [2021].

[79] M. Zhao & J. Hu, *Study on density of magnetic fluid in the strong magnetic field*, in *2012 Second International Conference on Instrumentation, Measurement, Computer, Communication and Control*, pages 396–398, IEEE [2012].

[80] R. Hao, H. Liu, & S. Wang, *Research on the density of magnetic fluid and its application in mineral separation*, in *Journal of Physics: Conference Series*, volume 1635, page 012061, IOP Publishing [2020].

[81] S. Doganay, R. Alsangur, & A. Turgut, *Effect of external magnetic field on thermal conductivity and viscosity of magnetic nanofluids: A review*, Materials Research Express, volume 6(11), page 112003 [2019].

[82] X. Fang, Y. Xuan, & Q. Li, *Anisotropic thermal conductivity of magnetic fluids*, Progress in natural science, volume 19(2), pages 205–211 [2009].

[83] C. L. Altan, A. Elkatmis, M. Yüksel, N. Aslan, & S. Bucak, *Enhancement of thermal conductivity upon application of magnetic field to Fe_3O_4 nanofluids*, Journal of Applied Physics, volume 110(9), page 093917 [2011].

[84] I. Nkurikiyimfura, Y. Wang, & Z. Pan, *Effect of chain-like magnetite nanoparticle aggregates on thermal conductivity of magnetic nanofluid in magnetic field*, Experimental Thermal and Fluid Science, volume 44, pages 607–612 [2013].

[85] H. Abbasov, *Modeling of anisotropic thermal conductivity of ferrofluids*, Journal of Dispersion Science and Technology, volume 41(7), pages 1030–1036 [2020].

[86] Q. Li, Y. Xuan, & J. Wang, *Experimental investigations on transport properties of magnetic fluids*, Experimental Thermal and Fluid Science, volume 30(2), pages 109–116 [2005].

[87] S. Ebrahimi & S. F. Saghravani, *Influence of magnetic field on the thermal conductivity of*

the water based mixed Fe_3O_4/cuo nanofluid, Journal of Magnetism and Magnetic Materials, volume 441, pages 366–373 [2017].

[88] W. Liu, J. Alsarraf, A. Shahsavar, M. Rostamzadeh, M. Afrand, & T. K. Nguyen, *Impact of oscillating magnetic field on the thermal-conductivity of water-Fe_3O_4 and water-Fe_3O_4/cnt ferro-fluids: Experimental study*, Journal of Magnetism and Magnetic Materials, volume 484, pages 258–265 [2019].

[89] W. Kordonsky, S. Gorodkin, & S. Demchuk, *Magnetorheological control of heat transfer*, International journal of heat and mass transfer, volume 36(11), pages 2783–2788 [1993].

[90] G. Yildirim & S. Genc, *Experimental study on heat transfer of the magnetorheological fluids*, Smart materials and structures, volume 22(8), page 085001 [2013].

[91] J. Maroofi, S. Hashemabadi, & Y. Rabbani, *Investigation of the chain formation effect on thermal conductivity of magnetorheological fluids*, Journal of Thermophysics and Heat Transfer, volume 34(1), pages 3–12 [2020].

[92] Z. Shulman, V. Kordonsky, & S. Demchuk, *The mechanism of heat transfer in magnetorheological systems*, International Journal of Heat and Mass Transfer, volume 22(3), pages 389–394 [1979].

[93] J. Maroofi & S. Hashemabadi, *Experimental and numerical investigation of parameters influencing anisotropic thermal conductivity of magnetorheological fluids*, Heat and Mass Transfer, volume 55(10), pages 2751–2767 [2019].

[94] B. N. Reinecke, J. W. Shan, K. K. Suabedissen, & A. S. Cherkasova, *On the anisotropic thermal conductivity of magnetorheological suspensions*, Journal of applied physics, volume 104(2), page 023507 [2008].

[95] I. Forero-Sandoval, A. Vega-Flick, J. Alvarado-Gil, & R. Medina-Esquivel, *Study of thermal conductivity of magnetorheological fluids using the thermal-wave resonant cavity and its relationship with the viscosity*, Smart Materials and Structures, volume 26(2), page 025010 [2016].

[96] J. C. Maxwell, *A treatise on electricity and magnetism*, volume 1, Clarendon press [1873].

[97] D. J. Jeffrey, *Conduction through a random suspension of spheres*, Proceedings of the Royal Society of London. A. Mathematical and Physical Sciences, volume 335(1602), pages 355–367 [1973].

[98] L. Rayleigh, *Lvi. on the influence of obstacles arranged in rectangular order upon the*

properties of a medium, The London, Edinburgh, and Dublin Philosophical Magazine and Journal of Science, volume 34(211), pages 481–502 [1892].

[99] Y.-P. Chiu, Y. Chen, S.-Y. Yang, J. Chen, H.-E. Horng, H.-C. Yang, W. Tse, & C.-Y. Hong, *Specific heat of magnetic fluids under a modulated magnetic field*, Journal of applied physics, volume 93(4), pages 2079–2081 [2003].

[100] V. Korolev, I. Aref'ev, & A. Ramazanova, *Magnetocaloric effect and the heat capacity of ferrimagnetic nanosystems in magnetic fluids*, Russian Journal of Physical Chemistry A, volume 81(10), pages 1677–1680 [2007].

[101] I. Mugica, S. Poncet, & J. Bouchard, *3D direct numerical simulation of magneto-caloric regenerators* [2018].

[102] A. Einstein *et al.*, *On the motion of small particles suspended in liquids at rest required by the molecular-kinetic theory of heat*, Annalen der physik, volume 17(549-560), page 208 [1905].

[103] H. D. Koca, S. Doganay, A. Turgut, I. H. Tavman, R. Saidur, & I. M. Mahbubul, *Effect of particle size on the viscosity of nanofluids: A review*, Renewable and Sustainable Energy Reviews, volume 82, pages 1664–1674 [2018].

[104] S. Odenbach & K. Raj, *The influence of large particles and agglomerates on the magneto-viscous effect in ferrofluids*, Magnetohydrodynamics, volume 36(4), pages 312–319 [2000].

[105] K. Shah, R. Upadhyay, & V. Aswal, *Influence of large size magnetic particles on the magneto-viscous properties of ferrofluid*, Smart materials and structures, volume 21(7), page 075005 [2012].

[106] J. Nowak, F. Wiekhorst, L. Trahms, & S. Odenbach, *The influence of hydrodynamic diameter and core composition on the magnetoviscous effect of biocompatible ferrofluids*, Journal of Physics: Condensed Matter, volume 26(17), page 176004 [2014].

[107] S. Odenbach, *Chapter 3 ferrofluids*, Handbook of magnetic materials, volume 16, pages 127–208 [2006].

[108] E. Lemaire, A. Meunier, G. Bossis, J. Liu, D. Felt, P. Bashtovoi, & N. Matoussevitch, *Influence of the particle size on the rheology of magnetorheological fluids*, Journal of Rheology, volume 39(5), pages 1011–1020 [1995].

[109] B. De Gans, N. Duin, D. Van den Ende, & J. Mellema, *The influence of particle size on the magnetorheological properties of an inverse ferrofluid*, The Journal of Chemical Physics,

volume 113(5), pages 2032–2042 [2000].

[110] M. I. Shliomis & K. I. Morozov, *Negative viscosity of ferrofluid under alternating magnetic field*, Physics of Fluids, volume 6(8), pages 2855–2861 [1994].

[111] J.-C. Bacri, R. Perzynski, M. Shliomis, & G. Burde, *"negative-viscosity" effect in a magnetic fluid*, Physical review letters, volume 75(11), page 2128 [1995].

[112] C. Singh, A. K. Das, & P. K. Das, *Flow restrictive and shear reducing effect of magnetization relaxation in ferrofluid cavity flow*, Physics of Fluids, volume 28(8), page 087103 [2016].

[113] J. P. McTague, *Magnetoviscosity of magnetic colloids*, The Journal of Chemical Physics, volume 51(1), pages 133–136 [1969].

[114] R. Rosensweig, R. Kaiser, & G. Miskolczy, *Viscosity of magnetic fluid in a magnetic field*, Journal of Colloid and Interface Science, volume 29(4), pages 680–686 [1969].

[115] W. Hall & S. Busenberg, *Viscosity of magnetic suspensions*, The Journal of Chemical Physics, volume 51(1), pages 137–144 [1969].

[116] M. Shliomis *et al.*, *Effective viscosity of magnetic suspensions*, Zh. Eksp. Teor. Fiz, volume 61(2411), pages s1971d–1971 [1971].

[117] A. Afifah, S. Syahrullail, & N. Sidik, *Magnetoviscous effect and thermomagnetic convection of magnetic fluid: A review*, Renewable and Sustainable Energy Reviews, volume 55, pages 1030–1040 [2016].

[118] R. Moskowitz & R. Rosensweig, *Nonmechanical torque-driven flow of a ferromagnetic fluid by an electromagnetic field*, Applied Physics Letters, volume 11(10), pages 301–303 [1967].

[119] A. Y. Zubarev, S. Odenbach, & J. Fleischer, *Rheological properties of dense ferrofluids. effect of chain-like aggregates*, Journal of magnetism and magnetic materials, volume 252, pages 241–243 [2002].

[120] A. Zeuner, R. Richter, & I. Rehberg, *Experiments on negative and positive magnetoviscosity in an alternating magnetic field*, Physical Review E, volume 58(5), page 6287 [1998].

[121] K. R. Schumacher, I. Sellien, G. S. Knoke, T. Cader, & B. A. Finlayson, *Experiment and simulation of laminar and turbulent ferrofluid pipe flow in an oscillating magnetic field*, Physical Review E, volume 67(2), page 026308 [2003].

[122] M. I. Shliomis & M. A. Zaks, *Ferrofluidic torsional pendulum driven by oscillating magnetic field*, Physical Review E, volume 73(6), page 066208 [2006].

[123] M. Tekir, E. Taskesen, B. Aksu, E. Gedik, & K. Arslan, *Comparison of bi-directional multi-wave alternating magnetic field effect on ferromagnetic nanofluid flow in a circular pipe under laminar flow conditions*, Applied Thermal Engineering, volume 179, page 115624 [2020].

[124] B. Felderhof, *Flow of a ferrofluid down a tube in an oscillating magnetic field*, Physical Review E, volume 64(2), page 021508 [2001].

[125] A. P. Krekhov, M. I. Shliomis, & S. Kamiyama, *Ferrofluid pipe flow in an oscillating magnetic field*, Physics of Fluids, volume 17(3), page 033105 [2005].

[126] J. H. Sánchez & C. Rinaldi, *Magnetoviscosity of dilute magnetic fluids in oscillating and rotating magnetic fields*, Physics of Fluids, volume 22(4), page 307 [2010].

[127] B. A. Finlayson, *Spin-up of ferrofluids: The impact of the spin viscosity and the langevin function*, Physics of Fluids, volume 25(7), page 073101 [2013].

[128] C. Jimenez, H. Vargas, & R. Correa, *Velocity profiles of ferrofluids in a cylindrical container and in the presence of external rotating magnetic fields of high strength and frequency.*, Magnetohydrodynamics (0024-998X), volume 56(4) [2020].

[129] Y. Lu, H. Zhou, H. Mao, S. Tang, L. Sheng, H. Zhang, & J. Liu, *Liquid metal-based magnetorheological fluid with a large magnetocaloric effect*, ACS Applied Materials & Interfaces, volume 12(43), pages 48748–48755 [2020].

[130] D. G. Thomas, *Transport characteristics of suspension: Viii. a note on the viscosity of newtonian suspensions of uniform spherical particles*, Journal of colloid science, volume 20(3), pages 267–277 [1965].

[131] R. Durand, *Basic relationships of the trnsportation of solids in pipes-experimental research*, Intern. Assoc. Hydr. Res., 5th Congr. Minneapolis, 1953 [1953].

[132] R. Turian, F.-L. Hsu, & T.-W. Ma, *Estimation of the critical velocity in pipeline flow of slurries*, Powder Technology, volume 51(1), pages 35–47 [1987].

[133] R. C. Ramsdell & S. A. Miedema, *An overview of flow regimes describing slurry transport*, WODCON XX, page 15 [2013].

[134] P. Doron, D. Granica, & D. Barnea, *Slurry flow in horizontal pipes—experimental and modeling*, International journal of multiphase flow, volume 13(4), pages 535–547 [1987].

[135] P. Doron & D. Barnea, *A three-layer model for solid-liquid flow in horizontal pipes*, International Journal of Multiphase Flow, volume 19(6), pages 1029–1043 [1993].

[136] P. Doron & D. Barnea, *Flow pattern maps for solid-liquid flow in pipes*, International journal of multiphase flow, volume 22(2), pages 273–283 [1996].

[137] A. P. Poloski, M. L. Bonebrake, A. M. Casella, M. D. Johnson, J. J. Toth, H. E. Adkins, J. Chun, K. M. Denslow, M. Luna, & J. M. Tingey, *Deposition velocities of non-newtonian slurries in pipelines: complex simulant testing*, Technical report, Pacific Northwest National Lab.(PNNL), Richland, WA (United States) [2009].

[138] B. Bbosa, E. DelleCase, M. Volk, & E. Ozbayoglu, *A comprehensive deposition velocity model for slurry transport in horizontal pipelines*, Journal of Petroleum Exploration and Production Technology, volume 7(1), pages 303–310 [2017].

[139] R. Gillies, R. Sun, R. Sanders, & J. & Schaan, *Lowered expectations: the impact of yield stress on sand transport in laminar, non-newtonian slurry flows*, Journal of the Southern African Institute of Mining and Metallurgy, volume 107(6), pages 351–357 [2007].

[140] J. R. Grace, *Contacting modes and behaviour classification of gas—solid and other two-phase suspensions*, The Canadian Journal of Chemical Engineering, volume 64(3), pages 353–363 [1986].

[141] M. Ishii & T. Hibiki, *Thermo-fluid dynamics of two-phase flow*, Springer Science & Business Media [2010].

[142] B. Peters, M. Baniasadi, M. Baniasadi, X. Besseron, A. E. Donoso, M. Mohseni, & G. Pozzetti, *Xdem multi-physics and multi-scale simulation technology: Review of dem–cfd coupling, methodology and engineering applications*, Particuology, volume 44, pages 176–193 [2019].

[143] C. E. Brennen, *Fundamentals of multiphase flow*, Cambridge university press [2005].

[144] C. Crowe, M. Sommerfeld, Y. Tsuji *et al.*, *Multiphase Flows with Droplets and Particles*, Ž [1998].

[145] M. Manninen, V. Taivassalo, & S. Kallio, *On the mixture model for multiphase flow* [1996].

[146] C. Van Rhee, *On the sedimentation process in a trailing suction hopper dredger* [2002].

[147] H. Zambrano, L. D. G. Sigalotti, J. Klapp, F. Peña-Polo, & A. Bencomo, *Heavy oil slurry transportation through horizontal pipelines: Experiments and CFD simulations*,

International Journal of Multiphase Flow, volume 91, pages 130–141 [2017].

[148] J. Wang, T. Zhang, & S. Wang, *Heterogeneous ice slurry flow and concentration distribution in horizontal pipes*, International Journal of Heat and Fluid Flow, volume 44, pages 425–434 [2013].

[149] B. B. Nayak, S. K. Gupta, D. Chatterjee, & A. N. Mullick, *Numerical analysis of convective transport of fly ash-water slurry through a horizontal pipe*, The Journal of Computational Multiphase Flows, volume 7(2), pages 79–96 [2015].

[150] B. Bhusan Nayak & D. Chatterjee, *Assessment of mixture and eulerian multiphase models in predicting the thermo-fluidic transport characteristics for fly ash-water slurry flow in straight horizontal pipeline*, Heat Transfer Engineering, volume 40(8), pages 679–692 [2019].

[151] A. Boghi, L. Brown, R. Sawko, & C. P. Thompson, *An inertial two-phase model of wax transport in a pipeline during pigging operations*, International Journal of Multiphase Flow, volume 94, pages 17–30 [2017].

[152] R. Rosensweig, S. JH, L. WK *et al.*, *Magnetically stabilized fluidized solids* [1981].

[153] Y. A. Sergeev & M. Muromsky, *On propagation of concentration disturbances in a magnetically stabilized fluidized bed*, International journal of multiphase flow, volume 20(5), pages 927–938 [1994].

[154] R. Rozenblit, M. Simkhis, G. Hetsroni, D. Barnea, & Y. Taitel, *Heat transfer in horizontal solid–liquid pipe flow*, International journal of multiphase flow, volume 26(8), pages 1235–1246 [2000].

[155] P. Kuzhir, G. Bossis, V. Bashtovoi, & L. Vekas, *Capillary flow of a suspension of non-magnetic particles in a ferrofluid under highly non-uniform magnetic field*, International journal of multiphase flow, volume 31(2), pages 201–221 [2005].

[156] Z. Recebli & H. Kurt, *Two-phase steady flow along a horizontal glass pipe in the presence of the magnetic and electrical fields*, International journal of heat and fluid flow, volume 29(1), pages 263–268 [2008].

[157] H. Aminfar, M. Mohammadpourfard, & F. Mohseni, *Two-phase mixture model simulation of the hydro-thermal behavior of an electrical conductive ferrofluid in the presence of magnetic fields*, Journal of Magnetism and Magnetic Materials, volume 324(5), pages 830–842 [2012].

[158] H. Aminfar, M. Mohammadpourfard, & F. Ghaderi, *Two-phase simulation of non-uniform magnetic field effects on biofluid (blood) with magnetic nanoparticles through a*

collapsible tube, Journal of magnetism and magnetic materials, volume 332, pages 172–179 [2013].

[159] C. Kittel, P. McEuen, & P. McEuen, *Introduction to solid state physics*, volume 8, Wiley New York [1996].

[160] R. Hamilton & O. Crosser, *Thermal conductivity of heterogeneous two-component systems*, Industrial & Engineering chemistry fundamentals, volume 1(3), pages 187–191 [1962].

[161] G. Batchelor, *The effect of brownian motion on the bulk stress in a suspension of spherical particles*, Journal of fluid mechanics, volume 83(1), pages 97–117 [1977].

[162] T. Tynjälä, A. Bozhko, P. Bulychev, G. Putin, & P. Sarkomaa, *On features of ferrofluid convection caused by barometrical sedimentation*, Journal of Magnetism and Magnetic Materials, volume 300(1), pages e195–e198 [2006].

[163] A. Jafari, T. Tynjälä, S. Mousavi, & P. Sarkomaa, *Simulation of heat transfer in a ferrofluid using computational fluid dynamics technique*, International Journal of Heat and Fluid Flow, volume 29(4), pages 1197–1202 [2008].

[164] H. Aminfar, M. Mohammadpourfard, & Y. N. Kahnamouei, *A 3d numerical simulation of mixed convection of a magnetic nanofluid in the presence of non-uniform magnetic field in a vertical tube using two phase mixture model*, Journal of Magnetism and Magnetic Materials, volume 323(15), pages 1963–1972 [2011].

[165] H. Aminfar, M. Mohammadpourfard, & S. A. Zonouzi, *Numerical study of the ferrofluid flow and heat transfer through a rectangular duct in the presence of a non-uniform transverse magnetic field*, Journal of Magnetism and Magnetic materials, volume 327, pages 31–42 [2013].

[166] M. Ghasemian, Z. N. Ashrafi, M. Goharkhah, & M. Ashjaee, *Heat transfer characteristics of Fe_3O_4 ferrofluid flowing in a mini channel under constant and alternating magnetic fields*, Journal of Magnetism and Magnetic Materials, volume 381, pages 158–167 [2015].

[167] M. Hangi, M. Bahiraei, & A. Rahbari, *Forced convection of a temperature-sensitive ferrofluid in presence of magnetic field of electrical current-carrying wire: A two-phase approach*, Advanced Powder Technology, volume 29(9), pages 2168–2175 [2018].

[168] M. H. Hekmat & K. K. Ziarati, *Effects of nanoparticles volume fraction and magnetic field gradient on the mixed convection of a ferrofluid in the annulus between vertical concentric cylinders*, Applied Thermal Engineering, volume 152, pages 844–857 [2019].

[169] E. Yousefi, H. R. Nazif, H. Najafi Khaboshan, & A. Azarinia, *Non-uniform magnetic field effect on forced convection heat transfer of flattened tubes using two-phase mixture model*, Heat Transfer Engineering, volume 42(12), pages 1041–1058 [2021].

[170] G. Tronci, A. Buffo, M. Vanni, & D. Marchisio, *Validation of the diffusion mixture model for the simulation of bubbly flows and implementation in openfoam*, Computers & Fluids, page 105026 [2021].

[171] K. Hiltunen, A. Jäsberg, S. Kallio, H. Karema, M. Kataja, A. Koponen, M. Manninen, & V. Taivassalo, *Multiphase flow dynamics*, Theory and Numerics. Tech. Rep, volume 722 [2009].

[172] D. Gidaspow, *Multiphase flow and fluidization: continuum and kinetic theory descriptions*, Academic press [1994].

[173] A. Bozhko & T. Tynjälä, *Influence of gravitational sedimentation of magnetic particles on ferrofluid convection in experiments and numerical simulations*, Journal of magnetism and magnetic materials, volume 289, pages 281–284 [2005].

[174] R. B. Bird, *Transport phenomena*, Appl. Mech. Rev., volume 55(1), pages R1–R4 [2002].

[175] S. Dalvi, T. H. van der Meer, & M. Shahi, *Hydro-thermal interactions of a ferrofluid in a non-uniform magnetic field*, Heat and Mass Transfer, pages 1–11 [2022].

[176] S. Dalvi, E. Karaliolios, T. H. van der Meer, & M. Shahi, *Thermo-magnetic convection in a circular annulus filled with magnetocaloric nanofluid*, International Communications in Heat and Mass Transfer, volume 116, page 104654 [2020].

[177] K. Fumoto, H. Yamagishi, & M. Ikegawa, *A mini heat transport device based on thermo-sensitive magnetic fluid*, Nanoscale and Microscale Thermophysical Engineering, volume 11(1-2), pages 201–210 [2007].

[178] W. Lian, Y. Xuan, & Q. Li, *Design method of automatic energy transport devices based on the thermomagnetic effect of magnetic fluids*, International Journal of Heat and Mass Transfer, volume 52(23-24), pages 5451–5458 [2009].

[179] Y. Xuan & W. Lian, *Electronic cooling using an automatic energy transport device based on thermomagnetic effect*, Applied Thermal Engineering, volume 31(8-9), pages 1487–1494 [2011].

[180] W. Lian, Y. Xuan, & Q. Li, *Characterization of miniature automatic energy transport devices based on the thermomagnetic effect*, Energy Conversion and Management, volume 50(1),

pages 35–42 [2009].

[181] Y. Iwamoto, H. Yamaguchi, & X.-D. Niu, *Magnetically-driven heat transport device using a binary temperature-sensitive magnetic fluid*, Journal of Magnetism and Magnetic Materials, volume 323(10), pages 1378–1383 [2011].

[182] H. Yamaguchi & Y. Iwamoto, *Energy transport in cooling device by magnetic fluid*, Journal of Magnetism and Magnetic Materials, volume 431, pages 229–236 [2017].

[183] M. Bahiraei & M. Hangi, *Automatic cooling by means of thermomagnetic phenomenon of magnetic nanofluid in a toroidal loop*, Applied Thermal Engineering, volume 107, pages 700–708 [2016].

[184] T. H. Kuehn & R. J. Goldstein, *Numerical solution to the navier-stokes equations for laminar natural convection about a horizontal isothermal circular cylinder*, International Journal of Heat and Mass Transfer, volume 23(7), pages 971–979 [1980].

[185] E. Abu-Nada, Z. Masoud, & A. Hijazi, *Natural convection heat transfer enhancement in horizontal concentric annuli using nanofluids*, International Communications in Heat and Mass Transfer, volume 35(5), pages 657–665 [2008].

[186] J. R. Gómez, R. F. Garcia, A. D. M. Catoira, & M. R. Gómez, *Magnetocaloric effect: A review of the thermodynamic cycles in magnetic refrigeration*, Renewable and Sustainable Energy Reviews, volume 17, pages 74–82 [2013].

[187] C. Graham Jr, *Magnetic behavior of gadolinium near the curie point*, Journal of Applied Physics, volume 36(3), pages 1135–1136 [1965].

[188] M. Suziuki, *Lecture note on solid state physics: Mean field theory, department of physics state university of new york, binghamton, 2006*.

[189] C. Kittel, *Introduction to solid state physics*, Wiley [2005].

[190] M. Laouyenne, S. Mahjoub, M. Baazaoui, E. Hlil, & M. Oumezzine, *Magnetic entropy change by mean-field theory for the second-order phase transition manganite nd0. 6sr0. 3ca0. 1mn0. 975fe0. 025o3*, Journal of Superconductivity and Novel Magnetism, volume 29(5), pages 1151–1157 [2016].

[191] M. Darby, *Tables of the brillouin function and of the related function for the spontaneous magnetization*, British Journal of Applied Physics, volume 18(10), page 1415 [1967].

[192] P. S. Szabo, M. Beković, & W.-G. Früh, *Using infrared thermography to investigate thermomagnetic convection under spatial non-uniform magnetic field*, International Journal

of Thermal Sciences, volume 116, pages 118–128 [2017].

[193] *Comsol Multiphysics ®, User's Guide, Version 5.4.*

[194] R. Groot, *Magnetocaloric Refrigeration: Design of major components for a refrigeration system utilizing a circulating magnetocaloric mixture*, Master's Thesis, University of Twente [2022].

[195] R. K. Shah & A. L. London, *Laminar flow forced convection in ducts: a source book for compact heat exchanger analytical data*, Academic press [2014].

[196] C. J. Greenshields, *Openfoam user guide*, OpenFOAM Foundation Ltd, version, volume 3(1), page 47 [2015].

[197] J. H. Ferziger, M. Perić, & R. L. Street, *Computational methods for fluid dynamics*, volume 3, Springer [2002].

[198] F. Moukalled, L. Mangani, M. Darwish *et al.*, *The finite volume method in computational fluid dynamics*, volume 6, Springer [2016].

[199] *ManetoCaloric Materials CALORIVAC* , https://vacuumschmelze.com/03_Documents/Brochures/CALORIVAC-PCV-001.pdf [2015].

[200] M. Games, *HALBACH ARRAY How to double the power of magnets, science experiment*, https://www.youtube.com/watch?v=uQWHjj6ofwo [2016].

[201] F. P. Incropera, D. P. DeWitt, T. L. Bergman, A. S. Lavine *et al.*, *Fundamentals of heat and mass transfer*, volume 6, Wiley New York [1996].

[202] D. Cebron, *Magnetic fields of solenoids and magnets*, https://www.mathworks.com/matlabcentral/fileexchange/71881-magnetic-fields-of-solenoids-and-magnets [2020].

[203] C. T. Crowe, J. D. Schwarzkopf, M. Sommerfeld, & Y. Tsuji, *Multiphase flows with droplets and particles*, CRC press [2011].